DEVELOPMENT OF THE HIGH VELOCITY TRANSIENT FIELD TECHNIQUE AND MEASUREMENT OF THE 2_1^+ g FACTORS OF ^{38,40}S

By

Andrew David Davies

A DISSERTATION

Submitted to
Michigan State University
in partial fulfillment of the requirements
for the degree of

DOCTOR OF PHILOSOPHY

Department of Physics and Astronomy

2006

ABSTRACT

DEVELOPMENT OF THE HIGH VELOCITY TRANSIENT FIELD TECHNIQUE AND MEASUREMENT OF THE 2_1^+ g FACTORS OF ^{38,40}S

By

Andrew David Davies

The onset of deformation in the neutron-rich sulfur isotopes has been investigated, through a new application of the transient field technique for measuring short-lived excited-state g factors with fast radioactive beams. The g factor (the magnetic dipole moment divided by the spin of the nuclear state) can provide insight into the complex interplay between single particle configurations and collective behavior in a nuclear state. In the case of the neutron-rich sulfur isotopes, a transition from spherical to deformed shapes has been inferred from first-excited state energy and transition probability measurements. However, the underlying causes of the deformation change have not yet been deduced. Knowledge of the $g(2^+)$ values can greatly constrain nuclear models and provide insight into the causes of the deformation change. However, the measurement of both the sign and magnitude of picosecond excited-state g factors requires the use of the transient field method, which generally requires ion velocities of Zv_0 ($v_0 = c/137$), or lower. Due to the high velocity of fragmentation products, the conventional transient field technique (which has been extensively developed for stable, Coulomb-barrier energy beams) could not be applied, and challenges posed by high-velocity radioactive beams needed to be overcome. A new technique, which combines the transient field method with intermediate-energy Coulomb excitation, has been developed in order to provide access to $g(2^+)$ values in fast radioactive secondary beams. The $g(2^+)$ values of ^{38}S and ^{40}S, with $N = 22$ and 24, were measured in the first application of the method at the NSCL. The description of the technique, results, and interpretation within a shell-model context is presented in this dissertation.

for Debbie

ACKNOWLEDGMENTS

This dissertation would certainly not have been possible without the help and support of a lot of people. I gratefully acknowledge Michigan State University, the Department of Physics and Astronomy, the NSCL, the National Science Foundation, and the APS Division of Nuclear Physics for financial support for graduate school and to travel to conferences. My adviser Paul Mantica always ensured I had the resources necessary to get this project done, and it was a privilege learning how to be an experimentalist from him. It was the vision and physical insight of Andrew Stuchbery that inspired the entire experiment, and his participation in every facet of the project despite being located thousands of miles away is greatly appreciated. Warren Rogers ultimately was responsible for my decision to go to graduate school; he is a true mentor, and has also had a huge impact through the Conference Experience for Undergraduates. Warren first introduced me to both Paul and Andrew S. — it's a small world!

I thank the members of my thesis committee, Gregers Hansen, Alex Brown, Thomas Glasmacher, Bhanu Mahanti, Paul Mantica, Andrew Stuchbery, and Michael Thoennessen, for their guidance and helpful discussions over the years.

The NSCL technical staff are totally outstanding, and literally dozens of people helped make the project a reality. I really need to thank Len Morris and Renan Fontus for their design work, and the NSCL Machine Shop for producing nearly everything we needed. John Priller wrote the magnet control script and John Brandon built the interface module that was inspired by Kelly Davidson. I thank John Yurkon for the PMT and for detector design advice, and Al Zeller for running the magnet calculations. Ron Fox helped enormously with the data acquisition, and Wil Mueller put in a lot of effort to support the use of SeGA. I needed to call on many others in order to build and set everything up prior to the run, and I am truly indebted to them all.

Theo Mertzimekis deserves a huge amount of credit for being truly helpful over the years, especially during the target test run, and together with Sean and Bryan, made the ANU measurements possible. Paul Davidson and Anna Wilson went above and beyond to contribute to the success of the experiment, and I can't thank them enough. Many thanks go to the Gamma Group, especially to Heather for her help with the SeGA stand, and to so many others for help during the setup and with taking shifts. The other graduate students here at MSU have been great friends and it has been a pleasure to spend all these years here in large part because of them. I especially should thank Chip, Nate, Heather, Russ, Joe, Josh, Ryan, and Pete for their friendship and for being great study partners for those first years here. Elaine, Chandana, and Jeremy have been great friends. I have been lucky to have been part of a research group here that has great chemistry among its members and has made this time worthwhile.

I want to thank my family for their love and support throughout college and graduate school. I thank God for them, for making it possible for me to attend Westmont in the first place, and for bringing Debbie into my life. Debbie, you have shown me so much love and patience while going through graduate school at the same time, and I love you.

Contents

List of Figures

List of Tables

Chapter 1

Introduction

Many systems in nature that consist of charged particles possess electromagnetic moments, including atomic nuclei. The electromagnetic moments of a nucleus are among its most fundamental properties, and since the electromagnetic interaction is well understood, nuclear theories can readily provide predictions of electromagnetic moments, which are experimental observables. Measurements of certain electromagnetic moments stringently test nuclear models because moments are very sensitive to the details of the nuclear wavefunction. In part, this is because the static electromagnetic moments are expectation values of "one-body" operators acting on single nuclear states. Since electromagnetic moments probe the properties of nuclear states, they are particularly useful in transitional regions of the nuclear chart, where they can be used to quantify the changes occurring and uncover their underlying causes.

The heavy sulfur isotopes have transitional characteristics, changing from spherical to deformed as neutrons are added beyond the stable, naturally occurring sulfur isotopes. The experimental evidence for the changing structure will be summarized in the following sections, where it will be pointed out that although several observables have been measured in this region of the nuclear chart, an understanding of the underlying causes of the shape transition is lacking. The onset of deformation in the sulfur isotopes is interesting because it coincides with the crossing of neutron

number $N = 20$, and continues toward $N = 28$, which are two "magic" numbers of neutrons in the stable nuclei, associated with extra binding energy indicative of a large energy gap in the nuclear shell structure. With increasing neutron excess, different orbits begin to be occupied compared to the situation at stability, and changes in the relative spacing of those single-particle orbits occur [1]. Since exotic nuclei are difficult to produce, experimentally measured properties are often sparse, providing no constraint for theoretical predictions, which can vary widely. It is the goal of this dissertation to describe new measurements on the neutron-rich sulfur isotopes that give a defining perspective on the evolution of their shell structure. After giving some details of the physics of the neutron-rich sulfur isotopes, an introduction to the nuclear excited-state magnetic dipole moment will be given, along with the justification of how the magnetic moment enables the elucidation of the underlying contributions to the structure of the neutron-rich sulfur isotopes.

1.1 Physics of Neutron-rich Sulfur Isotopes

The isotopes studied in the present work, ^{38}S and ^{40}S, are located in the chart of the nuclides in between the $N = 20$ and $N = 28$ closed neutron shells, where neutrons occupy the $f_{7/2}$ shell-model orbital. A view of the surrounding nuclides can be seen in Fig. 1.1, with the stable isotopes shown in black. Sulfur isotopes have 16 protons, and the last two protons fill the $2s_{1/2}$ orbit, forming a $Z = 16$ subshell closure which is partially evidenced by the fact that sulfur has the largest number of stable isotopes for any element lighter than calcium. A schematic of the relevant shell model orbitals is shown in Fig. 1.2. The heaviest stable isotope of sulfur is $^{36}_{16}S_{20}$, which has (in addition to the subshell closure at $Z = 16$) a full neutron $d_{3/2}$ orbital which closes the $N = 20$ major shell. That situation makes ^{36}S a stable, almost doubly-magic nucleus, with a high-energy first-excited state observed at 3.29 MeV. Adding one neutron pair to ^{36}S makes ^{38}S, a radioactive nuclide with $T_{1/2} = 170.3$ m and a

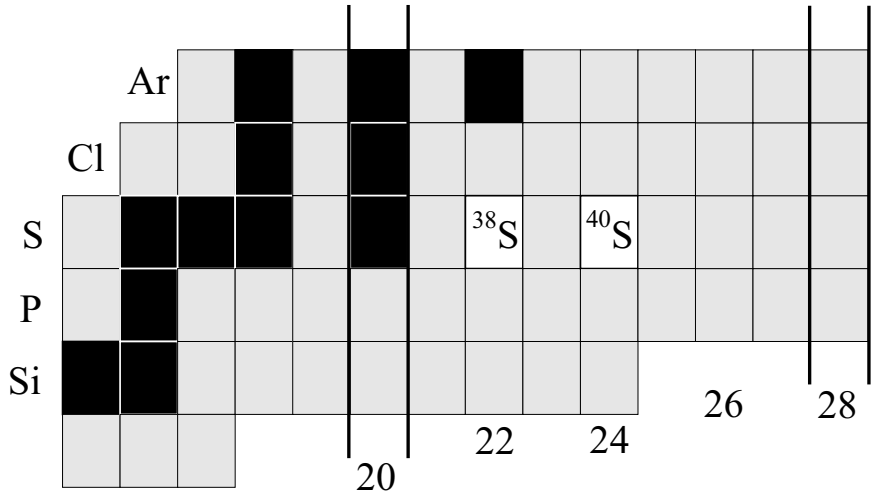

Figure 1.1: Region of the nuclear chart near ^{38,40}S, with the stable isotopes in black. The $N = 20, 28$ closed neutron shells are shown outlined in black. Sulfur isotopes have 16 protons.

2.9 MeV β-decay Q value. Adding one more pair of neutrons makes ^{40}S, the mid-shell nucleus for the $N = 20 - 28$ shell, with $T_{1/2} = 8.8$ s and a 4.7 MeV β-decay Q value. Initial interest in the neutron-rich sulfur isotopes arose when anomalous ^{46}Ca/^{48}Ca abundance ratios were observed in meteoritic inclusions [2], and it was suggested that the neutron-rich sulfur isotopes play an important role in the nucleosynthesis of heavy Ca-Ti-Cr isotopes (see Ref. [3] and references therein). Soon thereafter, indications of transitional properties arose as measurements began to be made on the neutron-rich sulfur isotopes, and it was recognized that these isotopes also offer a probe of changing shell structure as the neutron number approaches 28, away from the stability line. A survey of the experimental study of these isotopes prior to the current work will be given in the following section.

1.1.1 Previous Experimental and Theoretical Work

The isotope ^{38}S is accessible with two-neutron transfer onto ^{36}S, which is most readily done using (t, p) reactions. Since the isotopic abundance of ^{36}S is only 0.02% of natural sulfur, the (t, p) measurements were difficult to perform but resulted in the

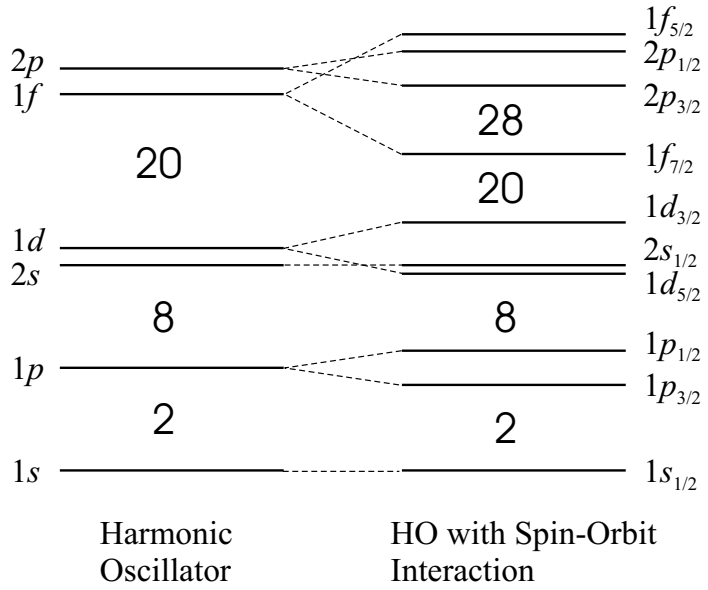

Figure 1.2: Single-particle shell model orbitals relevant to the neutron-rich sulfur isotopes. The left hand side shows the energy levels given by a harmonic oscillator (HO) potential, and the right hand side includes the effect of a negative spin-orbit force, that splits each harmonic oscillator level in two, conventionally labeled $n\ell_j$. Each level can be occupied by $2j + 1$ particles of each nucleon type. The numbers in between large gaps in the single-particle levels are the magic numbers of nucleons.

first studies of ^{38}S in the 1980's [4, 5, 6]. Other transfer reactions, such as two-proton pickup from ^{40}Ar in the reaction ^{40}Ar(^{11}B,^{13}N)^{38}S [7], and two-neutron transfer with heavy ions using ^{36}S(^{14}C,^{12}C)^{38}S and ^{36}S(^{18}O,^{16}Oγ)^{38}S reactions [8] also obtained low-energy level scheme information. The heavier even-even sulfur isotopes could not be produced in sufficient quantities to study using nucleon transfer reactions, and since fusion-evaporation reactions are generally more amenable to neutron-deficient systems, further progress in studying these isotopes was difficult. It is notable that Fornal and coworkers were able to glean some γ rays belonging to ^{38}S from a re-analysis [9] of $\gamma\gamma$ coincidence data from binary reactions of ^{36}S+^{160}Gd, by gating on ^{158}Gd particles, and this method may hold some promise in reaching the high-energy levels in some neutron-rich nuclides. However, more direct means of accessing nuclei in order to use other experimental probes needed to await progress in radioactive beam development.

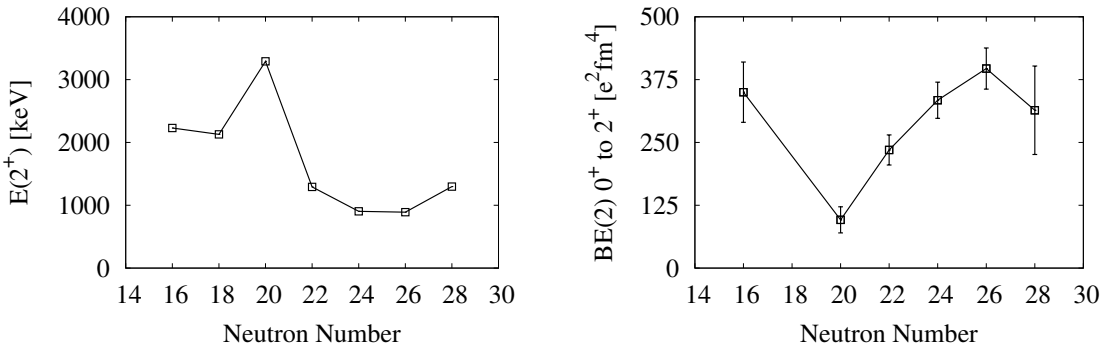

Figure 1.3: Previously measured 2^+ excited state energies (left) and B(E2; $0^+ \rightarrow 2^+$) values (right) for sulfur isotopes, as a function of neutron number. Data are taken from Refs. [10, 11] and [12]. Lines are drawn to guide the eye.

Fragmentation reactions can provide high yields of neutron-rich nuclides, and this technique made it possible for neutron-rich sulfur isotopes to be studied with intermediate-energy Coulomb excitation at the NSCL [13], yielding E(2^+) and B(E2) values for the first-excited 2^+ states in ^{38,40,42}S [10]. The Coulex measurements put on solid experimental ground the idea that the neutron-rich sulfur isotopes lie in a region of rapidly-changing nuclear structure [14, 15, 16]. The $N = 28$ nucleus ^{44}S was also studied with intermediate-energy Coulomb excitation, which provided a measurement of E(2^+) and the B(E2) to the first 2^+ state [11]. The results are summarized in Fig. 1.3. From the 2_1^+ energies, it appears that the nuclei become more collective as they approach midshell. This is confirmed by the increasing B(E2) values, which indicate that the heavy sulfur isotopes are becoming deformed as more neutrons are added on top of the spherical ^{36}S. Of particular interest is the behavior of the sulfur isotopes at the purported closed shell at $N = 28$, where some collectivity has been found to remain in ^{44}S [11]. Since the B(E2) value is proportional to the square of the proton deformation parameter β_2, the Coulomb excitation measurement was only able to establish that ^{44}S exhibits collectivity, and could not measure the sign of β_2 or tell whether the deformation is static or dynamic in nature.

Along with the Coulomb excitation studies, β-decay studies of ^{40}P were carried

out at the NSCL to study the level structure of ^{40}S [17], and proton inelastic scattering using a CH_2 target offered another probe of collectivity and deformation of the 2_1^+ state in ^{38}S [18].

In-beam γ-ray spectroscopy of neutron-rich sulfur isotopes was carried out following fragmentation reactions [19] at the GANIL facility in France. The workers in Ref. [19] were able to propose level schemes based on the γ-ray spectra, including the locations of 4^+ states, which in the case of ^{40}S contradicted the previous study by β-decay [17]. Nevertheless, the results of shell-model calculations and collective model calculations that explained the proposed level schemes indicated that the $N = 28$ shell closure weakens below $Z = 20$, and is probably eroded for $Z = 16$ since the proton subshell closure that is strong at $N = 20$ has evidently disappeared at $N = 28$, according to systematics of single-particle energies in the K isotopes [20]. Even though the measurement of higher-lying excited state energies can give an indication of the behavior of a nucleus within the framework of collective models, and can test shell model calculations, the results of Ref. [19] can be viewed as somewhat tentative until further confirmation of the level schemes is obtained. In general, the experimental data gathered so far leave an incomplete picture of the underlying causes for the transitioning nuclear properties of $^{36-44}$S.

The neutron-rich sulfur isotopes have been the subject of several theoretical investigations that have paralleled the experimental studies. Werner *et al.* [15] studied the heavy sulfur isotopes within the Relativistic Mean Field (RMF) framework and found that the potential energy surface of the neutron-rich sulfur isotopes is somewhat flat with respect to deformation, in general leading to nearly degenerate prolate ($\beta_2 > 0$) and oblate ($\beta_2 < 0$) shapes. Other calculations by the same workers using non-relativistic Skyrme Hartree-Fock (SkHF) techniques found nearly degenerate prolate-deformed and oblate-deformed solutions as well. The onset of deformation in the neutron-rich sulfur isotopes was confirmed by the Coulomb excitation studies of Refs. [10, 11] which found $|\beta_2| \sim 0.3$. Other theoretical studies followed Werner

and collaborators, where RMF studies using improved interactions also confirmed the theoretical presence of deformation [21, 22]. Shell model calculations were also undertaken by Retamosa and coworkers [20], and were later refined by Nummela *et al.* [23] and extended by Caurier, Nowacki, and Poves [24] to explain the B(E2) values and 2^+ excitation energies of the neutron-rich sulfur isotopes. The shell model studies also found the presence of deformation in the sulfur isotopes, and postulated strong shape coexistence at the $N = 28$ nucleus ^{44}S. Attention was beginning to shift to a larger nuclear physics question: the validity of the $N = 28$ magic number for neutron-rich nuclides with $Z < 20$. The RMF, SkHF, and shell model investigations, together with other studies including angular-momentum projected Generator Coordinate Method (AMPGCM) calculations of Rodriguez-Guzman *et al.* [25], all suggested that the $N = 28$ shell closure weakens below calcium.

The experimental as well as theoretical effort devoted to this region of the nuclear chart has been and continues to be significant. The conclusions about the nuclear structure that have been drawn are varied, largely because the physical interpretation of level energies and reduced transition probabilities are model-dependent, and many of the models used in the theoretical studies are insufficiently constrained by the available data. The lack of a consistent interpretation of the available data suggests that g-factor measurements, which stringently test nuclear models as will be shown in the next section, are crucial to aid in the understanding of the interplay between the migration of single-particle energy levels and the development of collectivity in the neutron-rich sulfur isotopes.

1.1.2 Open Questions

The changes in nuclear properties that have been observed for the heavy sulfur isotopes have left questions about their causes. In particular, the migration of the single-particle energy levels and their occupancies in this region are not well understood. Since the $N = 20$ energy gap has been crossed for the sulfur isotopes heavier than

^{36}S, it would be expected [5] that the addition of neutron pairs to form each successive even-even sulfur isotope would dominate the single-particle nature of the nuclear wavefunction, especially for ^{38}S which lies close to the $N = 20$ closed shell. On the other hand, the increase in collectivity that has been observed would tend to lower the role of single-particle effects as protons and neutrons become strongly coupled together to form excited states. There is a delicate interplay between collectivity and single-particle effects in nuclear excitations, and care is needed when drawing conclusions from excited-state energies and B(E2) values. In fact, since the B(E2) is a reduced matrix element between an initial and a final state, some ambiguities can arise in the determination of the nuclear properties. The g factor is not subject to such uncertainties since it is an observable of the properties of a single state. For this reason the onset of collectivity can be probed using $g(2^+)$ values to gain further insight into the single-particle contributions to the excited-state wavefunctions.

The large energy gap after neutron or proton number 20 is due to the *harmonic oscillator* closed shell consisting of the $d_{5/2}$-$s_{1/2}$-$d_{3/2}$ orbits (called the *sd* shell, see Fig. 1.2). The next level is the $f_{7/2}$ orbital, which has descended from the orbitals composing the pf shell due to the spin-orbit interaction, leaving an energy gap above it that causes the $N = 28$ magic number. The shell closure at $N = 28$ can be called a "spin-orbit closed shell" because it is primarily due to the spin-orbit force that there is a gap between the $f_{7/2}$ orbital and the pf shell. It had been suggested by Dobaczewski and collaborators [26] that the spin-orbit force weakens in nuclei with a large neutron excess — this would result in the raising of the $f_{7/2}$ orbit and the disappearance of the $N = 28$ shell closure. Single-particle effects are a result of large gaps in the single-particle energy levels, and for the single-particle behavior of the neutrons, the $N = 20$ and $N = 28$ shell gaps will clearly be the most important for the $^{38-44}$S isotopes. The proton single-particle behavior is most influenced by the proton $s_{1/2}$-$d_{3/2}$ gap. As neutrons begin to occupy the $f_{7/2}$ orbit, therefore changing the number of valence neutrons, proton-neutron interactions between the $f_{7/2}$ neutrons

and the *sd* protons can affect the energies of proton single-particle energy levels, in particular the proton $s_{1/2}$-$d_{3/2}$ gap [27]. It was suggested [28] that the mechanism of proton-neutron interactions that change strength with increasing neutron valence number is responsible for the changing structure of the sulfur isotopes, by eroding the $Z = 16$ subshell closure. In contradiction to the assertion in Ref. [28], a weakening of the $N = 28$ shell gap away from stability was recently proposed [19, 24] as the main cause of deformation in the neutron-rich sulfur isotopes. It will be shown that the g factor can separate the proton and neutron contributions to the nuclear wavefunction, which will enable the effects of the single-particle energy shifts, and the possible existence of shell closures, to be deduced in the sulfur isotopes.

The existence of shell closures at the traditional magic numbers toward the driplines is an open question, since many changes in shell gaps have already been observed. For example, the $N = 20$ shell closure has been found to soften for decreasing proton number below $Z = 16$, with clear evidence for non-magic behavior at the $Z = 12$ nuclide ^{32}Mg [29]. As was indicated previously, much attention has been focused on the $N = 28$ shell gap below calcium, since radioactive beam facilities have now provided experimental access to this region. It remains an open question as to whether some nuclides along the $N = 28$ line can be called "magic" nuclei, most notably ^{42}Si, which has been the subject of conflicting claims from β-decay studies [30] and from nucleon knockout measurements [31]. Cottle and Kemper had suggested [32] that spectroscopy of $Z = 14$ ^{42}Si would give a definitive answer about the possibility of the $N = 28$ magic number below $Z = 20$, rather than measurements in the neutron-rich sulfur isotopes; their reasoning is that the effect of the disappearing $Z = 16$ subshell closure is strong, but is limited to the sulfur chain. Since an excited-state g-factor measurement probes the nuclear wavefunction in a way that allows an elucidation of neutron *and* proton behavior (including orbital occupancies and shell gaps), g-factor measurements offer a means to search directly for the persistence of the $N = 28$ shell closure in the sulfur isotopes.

1.2 Electromagnetic Moments of Nuclei

Electromagnetic multipole moments are categorized as either electric or magnetic moments. Electric multipole moments arise from the distribution of electric charge within the nucleus, and magnetic moments arise from the distribution of currents and magnetization. Calling the charge density within the nucleus $\rho(\mathbf{x}')$, the potential $\Phi(\mathbf{x})$ outside the region of the nucleus can be expanded in a series of spherical harmonics. Following Jackson [33],

$$\Phi(\mathbf{x}) = \sum_{l=0}^{\infty} \sum_{m=-l}^{l} \frac{4\pi}{2l+1} E_{lm} \frac{Y_{lm}(\theta,\phi)}{r^{l+1}}, \tag{1.1}$$

where the values E_{lm} are the coefficients of the expansion, to be calculated from $\rho(\mathbf{x}')$. The E_{lm} coefficients are found by equating Eqn. 1.1 with the explicit expression for the electrostatic potential,

$$\Phi(\mathbf{x}) = \int \frac{\rho(\mathbf{x}')}{|\mathbf{x}-\mathbf{x}'|} d^3x', \tag{1.2}$$

for which the term $1/|\mathbf{x}-\mathbf{x}'|$ can be expanded using

$$\frac{1}{|\mathbf{x}-\mathbf{x}'|} = 4\pi \sum_{l=0}^{\infty} \sum_{m=-l}^{l} \frac{1}{2l+1} \frac{r'^l}{r^{l+1}} Y^*_{lm}(\theta',\phi') Y_{lm}(\theta,\phi), \tag{1.3}$$

yielding

$$\Phi(\mathbf{x}) = 4\pi \sum_{l,m} \frac{1}{2l+1} \left[\int Y^*_{lm}(\theta',\phi') r'^l \rho(\mathbf{x}') d^3x' \right] \frac{Y_{lm}(\theta,\phi)}{r^{l+1}}. \tag{1.4}$$

The quantities in brackets are the E_{lm}'s, known as the electric *multipole moments*,

$$E_{lm} = \int r'^l Y^*_{lm}(\theta,\phi) \rho(\mathbf{x}') d^3x'. \tag{1.5}$$

Since the nucleus is a quantum system, Eqn. 1.5 must be cast into a quantum mechanical form using $\rho(\mathbf{x}) = \sum_{i=1}^{Z} e|\psi_i|^2$. In a classical picture, magnetic multipole

moments can be defined in a manner analogous to Eqn. 1.5, as

$$M_{lm} = \int r'^{l} Y^*_{lm}(\theta, \phi) \rho_M(\mathbf{x}') d^3x', \tag{1.6}$$

where the magnetic density is $\rho_M(r) = -\nabla \cdot \mathcal{M}(r)$, with $\mathcal{M}(r) = \mathcal{M}_c(r) + \mathcal{M}_s(r)$ is the sum of contributions from electric currents and intrinsic spin of the nucleons [34]. The current density comes from the motion of the protons, leading to contributions of the form $r \times p$, which is their orbital angular momentum. The spin contributions arise from contributions of the neutrons as well as the protons, since both particle types carry intrinsic spin.

For symmetry reasons, the nucleus can not possess odd-rank static electric moments or even-rank magnetic moments, and indeed those moments (electric dipole, magnetic quadrupole, etc.) have been found experimentally to be vanishingly small. The electric monopole (E0) moment is simply the nuclear electric charge. The only higher electromagnetic moments experimentally established in nuclei are the magnetic dipole (M1), electric quadrupole (E2), and magnetic octupole (M3), with some evidence pointing to the existence of the electric hexadecapole (E4) moment, although the effects of the higher-order moments rapidly diminish with increasing rank. The magnetic dipole and electric quadrupole moments are the most important for describing nuclear structure. The electric quadrupole moment represents the deviation of the nuclear charge from a spherical shape. The existence of the magnetic dipole moment means that electric currents and magnetization are present within the nucleus, which indicates that the nucleus possesses internal structure. The classical definition of the magnetic dipole moment is $\mu = \int \mathcal{M}(\mathbf{x}') d^3x'$. Quantum mechanically, the contributions to $\mathcal{M}(\mathbf{x})$ from the current and spin terms can be written in terms of the angular momentum and spin operators, ℓ and s, which will be explained further in the context of the nuclear shell model.

When a magnetic dipole moment is immersed in a magnetic field, a torque ($\tau =$

$\mu \times b$) is exerted on the magnetic moment that causes a rotation with frequency

$$\omega = g\frac{\mu_N}{\hbar}B, \tag{1.7}$$

which is the Larmor precession formula for a nucleus in a magnetic field of strength B. The usual unit for nuclear magnetic moments is the *nuclear magneton*, $\mu_N = e\hbar/2m_p \approx 5.051{\cdot}10^{-27}$ J/T (m_p is the proton mass). The quantity g is the *gyromagnetic ratio*, defined as the proportionality constant between the value of the magnetic moment and the nuclear spin,

$$\mu = g\mu_N I. \tag{1.8}$$

It will be shown that the numerical value of g contains information on the nuclear wavefunction. A measurement of the Larmor frequency in Eqn. 1.7 is the principle on which most techniques for measuring magnetic moments are based. The frequency depends on the *product* of the field strength and the g factor, as can be seen from Eqn. 1.7. Extraction of the g factor therefore relies on the knowledge or measurement of the magnetic field strength.

The nucleons (protons and neutrons) are the constituents of nuclei, and they have their own complex internal structure. This structure gives the proton and neutron magnetic dipole moments, which possibly arise from the distribution of quark currents and magnetization within the nucleons, although at present these are not fully understood. The nucleon magnetic moments have been measured for the free proton and neutron, with the resulting nominal values [35]

$$\mu = \begin{cases} +2.793\ \mu_N & \text{for protons} \\ -1.913\ \mu_N & \text{for neutrons,} \end{cases} \tag{1.9}$$

known at present to a precision of $\Delta\mu/\mu \sim 10^{-7}$ for the neutron and 10^{-8} for the proton. It is the large difference (in both sign and magnitude, see Fig. 1.4) of the

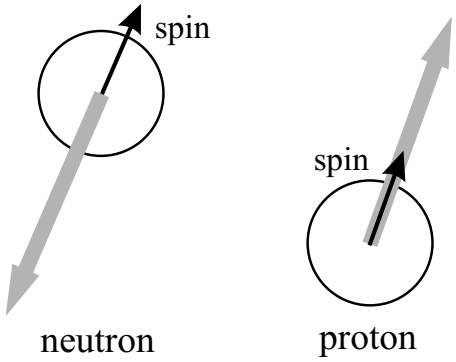

Figure 1.4: Proton and neutron magnetic dipole moment vectors (thick grey arrows) and the proton and neutron spins (thin black arrows).

neutron and proton magnetic moments that makes the nuclear magnetic moment such a sensitive probe of the internal arrangement of neutrons and protons within the nucleus, since the magnetic moments of the individual nucleons combine to produce the total nuclear magnetic moment. A measurement of the nuclear magnetic moment therefore gives insight into the particular way neutrons and protons are behaving in a nuclear state of interest. It is useful to interpret the magnetic moment of a nucleus in terms of a particular model in order to gain insight into the structure of the nucleus. Two broad classes of models, which generally predict very different g factors, are used to interpret magnetic moments. Microscopic-type models, like the shell model, focus on the motions of the individual constituent nucleons. In contrast, macroscopic collective models focus on the bulk properties of the whole nucleus. Brief introductions to the different approaches will be given in the following two sections.

1.2.1 Magnetic Dipole Moments in the Shell Model

One of the most interesting aspects of the nuclear system is its many-body nature. In contrast to atomic systems, the nucleons interact very strongly with each other, and this has interesting consequences. In close analogy to electrons, the nucleons are spin 1/2 particles which must obey the Pauli Exclusion Principle. The consequence of this principle and the nucleon-nucleon interactions within the nucleus are nuclear

properties that show a periodic shell structure reminiscent of the atomic structure seen in the Periodic Table of the Elements. A successful nuclear shell model exists that can explain many of these properties for the stable nuclides.

Shell model wavefunctions are obtained by assuming initially that the nucleons are moving inside an average potential well created by all of the nucleons, called the "mean field." Modern shell model calculations also take into account the residual nucleon-nucleon interactions. In the extreme single particle shell model, the single-particle wavefunctions can be obtained by solving the Schrödinger equation with the mean field potential, and energy levels for particles with quantum numbers (n, ℓ, j) result. The quantum number n represents the number of nodes in the radial wavefunction, ℓ is the orbital angular momentum, and j is the total angular momentum that results from coupling the intrinsic nucleon spin $s = \frac{1}{2}$ to the orbital angular momentum to obtain the two possibilities $j = \ell \pm \frac{1}{2}$. The nuclear potential generally has a Woods-Saxon shape, and during the development of the shell model, a spin-orbit term $(-\ell \cdot s)$ was added [36, 37] in order to account for the experimentally-determined "magic numbers" which correspond to large gaps in the single-particle energy levels. Since nucleons fill the lowest energy levels first and obey the Pauli principle, nucleons are added to a particular (n, ℓ, j) level until the maximum of $2j + 1$ protons or neutrons is reached. Additional nucleons must then begin to occupy higher-lying states. This means that in some cases, certain nuclides with A nucleons can exhibit an extra degree of binding relative to that of the nuclide with $A + 1$ nucleons. Empirically, these magic nucleon numbers are found in stable nuclei to be 2, 8, 20, 50, 82, and 126, for either the proton[1] number Z or the neutron number N. Certain nuclei that have magic numbers of both their protons and neutrons are termed *doubly magic* (such as ^{4}He and ^{16}O), which are extremely tightly-bound systems. It is not true that the magic numbers are universal for all possible combinations of Z and A, because they depend on the

[1]No nuclide has been found to exist with as many protons as 126. Such an isotope could lie beyond the limits of nuclear existence, or perhaps is simply unreachable with current experimental techniques.

ordering and relative spacing of the energy levels caused by the nuclear potential well and nucleon-nucleon interactions, which can change with nucleon number. It is one of the main goals of nuclear physics to observe and attempt to explain this change, in particular for nuclides far removed from stability.

A magnetic dipole moment arises from contributions from the orbital and intrinsic spins of the protons and neutrons that make up a particular nucleus, in the same way that the nuclear spin does (the two quantities are closely connected, as seen in Eqn. 1.8). The quantum-mechanical magnetic moment operator is given by

$$\mu = \mu_N \sum \left[g_\ell \ell + g_s s \right], \tag{1.10}$$

where the sum runs over all nucleons in the nucleus, for which the orbital g factor g_ℓ equals 1 for protons and 0 for neutrons, ℓ is the orbital angular momentum and s is the intrinsic spin. The spin g factors, g_s, are identical to the nucleon g factors, obtained from Eqn. 1.9 by dividing by the nucleon spin, 1/2:

$$g_s = \begin{cases} +5.586 & \text{for protons} \\ -3.826 & \text{for neutrons.} \end{cases} \tag{1.11}$$

The magnetic dipole moment is a sensitive probe of the single particle nature of nuclear states, since the operator involves terms that depend on the coupling of ℓ and s, and sums over all the nucleons composing the nucleus. The fact that the proton and neutron g factors are different in both sign and magnitude means that the nuclear g factor can change significantly with ℓ and j, as well as with particle type, which means that shell model calculations using different interactions or model spaces can be stringently tested.

Using the operator in Eqn. 1.10, the magnetic moment can be obtained from a nuclear wavefunction by calculating its expectation value for the wavefunction of the

$m = I$ substate,

$$\langle I\, m{=}I|\, \mu\, |I\, m{=}I\rangle. \tag{1.12}$$

A single-particle state with a particular j gives rise to a particular magnetic moment due to the operators ℓ and s contained in Eqn. 1.10. Since this is the sum of two angular momenta, one must obey angular momentum algebra in determining the result. Following Brink and Satchler [38], the addition theorem for the g factor of a state I that is the result of summing two angular momenta I_1 and I_2, with g factors g_1 and g_2, is

$$g = \frac{1}{2}(g_1 + g_2) + \frac{1}{2}(g_1 - g_2)\frac{I_1(I_1+1) - I_2(I_2+1)}{I(I+1)}. \tag{1.13}$$

The addition theorem can be applied using $g_1 = g_\ell$, $I_1 = \ell$, $g_2 = g_s$, $I_2 = s$, and $I = j$, to obtain the g factor of a particle in an orbital with angular momentum $j = \ell \pm \frac{1}{2}$ in a compact form [39]:

$$g_j = g_\ell \pm \frac{g_s - g_\ell}{2\ell + 1}. \tag{1.14}$$

Using Eqn. 1.14, simplified predictions can be made for the ground state magnetic moments of odd-mass nuclei within the "extreme single-particle model" which assumes that all protons and all neutrons form spin–0 pairs, and the remaining unpaired nucleon is responsible for the spin and magnetic moment of the odd-mass nucleus. The predicted magnetic moments for odd-mass nuclei are called the *Schmidt limits* because the experimentally measured values generally lie in between the $j = \ell + 1/2$ and $j = \ell - 1/2$ values given by Eqn. 1.14 (see Fig. 1.5). In reality, the magnetic moments usually deviate from these extreme predictions by a factor of about 0.6. The reason for the deviation is that the model is not realistic enough. Usually, effective g factors are used to provide a correction for missing interactions in the Hamiltonian, and $g_s^{\text{eff}} \approx 0.6 g_s^{\text{free}}$ is often used, and there can be corrections for g_ℓ as well. Modern

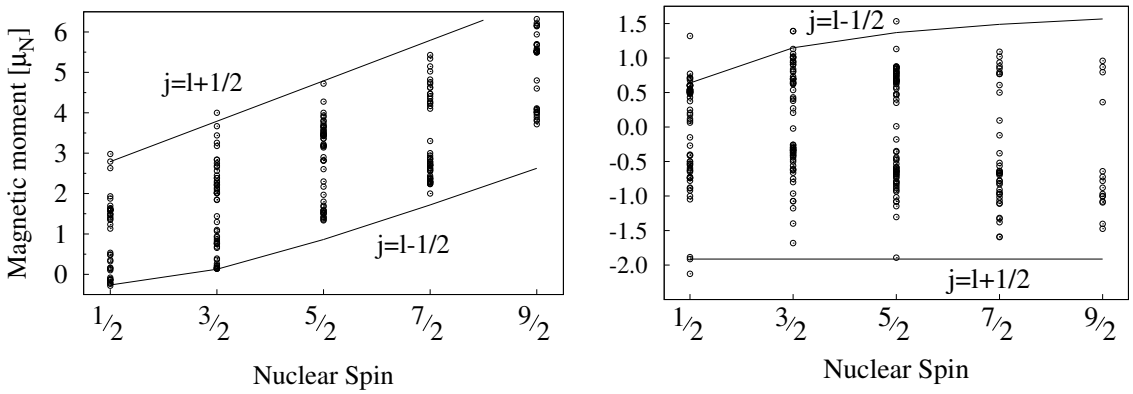

Figure 1.5: Measured magnetic dipole moments in odd-proton nuclides (left), odd-neutron nuclides (right), and Schmidt predictions (lines). Data are from Ref. [43].

shell model calculations such as those of Brown [40] or Caurier and coworkers [41] have prescriptions for including such corrections, and more details can be found in the literature [42, 39].

The Schmidt prediction in Eqn. 1.14 shows that the g factor can change sign depending on whether the particle is a proton or a neutron (because of their respective spin g factors), and depending on whether the orbit is one with $j = \ell$+1/2 or $j = \ell$–1/2 (because of the $\pm$ sign in Eqn. 1.14). A measurement of the *sign* of the g factor is very useful; this information can often establish the type of particle that is dominating the nuclear structure. The magnitude of the g factor can be used to sort out the relative contributions of the protons and neutrons to the wavefunction of a nuclear state.

1.2.2 $g(2^+)$ in Even-even Nuclei

Even-even nuclei always have zero ground state spin and therefore no ground state magnetic dipole moment. Excited states in even-even nuclei, however, can have finite spin and therefore are expected to have magnetic moments. The situation can be more complicated than in odd mass nuclei, that can be thought of as an inert core with an unpaired nucleon that is responsible for the spin and magnetic moment. In particular, the first excited state of most even-even nuclei has spin 2. The spin-2

state can be assembled from the single particles in many ways, such as promoting a pair of nucleons to a higher-energy orbit, breaking a pair and promoting one nucleon to another level, or by simply recoupling a pair of nucleons within the same j level to angular momentum $J = 2$. In all cases, the addition theorem can be used to obtain predictions for the g factor of such configurations, with especially simple results for identical particles in the same j orbital, where $g(J) = g(j)$. Therefore, within the context of the shell model, a g factor can be useful to determine the nucleon configuration for both the protons and the neutrons in an excited state. It is rarely only a single particle (or a single pair of particles) that make up the excited state wavefunction; for certain nuclei – most notably those with very large quadrupole deformation – the participation of a very large number of nucleons is needed to explain the large transition probabilities $\big($B(E2) values$\big)$ that can be 10-100 times larger than what would be expected from a few single-particle excitations. In the following, the example of a hydrodynamical picture is used to give a crude estimation of a collective g factor.

Hydrodynamical Model

In contrast to the shell model, which treats the nucleus on a microscopic basis by considering the interactions among the constituent nucleons, the nucleus can be treated as nuclear matter, similar to a liquid drop or a rigid body. Such systems, in which all the nucleons act together, are termed *macroscopic* or *collective*. Macroscopic models such as the liquid drop model [44] and the collective Bohr model [45] can describe many features of deformed nuclei, which tend to show characteristic patterns of rotation or vibration. Rather than describing the details of the various collective models, it is more useful in this context to discuss the excited-state g factors that result from these models. In particular, a hydrodynamical treatment of the nucleus as a rotating charged fluid predicts $g \sim +Z/A$, and this value serves as the canonical "collective" prediction for excited-state g factors although it is not clear that a real nucleus (even

one that is a good rotor) should behave in this fashion. A brief justification for the Z/A result will be given here.

The classical gyromagnetic ratio of an object is the ratio of its magnetic moment to its angular momentum. Using elementary electrodynamics, the expected gyromagnetic ratio can be calculated for a simplified version of the nucleus: a uniformly-charged rotating sphere. Let the sphere have mass Am_p and charge Ze distributed uniformly throughout its volume $\frac{4}{3}\pi R^3$, where R is the radius of the sphere. Then, for a rotational frequency ω, the sphere will have angular momentum $\mathcal{I}\omega$, with the moment of inertia $\mathcal{I} = \frac{2}{5}MR^2$. Therefore, the denominator of the gyromagnetic ratio is equal to $\frac{2}{5}Am_pR^2\omega$. The magnetic moment of the charged rotating sphere is calculated by recalling the result for the magnetic moment of a current loop, $\mu_{loop} = Ia$, where I is the current and a is the area enclosed by the loop. Using cylindrical coordinates with the z axis along the axis of rotation, a succession of current loops can form disks lying in planes of constant z, with radii corresponding to the cylindrical radius of the sphere, $r(z) = \sqrt{R^2 - z^2}$. These disks will have magnetic moments $d\mu_{disk}(z)$, which can add together to form a sphere with a resulting magnetic moment μ_{sphere}. The electric charge in a loop of radius r is $2\pi r\lambda$, where $\lambda = \rho\, dz\, dr$ is the charge per unit length and ρ is the volume charge density. So the current can be written as

$$dI = \frac{2\pi r\lambda}{2\pi/\omega} = r\omega\rho\, dz\, dr,$$

using the time for one revolution of $2\pi/\omega$, and for a loop of radius r one obtains

$$d\mu_{loop}(r) = Ia = \pi\omega\rho r^3 dz\, dr.$$

The magnetic moment of the sphere is obtained by integrating the current loops out to the cylindrical radius of the sphere, and then integrating over the z coordinate

from $z = -R$ to $z = +R$. This can be expressed as

$$\begin{aligned} \mu_{sphere} &= \pi\omega\rho \int_{-R}^{+R} dz \int_{0}^{\sqrt{R^2-z^2}} dr\, r^3 \\ &= \frac{4}{15}\pi\omega\rho R^5 \\ &= \frac{3}{15} Ze\omega R^2. \end{aligned} \tag{1.15}$$

By taking the ratio of Eqn 1.15 and the angular momentum one can obtain the classical gyromagnetic ratio of a charged rotating sphere:

$$g_{class} = \frac{\mu_{sphere}}{J_{sphere}} = \frac{\frac{1}{5}Ze\omega R^2}{\frac{2}{5}Am_p\omega R^2} = \frac{Z}{A} \cdot \frac{e}{2m_p}. \tag{1.16}$$

Thus the classical result for a charged rotating sphere shows a Z/A dependence, expressed in units of $e/2m_p$, the classical analog of the nuclear magneton.

The collective models based on classical rotators or surface vibrations tend to predict g factors near $+Z/A$. For rotational nuclei, this is indicative of how much of the angular momentum is carried by the protons with respect to the entire nucleus [46]. Vibrational nuclei also have a g factor of Z/A that is dominated by the orbital motion of the particles [45]. It is very significant that in collective models, the spin contributions of the nucleons are ignored. In the rare-earth mass region, calculations performed by Prior and coworkers [47] showed that the contributions from the spins of the nucleons are small and generally cancel. It is not clear if the spin contributions are small universally across all mass regions and N/Z ratios, since few excited-state g factors have been measured off the line of stability.

1.3 Organization of Dissertation

The merits of g-factor measurements for elucidating the structure of the nuclear state wavefunctions have been presented in this Chapter, along with the background of the

sulfur isotopes that are the subject of this dissertation. Since no existing technique was clearly suited to measuring $g(2^+)$ values of picosecond-lifetime excited states in nuclei produced as fast fragments (which at present is the most accessible means of obtaining the neutron-rich sulfur nuclei), a new technique needed to be developed. This thesis concerns the development of a suitable technique and its application to the transitional isotopes ^{38}S and ^{40}S. The method is called the High Velocity Transient Field (HVTF) technique and is presented in Chapter 2. The experimental realization of the technique at the National Superconducting Cyclotron Laboratory is described in Chapter 3. Results of HVTF g-factor measurements of the first-excited states of neutron-rich ^{38,40}S are reported in Chapter 4, as well as the outlook for further radioactive fast-beam magnetic moment measurements.

Chapter 2

Transient Field Technique

It was recognized by Brady & Deutsch [48] early in the development of the theory of the angular distribution of radiation that a nucleus may be perturbed by external fields prior to the emission of radiation. In the case of a magnetic interaction between the nuclear magnetic moment and a magnetic field existing at the site of the nucleus, the perturbation takes the form of a Larmor precession of the nuclear spin about the magnetic field axis, with the precession frequency given by Eqn. 1.7. Since nuclear radiation is emitted in a characteristic angular pattern measured with respect to the nuclear spin axis, a precession of the nuclear spin causes a change in the orientation of the angular distribution of radiation by an amount proportional to the product of the field strength and the g factor of the nuclear state, as seen by the following. Rewriting Eqn. 1.7 using $\omega = \Delta\theta/\Delta t$ yields

$$\Delta\theta = -g\frac{\mu_N}{\hbar}B_{ext}\Delta t, \tag{2.1}$$

where the negative sign (due to the interaction $H = -\mu \cdot B$), indicates that the spin precession proceeds in the direction of the torque $\tau = \mu \times B$. The average magnetic interaction time is the excited-state lifetime, $\Delta t = \tau(2^+)$. Since the g factor is generally of order unity, the ratio $\mu_N/\hbar$ has approximately the value 48 MHz/T, and

the 2^+ states of interest have lifetimes in the picosecond range (1 ps = 10^{-12} s), the magnetic field needs to be of order kiloTesla in order to induce a detectable precession (of order milliradians). Such a field cannot be provided by laboratory magnets, and the strongest static hyperfine fields present at the site of nuclei embedded in ferromagnetic materials are generally ∼100 T. It was found, however, that the hyperfine magnetic field experienced by ions swiftly traversing ferromagnetic materials is generally on the order of kiloTesla. Since this phenomenon occurs only while ions are in motion, it was called the *transient* field.

The transient field was discovered in the late 1960's [49, 50] when it was found that static-field induced precessions were affected if the ion under study first recoiled into a ferromagnet and later came to rest, where it experienced a static hyperfine field. It became apparent that ions precess at a different rate while slowing down in the ferromagnetic material, compared to the spin precession expected from the known static hyperfine field in the material. An intensive study of the properties of the transient field initiated shortly after the observation of the transient field phenomenon. The investigation of the transient field resulted in the development of the transient-field technique to measure short-lived excited-state g factors for states produced in nuclear reactions, since reaction products often have a significant amount of kinetic energy after the reaction and can recoil into a ferromagnetic medium by a suitable design of the target. An early review [51] was made by Benczer-Koller, Hass, and Sak in 1980, which contains an authoritative history of the progress made in understanding the behavior of the transient field, as well as a description of experimental techniques using the transient field. For a review encompassing many of the modern developments, see Ref. [52]. An outline of the transient field technique, including a sophisticated combination of Coulomb excitation in inverse kinematics with the transient field, will be presented in this Chapter. An overview of a typical experimental arrangement is shown in Fig. 2.1, which is taken from Ref. [53].

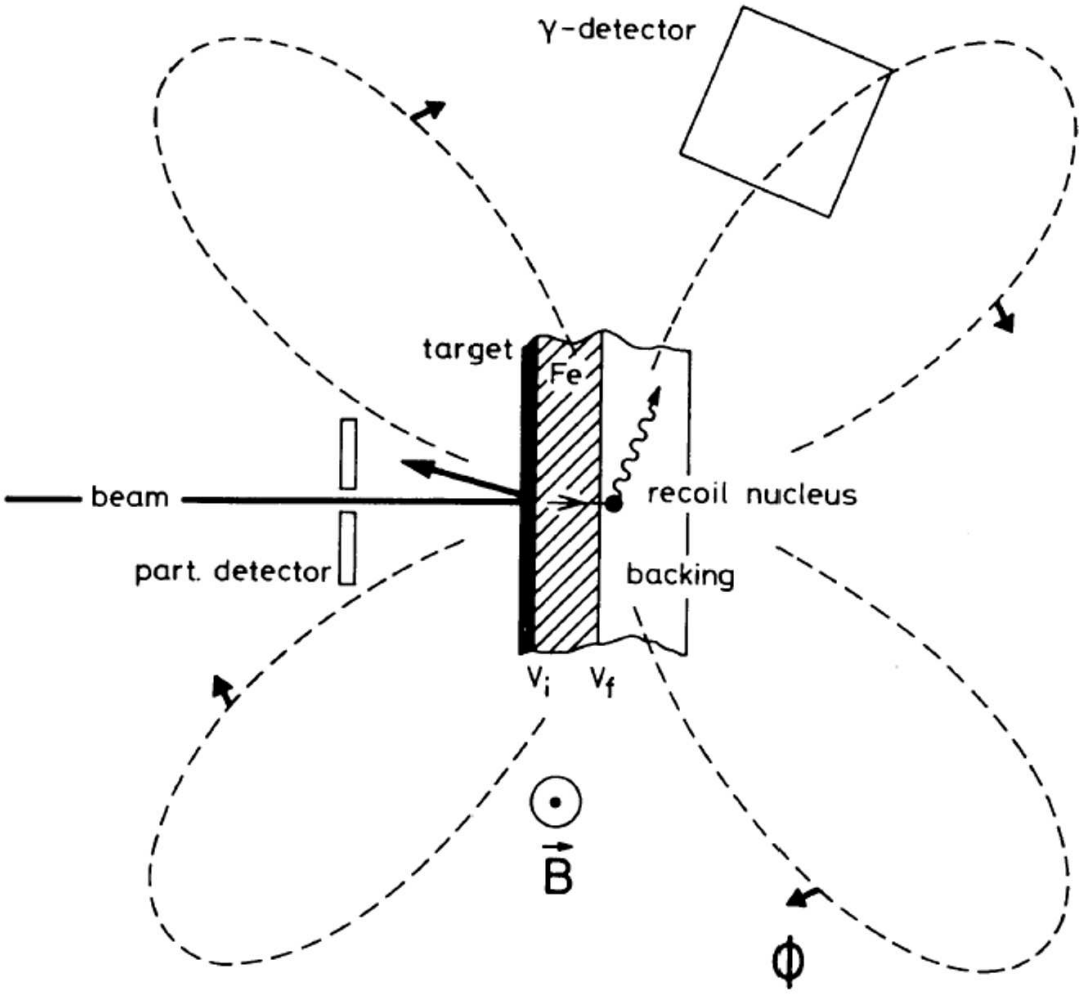

Figure 2.1: Transient field experimental concept, from Ref. [53]. In this arrangement, the beam enters through the hole in an annular particle detector and impinges on the target layer of the multilayer target. The beam can backscatter near 180° after Coulomb exciting a target nucleus, causing the target nucleus to recoil through the Fe layer, where it experiences the transient field. The dashed line is the γ-ray angular distribution, with the direction of precession shown by the arrows for a magnetic field directed out of the page, and a positive g factor. Placement of a γ-ray detector at the angle of maximum slope of the angular distribution (as shown) maximizes the sensitivity of the measurement.

2.1 Measurement Principles: Stable Beams

Nearly all of the techniques for measuring nuclear magnetic moments involve immersing the nucleus in a magnetic field (which may be provided by a laboratory magnet or via the internal fields in a molecular or solid-state environment), and measuring the interaction between the magnetic moment of the nuclear state and the external magnetic field, as expressed in Eqn. 1.7. A natural means of accomplishing a measurement of the magnetic interaction (the Larmor precession) that takes place while the nucleus is in an excited state is to measure a *perturbed angular correlation*[1]) (PAC) of de-excitation γ rays from the nuclear state of interest; this forms the basis of the transient field technique. One method, Time-Differential Perturbed Angular Distribution (TDPAD), measures the intensity variation of the γ rays emitted into a particular solid angle as a function of time, which directly results from the nuclear spin axis "sweeping past" the γ-ray detector at the Larmor precession frequency. In practice, TDPAD typically requires a nuclear excited-state lifetime longer than a few nanoseconds in order to allow at least one nuclear spin revolution to occur. If the nuclear lifetime is less than a nanosecond, it is not practical to use time-differential methods, and an integral method is usually used. Time-Integrated Perturbed Angular Distribution (IPAD), the category to which the transient field technique belongs, detects not the frequency of precession but the angular degree of precession that a nuclear spin turns within a set time interval, often its lifetime in a particular state. All PAC/PAD techniques require nuclear *spin alignment*, in addition to knowledge of the field strength in order to extract the g factor.

[1]Another term, used almost synonymously with PAC, is *perturbed angular distributions* (PAD), where the former usually refers to measuring the angle between successive γ rays in a coincidence measurement, and the latter usually refers to measuring the angular distribution of γ rays with respect to the beam axis or the direction of a particle associated with the population of the state that emits the γ ray. This dissertation uses the term "angular distribution" to mean the measurement of γ rays with respect to the beam axis, which also corresponds to the associated particle direction.

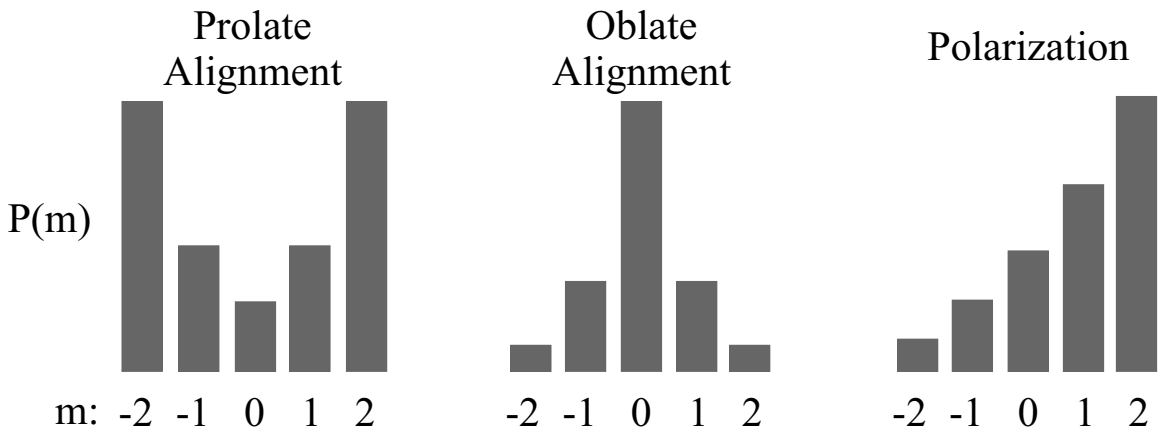

Figure 2.2: Examples of different types of nuclear orientation, shown as the relative populations of different magnetic substates for an $I = 2$ nucleus. Both types of alignment are symmetric about the $m = 0$ substate, while polarization is asymmetric.

2.1.1 Angular Distribution from Spin Alignment

To obtain information on the spin precession that is proportional to the g factor, excited-state spin alignment is necessary in order to allow a directionally-anisotropic emission of γ rays from the state of interest. Spin-aligned states (meaning an ensemble of nuclei with an unequal population of magnetic substates, i.e. $P(m) = P(-m)$ but $P(m) \neq P(n)$, where n is any other magnetic substate; see Fig. 2.2) can be populated with compound nuclear reactions, direct transfer reactions, or Coulomb excitation (for example), when there is a preferred axis in the reaction geometry. If the details of the reaction are known, it is possible to calculate the exact distribution of magnetic substates and therefore predict the directional emission of γ rays from the excited states formed in the reaction. It is difficult to calculate the m-state population distribution with much accuracy for most nuclear reactions because the interaction is not completely understood. However, since the electromagnetic interaction is very well understood, Coulomb excitation is a case where the m-state populations can be very accurately calculated. This makes Coulomb excitation (presented in § 2.3.1) an excellent means of preparing excited states which will decay by γ-ray emission with a known directional distribution.

Fig. 2.1 illustrates the angular distribution for head-on Coulomb excitation of the 2_1^+ state of an even-even nucleus, where the beam is used to excite a target nucleus. The experimental arrangement requires the detection of a beam particle scattering backward at near 180° with respect to the beam axis, causing the excited target nucleus to recoil forward into the ferromagnetic layer that provides the transient field. In such an arrangement, the angular distribution of γ rays has a characteristic four-lobe shape due to the preferred population of $m = 0$ substates in a backscattered geometry. The degree of spin precession can then be measured by detecting a change in the γ-ray count rate at a known angle in the angular distribution, for which the slope of the angular distribution with respect to θ is known. Generally, several detectors are used in order to measure the γ-ray angular distribution and characterize the slope. The angular distribution measurement becomes especially important when the excited state is populated by a compound-nucleus or transfer reaction and the m-substate population distribution is not known. For Coulomb excitation, the substate populations can be calculated from the well-known theory and a measurement at several angles is important mainly to confirm the calculations and to ensure that the system behaved as expected.

Formalism of Angular Distribution of γ Rays

A γ ray is typically emitted by a nucleus as it transitions from one state of angular momentum I_i and definite parity, to another state of angular momentum I_f, which also has definite parity. The γ ray carries away the energy difference between the two nuclear states, and it is also responsible for the possible changes in angular momentum and parity. Due to the way that the photon electromagnetic fields couple to angular momentum, the emission direction of the γ ray has a relationship to the direction of the initial nuclear state's spin axis [54]. This relationship is expressed analytically as an angular probability distribution, which only has experimental meaning in the context of an ensemble of nuclei rather than only one nucleus. If the nuclei are oriented

randomly in space, then all of their γ-ray angular probability distributions will overlap to make an isotropic distribution. However, if the ensemble of nuclei is aligned along a particular axis, then the γ rays emitted from the ensemble may show an anisotropy in space with respect to that axis.

The theory of the angular distribution of radiation has been developed through an examination of the effect the angular momentum change has on the direction of the emitted radiation. Several references [55, 56, 57, 58] describe this formalism, and a brief description of the practical details will be given here. For the case of axial symmetry about the beam axis, it is most convenient to express the angular distribution as an expansion in terms of Legendre polynomials, and within the formalism of angular distributions, the coefficient for each term in the series is calculable. The angular distribution is written as

$$W(\theta) = \sum_{k=0}^{k_{max}} a_k P_k(\cos\theta), \tag{2.2}$$

and it remains to determine the coefficients a_k and the number of terms in the series. The emission of γ radiation is caused by the electromagnetic interaction, which conserves parity. The conservation of parity implies that the emitted radiation should not contain information about the *direction* of the nuclear spin, but rather should only have information about the nuclear spin *axis*. In other words, the angular distribution should be a function of the angle between the γ ray and the orientation axis, but should not be different if $\theta = 0^\circ$ and $\theta = 180^\circ$ are interchanged. Functions with that property must be symmetric about 90°. The Legendre polynomials $P_k(\cos\theta)$ for odd k are not symmetric about 90°, but the even-ranked $P_k(\cos\theta)$ are symmetric. Therefore, the angular distribution is described only with even values[2] of k. It will be shown shortly that a γ-ray angular distribution depopulating a 2^+ state is completely

[2]The decay of a nucleus by the emission of a β particle is governed by the weak interaction, which violates parity, and $W_\beta(\theta)$ is written using the odd-k Legendre polynomials.

described by terms with $k = 0, 2, 4$, and can be written as

$$W(\theta) = 1 + G_2 B_2 F_2 Q_2 \, P_2(\cos\theta) + G_4 B_4 F_4 Q_4 \, P_4(\cos\theta), \tag{2.3}$$

where the coefficients a_k are expressed as factors that separate the various physical contributions to the final angular distribution. The factors come primarily from details of the γ ray itself (F_k depends on the multipolarity and electric or magnetic character of the γ ray, and the spins of the initial and final states) and the degree of initial nuclear alignment (specified by the substate populations $P(m)$, from which the orientation parameters B_k are obtained). Also affecting the experimentally-observed angular distribution is the finite angular resolution of the γ-ray detectors (instead of observing $W(\theta)$ at an exact angle θ, the finite opening angle of the detector averages over a range of θ, which can "wash out" some of the effect), represented by the Q_k factors. An additional effect is due to hyperfine interactions that reduce the orientation of the nucleus if it leaves the target carrying electrons, prior to emitting the γ ray. The hyperfine interaction introduces "attenuation coefficients" G_k that depend on the state of ionization of the projectiles emerging into vacuum [59]. The G_k values will be discussed along with the analysis of the γ-ray angular distribution obtained in this work.

The degree of nuclear alignment is a measure of the relative populations of the magnetic substates, and plays a key role in the anisotropy of a γ-ray angular distribution. A convenient way of treating an ensemble of oriented states (such as the excited states resulting from Coulomb excitation) is to use density matrix formalism. The density matrix is a way to organize all the information necessary to completely specify the state of a quantum-mechanical system. In the present application, that consists of the normalized populations of the magnetic substates, using the beam axis as the quantization axis. The density matrix ρ can be decomposed into multipole terms that affect separate k terms in the angular distribution series. These multipole

terms are called "statistical tensors" ρ_{kq}, and in the case of axial symmetry (when the particles are detected symmetrically about the beam axis) only the $q = 0$ terms are needed:

$$\rho_{k0} = \frac{\hat{I}}{\hat{k}} \sum_{m=-I}^{I} (-)^{I+m} \langle I\, -m I m | k0 \rangle P(m). \tag{2.4}$$

where the symbol $\hat{x} \equiv \sqrt{2x+1}$. In the angular distribution series, the statistical tensors are contained in the B_k orientation parameters by the relation $B_k = \sqrt{2k+1}\rho_{k0}$. The Clebsch-Gordan coefficients vanish unless $k \leq 2I$, showing that higher-order terms are not needed to describe the angular distribution completely. The Clebsch-Gordan coefficients can be written explicitly for $I = 2$ and $k = 2, 4$ to obtain

$$\begin{aligned} \rho_{20} &= \frac{1}{3\sqrt{14}} \sum_{m=-2}^{2} [3m^2 - 6] P(m), \quad \text{and} \\ \rho_{40} &= \frac{1}{36\sqrt{14}} \sum_{m=-2}^{2} [35m^4 - 155m^2 + 72] P(m). \end{aligned} \tag{2.5}$$

Since $P(m) = P(-m)$ from the definition of alignment, these expressions can be further simplified to

$$\begin{aligned} \rho_{20} &= \frac{2}{\sqrt{14}} [2P(2) - P(1) - P(0)], \quad \text{and} \\ \rho_{40} &= \frac{2}{3\sqrt{14}} [P(2) - 4P(1) + 3P(0)]. \end{aligned} \tag{2.6}$$

For the case of 100% prolate alignment, where all of the substate population resides in the $m = \pm I$ states, the theoretical maximum values of the statistical tensors can be obtained from Eqn. 2.6 using $P(2) = 0.5$ and $P(1) = P(0) = 0$ to get $\rho_{20}^{max} = 0.5345$ and $\rho_{40}^{max} = 0.08909$. This is the type of alignment produced in intermediate-energy Coulomb excitation. The opposite situation occurs when the population mainly resides in $P(0)$, called oblate alignment; this type of alignment is produced in "head-on" Coulomb excitation such as the situation shown in Fig. 2.1. For 100% oblate alignment, $\rho_{20}^{max} = -0.2673$ and $\rho_{40}^{max} = +0.2673$. It is easy to see from Eqn. 2.6

that for no alignment (equal population of all substates), ρ_{20} and ρ_{40} vanish[3]. In that case, the angular distribution is isotropic in the frame of the emitting nucleus.

The γ-ray directional distribution coefficients are termed F_k, and depend on k, the initial spin I_i, the final spin I_f, and the multipolarity of the γ ray, through a function called the F-coefficient [58], defined as

$$F_k(L\,L'\,I_f\,I_i) = (-1)^{I_f+I_i+1}\hat{k}\hat{L}\hat{L'}\hat{I}_i \begin{pmatrix} L & L' & k \\ 1 & -1 & 0 \end{pmatrix} \begin{Bmatrix} L & L' & k \\ I_i & I_i & I_f \end{Bmatrix}, \qquad (2.7)$$

where L and L' are the multipolarities of the γ ray, the $\big(\dots\big)$ is a Wigner 3-j symbol and the $\big\{\dots\big\}$ is a 6-j symbol (see Ref. [60] and references therein). For a pure[4] multipole transition, *e.g.* a pure $E2$ transition, $L = L' = 2$. The F-coefficients can be calculated directly from Eqn. 2.7, and they are also tabulated in the literature (see *e.g.* Ref. [61]). For $2^+ \rightarrow 0^+$ transitions, $F_2 = -0.5976$ and $F_4 = -1.0690$.

The corrections to the a_k coefficients due to the finite solid angles subtended by the detectors, the Q_k coefficients, have been extensively studied only for cases where cylindrical γ-ray detectors are oriented with their symmetry axes pointing towards the target position [62, 63]. As will be discussed in Chapter 3, the γ-ray detectors in this work were not oriented in that way, but instead had their symmetry axes oriented tangentially to spheres centered at the target position. In the tangential geometry, neither tabulated values of Q_k nor analytical formulae known at present can be applied. An estimate of the solid-angle correction factors can be used in lieu of an analytical calculation, since the germanium detectors were not close-packed around the target position but were 24.5 cm away. The estimate is obtained by considering the detectors to be oriented with their symmetry axes pointing towards the target position, and performing a calculation in which the diameters of the detectors are equal to the crystal lengths in the true geometry, and the lengths in the calculation

[3]A useful definition of the % prolate alignment is $\rho_{20}/\rho_{20}^{max}$.

[4]For a γ ray of mixed multipolarity, e.g. an $E2+M1$, see Ref. [58].

are set equal to the diameters in the true geometry. The Q_k values that result from the calculation [64] are $Q_2 = 0.98$ and $Q_4 = 0.94$, which do not differ much from unity. A more accurate calculation probably requires Monte Carlo techniques, but is unnecessary since these Q_k coefficients are only small corrections to the angular distribution (on the order of 2%, since the $k = 4$ term is very small), and the statistical errors of the measurements are generally much larger.

2.1.2 Transient Field Strength

The mechanism of the transient field interaction is in principle understood, but at present there are no means to calculate transient field strengths reliably from first principles. In 1986, Rud and Dybdal made a thorough study [53] of a mechanism based on the polarization of electrons bound to the moving ions, that was originally proposed by Borchers *et al.* [50] as an explanation for their results that discovered the transient field. The polarized bound electron mechanism provides a coherent picture of the general behavior of the transient field, but Rud and Dybdal admitted that the ability to obtain quantitative predictions from the model for the purpose of making g-factor measurements was limited, as it remains today. Nevertheless, there are numerous properties of the transient field that are known empirically. The first property of the transient field that was apparent in early studies was that the direction is always parallel to the applied magnetic field, even if the static hyperfine field in that same substance is antiparallel. It was also observed that the transient field depends on the ion atomic number Z but not the mass number A, and it also depends on the species of ferromagnet (e.g., Fe or Gd), and the velocity at which the ion traverses the ferromagnet. By using very thin foils, experimenters were able to determine that the transient field interaction "turns on" within 10 fs of an ion entering the foil [65]. From studies using ion probes of different velocities, it was shown that the transient field is usually a smoothly-varying function of velocity, although for light ions ($Z = 8$, 9, 10) at low velocities, matching conditions permit atomic shell and molecular orbital effects

to cause discontinuities in an otherwise smooth velocity dependence [66]. For some heavy ions at low velocities, matching conditions for 4s electrons cause some field-strength discontinuity in Fe hosts [67], analogous to the 1s matching for the light ions. Outside of the very low velocity regime, for light ions ($Z \leq 20$), the field strength increases with ion velocity until reaching a maximum at a velocity of

$$v_K = Zv_0. \tag{2.8}$$

At much higher velocities, the TF magnitude approaches zero [68]. The quantity $v_0 = e^2/\hbar \simeq c/137$ is the Bohr velocity of atomic electrons, and Zv_0 is the velocity of the K-shell electrons of an atom of atomic number Z. It is assumed that the transient field arises from an interaction between the polarized electrons in the ferromagnetic host material with the ion as it traverses the material, and the velocity of maximum transient field strength for light ions indicates that the K-shell electrons of the ion play a significant role. In fact, the magnetic hyperfine interaction between a 1s electron and the nucleus is the largest among all electron-nuclear magnetic hyperfine interactions due to the high spatial overlap at the site of the nucleus. However, a theory to explain the interaction fails to describe the transient field strength over a large range of ion Z values and velocities. For heavier ions ($Z \geq 20$), the effectiveness of K-shell polarization has not been fully explored experimentally and the existing data suggest less efficient polarization of K-shell electrons.

In general, it is not always possible to perform simultaneous relative measurements between a reference g factor in a neighboring isotope to the nucleus of interest under identical experimental conditions, in order to calibrate the transient field strength. Therefore, different parametrizations have been established that are applicable to different velocity regimes and ion atomic numbers. Three parametrizations are found

in the literature, summarized in [52] as

$$\text{Linear parametrization [69]:} \quad B^{LIN} = aZ\frac{v}{v_0} \tag{2.9}$$

$$\text{Rutgers parametrization [70]:} \quad B^{RUT} = a'Z^{1.1}\left(\frac{v}{v_0}\right)^{0.45} M \tag{2.10}$$

$$\text{Chalk-River parametrization [71]:} \quad B^{CR} = a''Z\frac{v}{v_0}e^{-\beta v/v_0}. \tag{2.11}$$

The value M in the Rutgers parametrization is the magnetization of the host material, and sets of the parameters a, a', a'', and β exist for different mass regions and velocity ranges (typically between $1\,v_0$ and $5\,v_0$). The Rutgers and Chalk-River parametrizations have been extensively applied to the rare-earth region at typical velocities of less than $5\,v_0$. The linear parametrization is the most straightforward of the three parametrizations, but quickly diverges from measured TF strengths as the ion velocity deviates from the velocity and Z range in which the coefficient a was determined; an extrapolation to velocities beyond Zv_0 would grossly overestimate the magnitude of the transient field. The Chalk-River parametrization includes an exponential term that introduces a stronger velocity dependence, but even though it would show a disappearance of the transient field at a sufficiently-high velocity (dependent on the values of a'' and β), it was not intended to be applied outside of the velocity or Z range for which it was calibrated.

Because B_{TF} is a function of velocity, it is important to know the velocity of the ions as they travel through the ferromagnetic material. Ions lose energy while traversing matter, primarily by ionizing the material along their trajectories, which causes a continual decrease in velocity as they move through the material. The rate of energy loss, called the stopping power, can be expressed by the Bethe-Bloch equation [72],

$$-\frac{dE}{dx} = Kz^2\frac{Z}{A}\frac{1}{\beta^2}\left[\frac{1}{2}\ln\frac{2m_e c^2\beta^2\gamma^2 T_{max}}{I^2} - \beta^2 - \frac{\delta}{2}\right], \tag{2.12}$$

where z is the projectile atomic number, Z, A, and δ are the atomic number, mass

number, and density of the target material, β and γ are the projectile velocity and Lorentz factor, and m_e is the electron mass. I is the mean excitation energy which can be approximated as $(10 \cdot Z)$ eV for $Z > 16$ and T_{max} is the maximum energy that can be given to a free electron in a collision with a particle of mass M and velocity $\beta = v/c$,

$$T_{max} = \frac{2m_e c^2 \beta^2 \gamma^2}{1 + 2\gamma m_e/M + (m_e/M)^2}, \tag{2.13}$$

which can be approximated as $T_{max} \approx 2m_e c^2 \beta^2 \gamma^2$ for $2\gamma m_e/M \ll 1$. K is a constant equal to $4\pi N_A r_e^2 m_e c^2$, where N_A is Avogadro's number, and r_e is the classical radius of the electron, e^2/m_e. The Bethe-Bloch equation, and stopping powers in general, are an active area of research, with correction factors such as shell corrections of the target material usually taken into account [73]; for brevity, such details have been omitted here. In practice, heavy ion stopping calculations are usually done with computer programs based on the Bethe-Bloch equation or based on empirical stopping powers. It is important to appreciate the functional form of the stopping power, and its dependence on projectile atomic number and target material properties, to understand the principles of the transient-field targets presented in this Chapter.

Transient-field Target Principles

After the nuclear excited states are populated in an excitation target layer, the spin-aligned nuclei pass into a ferromagnetic target layer that provides the transient field. The ferromagnetic layer is polarized by an external magnetic field, which is usually provided by a small electromagnet designed to produce a magnetic field of 500-1500 Gauss (depending on the needs of the ferromagnetic layer used); the purpose of the applied magnetic field is to align the magnetic domains of the ferromagnet layer and bring it to its saturation magnetization. Although in principle any ferromagnetic material can be used to provide the transient field, two commonly-used ferromagnetic host materials are iron and gadolinium, which have the most extensively studied tran-

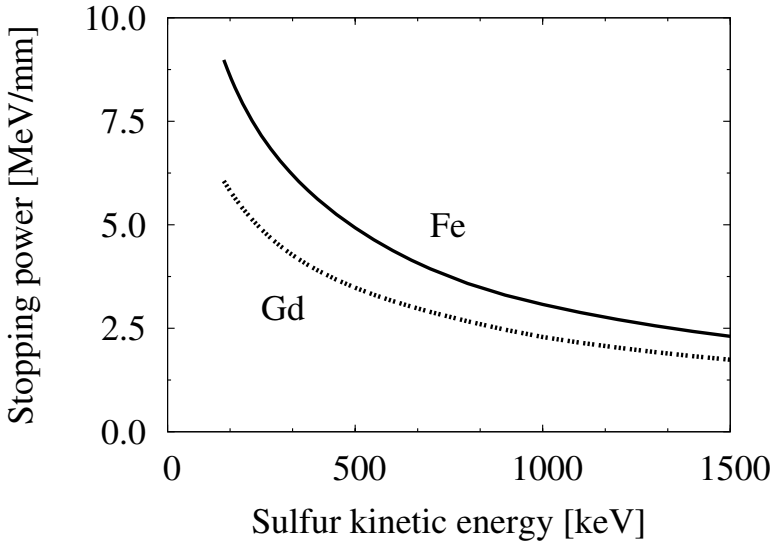

Figure 2.3: Ziegler stopping powers for sulfur projectiles in iron and gadolinium, as a function of energy.

sient field strengths. Iron is a good ferromagnet at room temperature, and has been well-studied. The use of Gd to provide the transient field is somewhat advantageous because ion ranges are longer in Gd than Fe, and thicker targets can be used so more time can be spent interacting with the transient field. The drawback is that Gd is not magnetic at room temperature and must be cooled to below its Curie temperature ($T_C = 293$ K) to enter the ferromagnetic phase, which requires a means to cool the target (such as liquid nitrogen). However, most recent stable-beam measurements have been made with Gd due to the advantage of its lower stopping power (compared to Fe, shown in Fig. 2.3), since the measurements are done with beam energies near the Coulomb barrier[5].

The conventional transient field target usually includes a "stopping layer," which consists of a thick, non-magnetic material that provides a perturbation-free environ-

[5]The energy of the electrostatic repulsion of the two positively-charged nuclei, when they are barely touching (the distance between their centers is the sum of their radii):

$$E_{\text{barrier}} = \frac{e^2 Z_1 Z_2}{R_1 + R_2} \approx \frac{1.44 \cdot Z_1 Z_2}{1.25(A_1^{1/3} + A_2^{1/3})} \text{ MeV}.$$

ment in which the nuclei can stop and then γ decay. The stopping layer ensures that the spin precession from the transient field layer is "locked in." The γ rays are emitted primarily while the nucleus is at rest, avoiding the complications arising from the Doppler shift.

Knowledge of the transient field strength is necessary to extract the magnitude of the g factor from a measured spin precession. The transient field is always parallel to the applied magnetic field direction, so the nuclear spins will precess in a direction determined by the sign of the g factor, independent of a precise calibration of the transient field strength. The precession direction is straightforward to measure if the general shape of the γ-ray angular distribution is known, because a simple increase or decrease of counts in a γ-ray detector at a known angle with respect to the beam axis will contain this information, as can be seen in Figure 2.1. Reversing the direction of the applied magnetic field will reverse the transient field direction, and therefore the direction that the angular distribution rotates as well. Comparing the counts in detectors for field up and field down is the main experimental signal that indicates both the sign and magnitude of the spin precession in a manner that cancels out most instrumental asymmetries.

2.1.3 Measurement of Spin Precession

The number of counts detected for a particular angle and magnetic field direction, e.g. up ($\uparrow$) is

$$N(\pm\theta\uparrow) = \zeta^{\pm} W(\theta\uparrow)\Delta t_{\uparrow}\overline{I_{beam}},$$

where the efficiency of the detector at the angle $\pm\theta$ is $\zeta^{\pm}$, the counting time during the particular field direction is $\Delta t_{\uparrow}$, and the average beam current during that time is $\overline{I_{beam}}$. The sign convention for the detector angle is shown in Fig. 4.10. The double

ratio ρ is used in order to eliminate instrumental asymmetries, as seen here:

$$\begin{aligned}\rho &= \sqrt{\frac{N(+\theta\uparrow)}{N(+\theta\downarrow)}\frac{N(-\theta\downarrow)}{N(-\theta\uparrow)}} = \sqrt{\frac{\zeta^{+}W(+\theta\uparrow)\Delta t_{\uparrow}\overline{I_{beam}}}{\zeta^{+}W(+\theta\downarrow)\Delta t_{\downarrow}\overline{I_{beam}}}\frac{\zeta^{-}W(-\theta\downarrow)\Delta t_{\downarrow}\overline{I_{beam}}}{\zeta^{-}W(-\theta\uparrow)\Delta t_{\uparrow}\overline{I_{beam}}}} \\ &= \sqrt{\frac{W(+\theta\uparrow)}{W(+\theta\downarrow)}\frac{W(-\theta\downarrow)}{W(-\theta\uparrow)}}.\end{aligned} \tag{2.14}$$

The detector efficiencies, up/down counting times, and average beam currents cancel, since the two ratios of the double ratio are each taken with respect to one detector. The precession effect is then

$$\epsilon = \frac{1-\rho}{1+\rho}, \tag{2.15}$$

which is related to the precession angle by

$$\Delta\theta = \frac{\epsilon}{S}, \quad \text{where} \quad S = \frac{1}{W(\theta)}\frac{dW(\theta)}{d\theta} \tag{2.16}$$

is the logarithmic slope of the angular distribution at the detector position.

The uncertainties in the quantities ρ and ϵ are

$$\delta\rho = \frac{\rho}{2}\sqrt{\sum_{i=1}^{4}\left(\frac{\delta N_i}{N_i}\right)^2}, \quad \text{and} \quad \delta\epsilon = \frac{2\delta\rho}{(1+\rho)^2}. \tag{2.17}$$

Assuming that the counts in the two detectors for each field direction are similar, such that there are N counts per detector per field direction, and using counting statistics where $\delta N \approx \sqrt{N}$, the uncertainty on the precession angle can be estimated. Inserting $\delta N = \sqrt{N}$ into $\delta\rho$ gives

$$\delta\rho = \frac{\rho}{2}\sqrt{4\left(\frac{\sqrt{N}}{N}\right)^2} = \frac{\rho}{\sqrt{N}}. \tag{2.18}$$

Using $\delta\rho = \rho/\sqrt{N}$, the uncertainty in the effect ϵ is

$$\delta\epsilon = \frac{2\delta\rho}{(1+\rho)^2} = \frac{1}{\sqrt{N}}\frac{2\rho}{(1+\rho)^2} \approx \frac{1}{2\sqrt{N}}, \tag{2.19}$$

where the last step is permitted since $\rho \approx 1$ for small precessions, which is the same as the initial assumption that assigns N counts to each detector per field direction. Since the precession angle is $\Delta\theta = \epsilon/S$, the uncertainty in the precession angle is

$$\delta_{\Delta\theta} \approx \frac{1}{2S\sqrt{N}}, \tag{2.20}$$

where the uncertainty in the slope factor S is generally considerably less than the statistical uncertainty in ϵ, and is neglected.

The inverse of $\delta_{\Delta\theta}$, S^2N, is often called the *precession sensitivity* of a particular pair of detectors located at an angle θ. In general, $S(\theta)$ is the dominant factor in determining where to place the detectors for a transient field experiment, in order to maximize S^2N.

2.2 $g(2^+)$ of Radionuclides: New Challenges

The transient field technique was developed at stable-beam facilities where measurements on most stable isotopes with picosecond 2^+ states were carried out. Several groups began modifying the technique in order to measure excited-state g factors in a limited number of radioactive nuclei. Since it is impractical to fabricate radioactive targets, especially when the nuclei are short-lived, the radioactive nuclei need to be produced as projectiles. In one method, the production of the radioactive nuclei was done with transfer reactions in the first layer of the transient-field target, and the principle challenges are the radioactive decay background from the nuclear reactions, the uncertainties the production mechanism introduces because of the unknown m-state populations, and possible feeding from higher-lying states, which lends an uncertainty

to the interaction time for the state of interest. Radioactive Ti isotopes were produced using α-transfer reactions on stable calcium beams, with ^{44}Ti ($T_{1/2} = 60$ yr) obtained using a ^{40}Ca beam [74] and ^{52}Ti ($T_{1/2} = 1.7$ m) obtained using a ^{48}Ca beam [75]. A similar method was used to obtain ^{68}Ge ($T_{1/2} = 271$ d) by α-transfer onto a stable ^{64}Zn beam [76]. Inspection of the nuclear chart shows this method has limited applicability to radioactive isotopes, because it requires a stable target with an isotopic chain that spans a few units more on the neutron-rich or neutron-deficient side than a neighboring isotopic chain (this is the case for the Ca isotopes and the Zn isotopes mentioned here). Some heavier neutron-deficient isotopes can be accessed as the line of stability begins to favor larger N/Z ratios, *e.g.*, ^{106}Cd$\rightarrow^{110}$Sn or ^{124}Xe$\rightarrow^{128}$Ba, and under suitable conditions other candidates may be found.

To measure g factors in radioactive isotopes available directly as beams, a technique based on Coulomb excitation in inverse kinematics can be used, which is one of the more recent transient field experimental arrangements that offers many advantages when the nucleus of interest is the projectile (for stable projectile applications, see *e.g.* Refs. [77, 78]). The inverse-kinematics arrangement is outlined in Fig. 2.4. Rather than using the beam to excite a target nucleus under study, a heavy ion of interest is accelerated and impinges on a thin target layer consisting of a light nuclear species such as silicon. In a head-on collision between a heavy projectile and a light target with the beam energy below the Coulomb barrier, the two nuclei will not touch. However, due to momentum conservation, the light nucleus will be knocked forward, followed by the heavy projectile. Since the light target ion is low-Z, it has a long range in the multilayer target and escapes the stopping layer, where it travels through vacuum to be detected in a particle detector subtending a small angular range about the beam axis. The heavy projectile, which may have been Coulomb-excited in the close head-on collision, traverses the ferromagnetic layer in an excited state, experiencing the transient field and precessing. Due to the higher stopping power for the higher-Z projectile, it stops in the stopping layer and emits a de-excitation γ ray which is

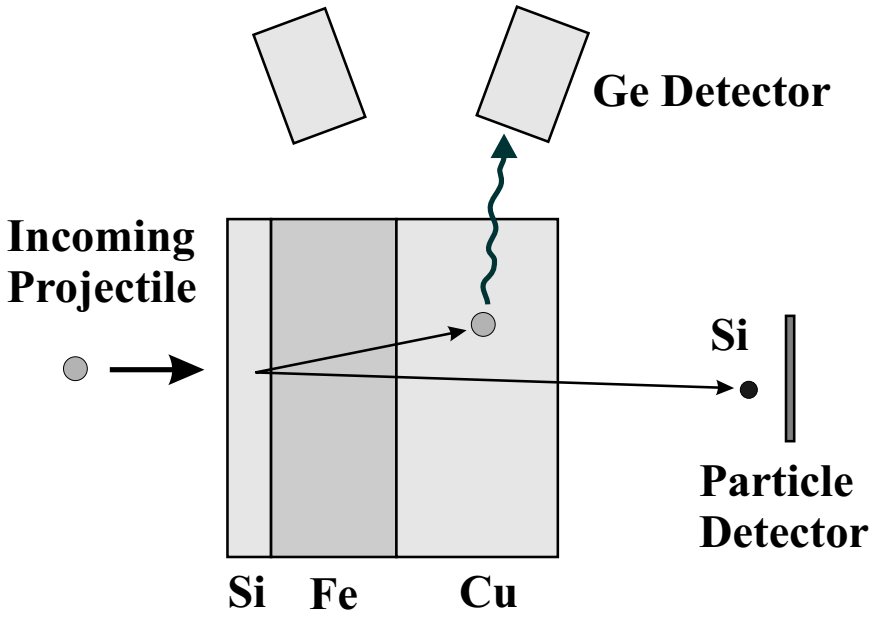

Figure 2.4: View of the conventional transient field target used in conjunction with Coulomb excitation in inverse kinematics. The incoming heavy projectile is excited in a head-on collision, sending the light target nucleus forward to be detected in the particle detector. The heavy projectile stops in the copper stopping layer, where it can emit a γ ray in a perturbation-free environment.

detected in coincidence with the light target ion that has recoiled out of the target. Such an arrangement produces a clean spectrum of γ rays from Coulomb excitation of the heavy projectile on the light target because of the particle coincidence required (i.e., if the Coulomb excitation occurs in the ferromagnet or stopping layer, no light particle will be detected in coincidence with the γ ray). This geometry, which selects head-on Coulomb excitation events, ensures that the excited nuclear states have a high degree of spin alignment with the magnetic substate population dominated by the $m = 0$ state.

A novel means of obtaining a radioactive ^{76}Kr ($T_{1/2}$ = 14.8 h) beam at the Berkeley 88" Cyclotron was developed [79], which used radiochemistry techniques to separate the long-lived sample produced in a stable cyclotron beam bombardment. The separated ^{76}Kr was then introduced into the ion source and accelerated for the experiment (the "re-cyclotron technique"). In this case, the inverse-kinematics Coulomb excitation technique was used, which overcame the drawbacks of using nuclear reac-

tions to populate the excited state. To solve the problem of the decay background, the stopping layer was replaced by a moving tape system that periodically removed the activity. In this way, it was shown that a transient field measurement is feasible on radioactive ions available with Coulomb-barrier kinetic energies, which are becoming available as re-accelerated beams at ISOL facilities such as ISAC-II [80], REX-ISOLDE [81], and HRIBF [82].

Whether the radioactive isotopes are produced by nuclear reactions in the target, or produced directly as a beam, the intensity (or yield) of radioactive isotopes is several orders of magnitude weaker than a stable beam intensity. The low intensity directly lowers the yield of γ rays, and hence increases the statistical uncertainty of the measurement. More will be said about the factors influencing the uncertainty later, since this dissertation involves the specific case of *fast* radioactive beams, which come with additional challenges that will be introduced in the following section.

2.3 $g(2^+)$ of Fast Radioactive Beams: New Technique

Most of the details of the first transient field measurements on radioactive isotopes were specially designed for the nucleus at hand, and something that they all held in common were the ion velocity ranges used. None of the radioactive $g(2^+)$ measurements were conducted with beam energies significantly different from previous studies using the same elements, and therefore the well-established parametrizations of the transient field strength with respect to velocity could be employed. To study radioactive isotopes produced using in-flight fragmentation, which offers access to numerous isotopes away from stability but with higher velocities not encountered in the previous transient field measurements, the new HVTF technique needed to be developed.

The HVTF technique consists of three key components: the production of a beam

of radionuclides with sufficient intensity (intensity requirements are addressed in § 2.3.3); intermediate-energy Coulomb excitation to produce spin alignment, using a thick target designed to degrade the projectile velocity to near Zv_0 (target design is addressed in § 2.3.3); and knowledge of the transient field strength, $B_{TF}(Z, v)$ which depends on the ion and ferromagnet combination and is a function of ion velocity that is usually described by a parametrization (the B_{TF} parametrization is addressed in § 2.3.2).

2.3.1 Intermediate–Energy Coulomb Excitation

When nuclei approach each other closely, they are each immersed in the strong electric field created by the protons of the other nucleus. Coulomb repulsion causes the nuclei to deviate from their original paths and follow hyperbolic paths called Rutherford trajectories. The shapes of the trajectories are hyperbolic because the electric field is a function of the distance separating the two nuclei, with a maximum at closest separation and nearly no effect at large distances (hence the arms of the hyperbola that asymptotically become straighter as the distance from the vertex increases). If the nuclei approach each other swiftly, they will experience a strongly-varying electric field as a function of time. This strong electric field is a time-dependent perturbation that can cause a nucleus to transition to an excited state in a process known as *Coulomb excitation*, often abbreviated as *Coulex.*

Semiclassical Approach

The strength and time-dependence of the electromagnetic perturbation is calculable because the interaction is the most well known of the fundamental interactions. The modified[6] Rutherford trajectory that governs the magnitude and time dependence of

[6]Since the scattering is inelastic and involves an energy transfer to the excited nucleus, the classical Rutherford orbit is slightly modified. Since one cannot specify where along the trajectory the excitation takes place, a symmetrization procedure is performed to account for this modification by setting up a new trajectory with the beam velocity changed to the average of the velocities before and after the collision. Fortunately, since most of the excited states studied by Coulomb excitation

the electric perturbation is usually treated classically. This is justified because the de Broglie wavelength of the heavy ion is small compared to the nuclear scattering length scale, or half the distance of closest approach in a head-on collision, a_0. The parameter a_0 is defined as

$$a_0 = \frac{Z_1 Z_2 \, e^2}{m_0 \beta^2}, \tag{2.21}$$

for a beam velocity $\beta = v/c$ and reduced mass m_0 of two nuclei with atomic numbers Z_1 and Z_2. The ratio $a_0/\lambda\!\!\!^{-}$ is called the Sommerfeld parameter η, written explicitly as

$$\eta = \frac{Z_1 Z_2 \, e^2}{\hbar c \beta}. \tag{2.22}$$

A classical description of the trajectory is justified when $\eta \gg 1$. The actual trajectory will determine the magnitude of the electromagnetic interaction, which can be decomposed into multipole interaction terms between the target's charge and the projectile's electromagnetic moments. These terms are called the "monopole–2^λ-pole" terms, such as the monopole-monopole term, which causes the Rutherford scattering. As was pointed out in §1.2, only certain electromagnetic moments exist in nuclei for symmetry reasons. Therefore, the monopole-dipole term is small since the nucleus has no static electric dipole moment, and the electric dipole strength that exists due to a dynamic electric dipole moment is concentrated at high energy in the Giant Dipole Resonance. The most important term is therefore the interaction of the target's electric field and the electric quadrupole moment of the projectile nucleus, which has the consequence that the majority of the Coulomb excitation strength causes E2 transitions. Magnetic interactions are suppressed by a factor of $(v/c)^2$ relative to electric interactions (which is not entirely negligible in the intermediate-energy regime; however, the electric quadrupole transitions will still dominate the Coulomb excitation).

For a nucleus subjected to the electromagnetic perturbation, the probability of

have only a few MeV of excitation energy, the energy transfer is small compared to the kinetic energy of the beam. Therefore, the effect of the trajectory modification is not important, especially with increasing beam energy.

Coulomb excitation will depend on the transition matrix element between the initial and final states, and this probability can be calculated quantum mechanically through perturbation theory. The total cross section for Coulomb excitation is calculated *semiclassically* to be

$$\frac{d\sigma_{coul}}{d\Omega} = \frac{d\sigma_{Ruth}}{d\Omega} \cdot P_{if}, \tag{2.23}$$

where P_{if} is the Coulomb excitation probability for a transition to be induced between two nuclear states by the electromagnetic perturbation of a particular Rutherford trajectory. Therefore, the measurement of the Coulomb excitation cross section yields information on nuclear matrix elements, which give insight into the nuclear structure of the initial and final nuclear states. To extract the matrix element contained in P_{if} from the measured excitation cross section, it is essential that the projectile and target nuclei remain well separated throughout the collision so that the interaction between them is purely electromagnetic. The usual way to ensure that the nuclei do not interact with the strong nuclear force — which can happen if any matter overlap occurs — is to choose the bombarding energy well below the Coulomb barrier. Specifically, a "safe Coulex" energy can be defined such that the distance of closest approach between the nuclear centers is the sum of the nuclear radii plus a few extra fm, where the choice of how many additional fm of separation is left to the experimenter's tolerance of possible nuclear effects [83].

Coulomb excitation will generally occur only under the condition that the collision is faster than the time it takes for the nucleus to adjust to the changing electric field. This is called the *adiabatic condition,* and is usually expressed quantitatively as the ratio between the collision time $t_{coll} \approx a_0/v$ and the transition time $t_{trans} = \hbar/\Delta E$ (with $\Delta E = E_f - E_i$),

$$\xi = \frac{a_0 \Delta E}{\hbar c \beta}. \tag{2.24}$$

The condition for which Coulomb excitation is probable is $\xi < 1$, and if the bombarding energy is too low or the excitation energy is too high such that $\xi \geq 1$, the Coulex

probability drops exponentially with ξ [84]. For typical Coulomb excitation experiments, which run near Coulomb barrier energies, the adiabatic condition limits the excitation to states with only a few MeV excitation energy. At such energies, a high-Z nucleus can cause multiple Coulomb excitations of a nucleus under study, especially if that nucleus is highly deformed, because of the ease of inducing E2 transitions in a nucleus with a large quadrupole moment. In such a situation, it is no longer a weak perturbative scenario and a system of coupled-channels equations needs to be solved to extract the many transition matrix elements involved [85].

When the beam energy is raised into the intermediate-energy range, several additional effects come into play. The primary effect is the rapid increase in the eccentricity of the Rutherford orbits, which begin to look like straight lines, since the Coulomb repulsion can cause less deviation of the high-momentum trajectory. The beam energy is above the Coulomb barrier, so the distance of closest approach can be smaller than the sums of the nuclear radii, and the projectile and target can interpenetrate. Nuclear reactions can then take place, including few-nucleon removal and fragmentation reactions, which are undesirable because they result in nuclear species changes rather than inelastic scattering. The experiment can be designed such that only particles that are deflected within a small angle θ_{max} (corresponding to a large enough minimum impact parameter b_{min}) are detected. A secondary effect at high beam energies is the Lorentz transformation of the electric fields of the projectile and target, as seen in Fig. 2.5, which increases the concentration of electric field strength in the plane perpendicular to the beam axis. This means that the projectile and target do not "feel" the influence of each other until they are closer than in the conventional Coulomb excitation situation. Half the distance of closest approach, a_0, is modified by the Lorentz factor $\gamma = 1/\sqrt{1-\beta^2}$ to become $a = a_0/\gamma$, which reflects the reduced effect of the electric fields prior to the scattering. The scattering angle in the center

of mass system, θ_{cm}, can be described classically by the relation

$$b = \frac{a_0}{\gamma} \cot \tfrac{1}{2}\theta_{cm}, \tag{2.25}$$

where b is the impact parameter, shown in Fig. 2.5. The collision time is very short, of order $b/\gamma v$, and during that time there is an increased electric field strength due to the Lorentz concentration of the electric fields of the projectile and target. Multiple Coulomb excitation can no longer occur, since the reaction is much more "sudden." The one-step excitation dominates, and can be solved using perturbation theory. The adiabatic condition from Eqn. 2.24 is now

$$\xi = \frac{a_0 \Delta E}{\gamma \hbar c \beta} \longrightarrow \frac{\Delta E}{\hbar c} \frac{b}{\gamma \beta}, \tag{2.26}$$

where the distance of closest approach in a head-on collision is replaced by the appropriate separation distance for small-angle scattering, the impact parameter b. From Eqn. 2.26, one can see that fast collisions with $b \sim R_1 + R_2$ (the sum of the nuclear radii) can populate states of order 10 MeV excitation energy.

As was mentioned previously, intermediate-energy beams can easily cause nuclear reactions for impact parameters small enough to allow the nuclei to overlap. In contrast to a Coulomb excitation cross-section measurement, a HVTF experiment does not need to strictly ensure "safe Coulex" because the goal is not to extract electromagnetic transition matrix elements. Therefore, the exact separation to allow between the projectile and target (which is not a well-established quantity) is not a major concern. It suffices to choose a maximum scattering angle θ_{max} such that the impact parameter b is larger than the sum of the nuclear radii, where if nuclear effects set in, they should affect the excitation cross section without impacting the distribution of $P(m)$ too severely. Since Eqn. 2.25 is defined for scattering angles in the center of mass frame, θ_{cm}^{max} must be transformed into the appropriate lab-frame θ. The relativistic formulae for this transformation are given here, and can also be

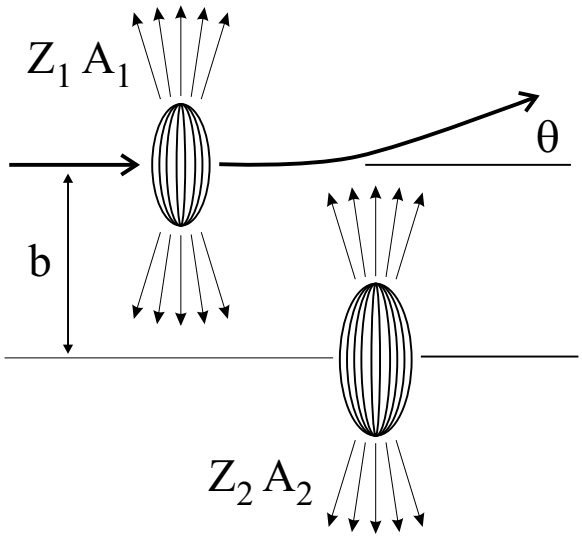

Figure 2.5: The electric field lines from the projectile and target nuclei are contracted along the beam axis by Lorentz effects for intermediate-energy beams. The projectile has Z_1 protons and mass A_1, and the target has Z_2 protons and mass A_2. The impact parameter b is the distance separating the lines of initial trajectories, and the projectile scattering angle is θ.

found in standard texts [86]. For a projectile with mass number A and kinetic energy T, the Lorentz factor γ is

$$\gamma = 1 + \frac{T}{Am_N\,c^2}, \tag{2.27}$$

with $m_N c^2 = 931.494$ MeV. Using the ratio of the projectile mass to the target mass, $\rho = M_p/M_t$, the Lorentz factors for the projectile and target can be defined for the center of mass frame,

$$\gamma_1 = \frac{\gamma + \rho}{(1 + 2\rho\gamma + \rho^2)^{1/2}} \tag{2.28}$$

and

$$\gamma_2 = \frac{1 + \gamma\rho}{(1 + 2\rho\gamma + \rho^2)^{1/2}}. \tag{2.29}$$

Eqns. 2.28 and 2.29 can be used in the expression for the lab frame scattering angle θ_{Lab} that corresponds to the center of mass scattering angle θ_{cm}:

$$\tan\theta_{Lab} = \frac{1}{\gamma_2} \cdot \frac{\sin\theta_{cm}}{(\cos\theta_{cm} + M_p\gamma_1/M_t\gamma_2)}. \tag{2.30}$$

2.3.2 Transient Field Strength at High Velocity

Few studies have been undertaken to study the action of the transient field at velocities $v > Zv_0$ for ions with $Z \leq 16$, although a great number of experiments have been conducted at ion velocities between the L and K shell electron velocities ($\frac{1}{2}Zv_0 < v < Zv_0$). Measurements of spin precessions using stable beams with v at Zv_0 have been achieved for example using sulfur projectiles [87] at the Max-Planck-Institut für Kernphysik in Heidelberg, and a higher-Z Cr beam ($Z = 24$) at 752 MeV, corresponding to $v = 21v_0$ was produced with the UNILAC accelerator at Darmstadt [88], lending hope to the idea that high velocity measurements are possible. However, radioactive beams produced by fragmentation have velocities on the order of 0.3-0.5 c, and the K-shell electron velocity is $Zv_0 \approx \frac{Z}{137}c$, which is much less than 0.3 c (especially for ions with $Z = 16$ in this work). There is no *a priori* reason why any of the conventional TF parametrizations could be extended into this velocity regime; indeed, it would seem that no TF interaction is possible at such high velocities. Nevertheless, there has been great interest in the use of fast radioactive beams for transient field g factor measurements, and several groups have reported their approaches to the problem [89, 90]. The primary concern is that there would be a sufficient precession effect to make a HVTF technique feasible for radioactive beams, which often are only available with low intensity.

A parametrization of the transient field strength is needed in order to extract g factors from possible spin precessions. The parametrization can then be used together with the other experimental details such as the intermediate-energy Coulomb excitation cross section and the degree of spin alignment, the angular distribution slope parameters at the detector locations, and the γ-ray detector efficiencies to estimate the experimental sensitivity to the spin precession expected in the high velocity regime.

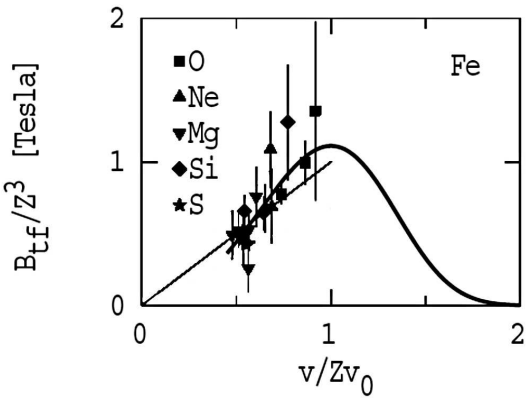

Figure 2.6: TF strengths for light ions in Fe (data points) and high velocity TF parametrization that results from a fit using the functional form described in the text (solid line), from Ref. [91]. Also shown is a linear parametrization used in this mass and velocity range.

Parametrization for High Velocity Light Ions

A parametrization was proposed by Stuchbery [91] after an examination of the available data for transient field strengths for ions with $6 \leq Z \leq 16$, traversing Fe or Gd foils, at velocities greater than $\frac{1}{2}Zv_0$. A brief description of this parametrization, which was used to plan the experiment on ^{38,40}S and analyze the resulting data, will be given here. In principle, since high-velocity light ions will exist primarily in high charge states (*e.g.*, $q = Z - 1$) while traversing matter, the physical situation is simplified relative to heavier ions, and it is plausible that a model-based parametrization can be found to describe the transient field behavior. The basic physical principle for the model-based parametrization, here called the ANU parametrization, is that the transient field strength for a particular ion as a function of velocity should follow the hydrogen-like charge-state distribution for that ion as a function of velocity, except that the peak of the field strength should occur at $v = Zv_0$. This is a reasonable assumption because it is well-established that the K-shell electrons are responsible for the majority of the transient field effect for light ions [53]. The magnetic field at

the site of the nucleus, due to a $1s$ electron in particular [92], is

$$B_{1s} = 16.7 Z^3 R(Z)\, T, \tag{2.31}$$

where the relativistic correction factor, $R(Z) \simeq [1 + (Z/84)^{2.5}]$, is not appreciably different from 1 for light ions. This expression is often used as a starting point in describing transient field strengths, which are generally described as [51, 52, 53]

$$B_{tf} \propto \xi_{1s}(v, Z) F^1_{1s}(v, Z_1, Z_2) B_{1s}(Z). \tag{2.32}$$

In the above expression, ξ_{1s} is the polarization of the $1s$ electron carried by the ion and F^1_{1s} is the fraction of ions that are carrying one $1s$ electron (this is also called the "single K-vacancy fraction"). For the development of the parametrization, Stuchbery used the observation that ξ_{1s} is virtually velocity-independent and wrote the polarization factor ξ_{1s} as $\xi_{1s}(Z) = A_\xi Z^{P_\xi}$, where A_ξ and P_ξ are parameters that can be different for each ferromagnetic host material. The K-vacancy fraction F^1_{1s} was used to describe the velocity-dependence of the transient field, using a function that reproduced the behavior of the hydrogen-like charge state fractions for light ions traversing Fe and Gd foils, calculated with the program LISE [93, 94]. The adopted function has the form $f(x) = axe^{-bx^2}$, where $x = E/A$ is the kinetic energy per nucleon. Using this functional form together with the Z-dependent form for the polarization parameter and B_{1s}, the ANU parametrization is

$$B_{tr}(v, Z) = A Z^P (v/Zv_0)^2 e^{-\frac{1}{2}(v/Zv_0)^4}, \tag{2.33}$$

with the parameters A and P determined for Fe and Gd hosts by fitting the available data on transient field strengths. For Fe hosts, summarized in Fig. 2.6, the value of $A = 1.82(5)$ T with $P = 3$ was obtained [91].

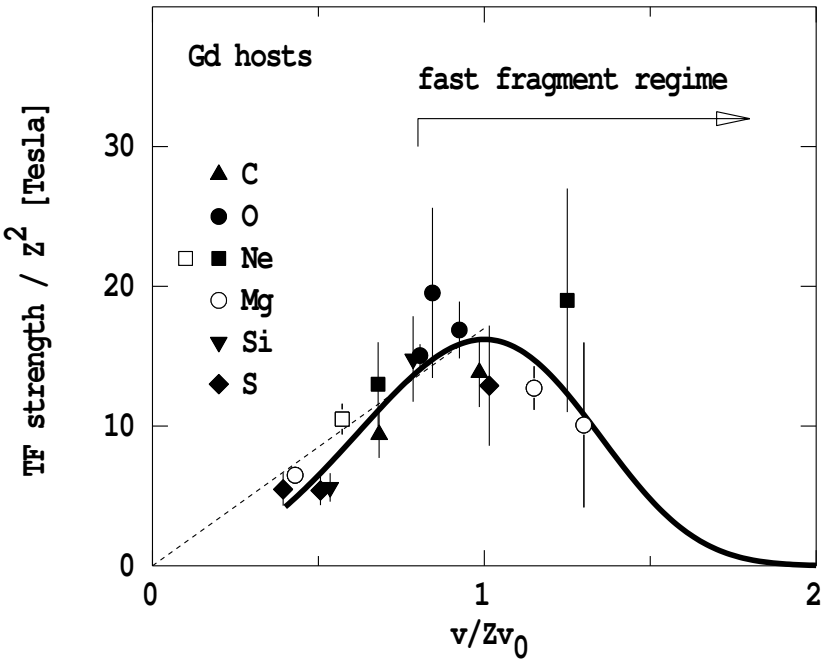

Figure 2.7: Compilation of previously-known TF strengths for light ions in Gd (solid symbols) and high velocity TF parametrization (solid line), and newer measurements that test the parametrization (open symbols), from Ref. [95]. A linear parametrization (dashed line) is also shown.

Stable Beam Transient Field Strength Measurement

When the light-ion HVTF parametrization was proposed, it was apparent that very few data on transient field strengths beyond $v = Zv_0$ exist, and that more experimental work was necessary to validate the parametrization. An experiment was performed at the 14UD Pelletron facility at The Australian National University as a collaboration between researchers at the NSCL and at ANU, to measure transient field strengths for Mg ions in Gd, at velocities above Zv_0 [95]. Gadolinium was chosen as the ferromagnet because there are fewer "high-velocity" field strength measurements reported in the literature (where high velocity means $v > \frac{1}{2}Zv_0$) for gadolinium compared to iron. In addition, a $v = 1.25Zv_0$ measurement (the highest velocity with which a TF measurement has been made for ions with $6 \leq Z \leq 16$) has been reported for neon in Gd, with large error bars. In Figs. 2.6 and 2.7, the previously-known TF strengths are shown as filled points, and the $v > Zv_0$ Ne point leaves open to questioning whether

the transient-field strength is increasing or decreasing at $v = 1.25Zv_0$. A confirmation of the proposed parametrization in gadolinium would provide strong evidence for the validity of the proposed iron parametrization, which was based on a fit to more data points than gadolinium. In order to ensure the validity of the result, a low-velocity point for Mg in Gd was measured in the region where the transient field has been well characterized, $v \sim \frac{1}{2}Zv_0$, and the transient field strength extracted from that measurement agreed with systematics of known transient field strengths. The new ANU measurements are shown in Fig. 2.7 as open points. The new measurements consist of two high-velocity and one low-velocity Mg TF strength measurements, along with an additional point taken with a Ne probe near $\frac{1}{2}Zv_0$ [95]. The previously-measured transient field strengths (filled points) and the ANU parametrization [91] (solid line) are shown for comparison. Good agreement is seen between the new high velocity data and the parametrization for Gd hosts, and since the transient field behavior is Fe is similar, the Fe parametrization should also hold. Further experiments are planned to measure high velocity transient field strengths in Fe at ANU for additional confirmation.

2.3.3 Target Design for Optimum Slowing

The concentration of transient field strength near Zv_0 provides a stringent constraint on the experiment design. Slowing the fast radioactive projectiles to near Coulomb-barrier velocities is the most critical aspect to be addressed in the choice of the experimental parameters, *i.e.* primary beam energy, primary target thickness, wedge degrader thickness, and HVTF target layer thicknesses, because without a proper slowing of the projectiles, there is no transient-field induced spin precession. Accomplishing this slowing in an optimum fashion involves several compromises to ensure a successful experiment. Some aspects of the compromises that affect the experimental sensitivity to spin precession can be quantified by figure of merit expressions involving the number of γ-ray counts and the slope of the γ-ray angular distribution at

the γ-ray detector positions, as discussed in § 2.1.3. To first order, however, these quantities only impact the amount of beam time required to achieve a statistically significant result. Of greater importance is the necessity to slow the beam down into the velocity range where B_{TF} can act at all.

The requirement that the projectiles be slowed to $v \approx Zv_0$ (which corresponds to $\sim$5 MeV/nucleon for the heavy sulfur isotopes) is nearly the equivalent to requiring the ions to slow as much as possible without stopping in the HVTF target. Slowing ions in matter necessarily increases the energy spread of the projectiles. A compromise must therefore be made between how much slowing can be done in the fragment separator (and the fragment transmission that lowers as the momentum spread of the beam increases) and the amount of slowing that gets left for the HVTF target itself. The practical limit $\langle E_{out} \rangle - \sigma_E > 0$ should be obeyed, where σ_E is the full width at half maximum of the energy distribution for the emerging ions. An estimate of the increase in energy straggling is given by Gottschalk, where for an incoming energy spread σ_i, the outgoing energy spread is approximately [96]

$$\sigma_o = \frac{S(E_{out})}{S(E_{in})} \cdot \sigma_i, \tag{2.34}$$

where $S(E) = -dE/dx$ is the energy-dependent stopping power for the ion/material combination of interest. Using Eqn. 2.34 and an incoming energy spread, the compromise between slowing in the separator and slowing in the HVTF target can be quantified. In general, a simulation of the fragment separator and ion optics is necessary to calculate beam properties after production, separation and transport.

An additional constraint on the experiment design is the *slowing down time.* In the HVTF target, the slowing must be done quickly because after the Coulomb excitation event, the states begin decaying. Decays that occur in the non-ferromagnetic layer accomplish nothing because there is no transient field present. However, since the cross section for Coulomb excitation goes as Z^2_{target}, it is advantageous to use a thick,

high-Z Coulomb excitation layer to ensure enough excitation yield. The thickness of the Coulex layer increases the transit time of the ions prior to their arrival in the ferromagnet, so a compromise needs to be made between excitation yield and the need to ensure a large interaction time with B_{TF} prior to the decay governed by the excited-state lifetime τ. It turns out that iron has a higher stopping power than many common Coulex targets such as gold, so if iron is used, it is beneficial to place the transition to the ferromagnetic layer at a point where the ion velocity is still beyond $2Zv_0$; there is no transient field initially, but the ions are quickly slowed into the velocity range where B_{TF} is large. To determine whether a particular nuclear excited-state g factor can be measured using the HVTF method, the slowing time needs to be compared to the excited-state lifetime.

The slowing time can be estimated using tabulated ranges of ions in matter, available, for instance, with the program SRIM [97]. As a benchmark, the time it takes for ions with $6 \leq Z \leq 20$ to slow in a single step from 100 MeV/nucleon down to 5 MeV/nucleon in aluminum (a typical degrader material), is shown in the left panel of Fig. 2.8. These values were calculated for each proton number Z (for simplicity using each isotope's stable mass value) by looking up the ranges in Al for 100 MeV/nucleon, $R_Z(100)$, and subtracting the range of the ion with 5 MeV/nucleon, $R_Z(5)$, to get the total slowing distance, $R_Z(\Delta E) = R_Z(100) - R_Z(5)$. To obtain the slowing down time, the energy loss was approximated linearly through the target and the velocity was approximated as $v(x) = \sqrt{2E(x)/M}$. The inverse velocity as a function of energy was integrated through the distance $R_Z(\Delta E)$. As a comparison to this "one step" slowing, the times were calculated for an iron transient-field layer, assuming that the ions have first been slowed by some means to 20 MeV/nucleon prior to the iron layer. The right side of Fig. 2.8 shows the resulting times for ions to slow from 20 to 5 MeV/nucleon in iron, using range tables for ions from carbon to calcium and the linear energy loss approximation. It can be seen that the times range from ∼2-5 ps, meaning that excited states with lifetimes on the order of a few ps

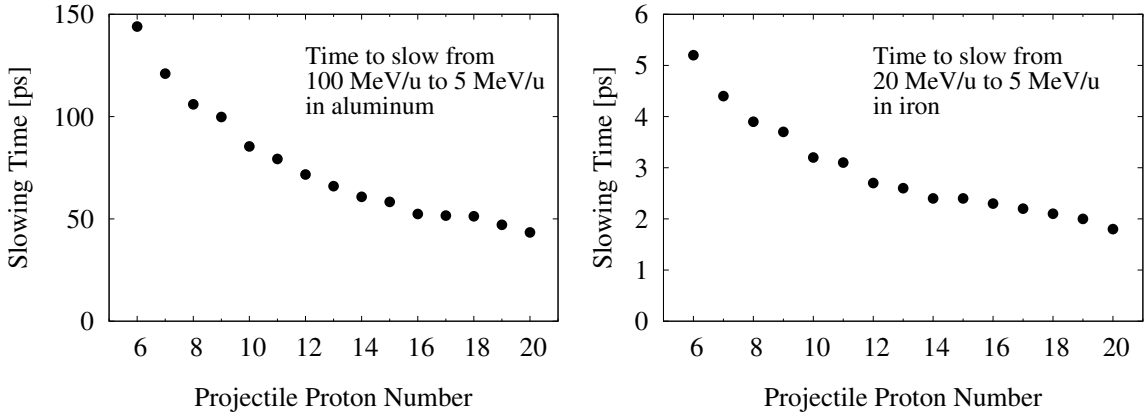

Figure 2.8: Approximate time for ions with $6 \leq Z \leq 20$ to slow down to 5 MeV/nucleon, in one step from 100 MeV/nucleon in Al (left) and as a second step from 20 MeV/nucleon in Fe (right); see text for calculation details. Note the change in vertical scale between the two scenarios.

are accessible, if the transit time in the Coulomb excitation layer is also kept to a few ps. Since the slowing from 100 MeV/nucleon — the typical production energy — has been shown to be much greater than tens of picoseconds, it is clear that the Coulomb excitation layer cannot be responsible for slowing the ions from 100 to 20 MeV/nucleon, and the bulk of the slowing must be done first in the separator.

Therefore, the general technique of transient field measurements on fast beams is a "three-step slowing" process, where the ions are slowed using degraders in the fragment separator, and then slowed in a two layer HVTF target, where a high-Z Coulex layer slows the ions while populating the excited states, and then the transient field layer slows the ions to near or below Zv_0. It has been shown that an iron transient-field layer can accomplish slowing from 20 MeV/nucleon to 5 MeV/nucleon in 2-5 ps and is therefore a better choice than gadolinium, which has a lower stopping power and therefore a longer stopping time. It is possible, however, to use a single-layer HVTF target where gadolinium ($Z = 64$) serves as both a Coulex target and the ferromagnetic host. This choice may have a smaller effective time between the average excitation and the onset of B_{TF} under certain experimental conditions, but it is a compromise between transient field interaction time and the Coulomb excitation cross

section, in addition to the added complexity of requiring a cooling mechanism for the gadolinium.

The beam intensity requirements for the fast-beam transient field method depend on the Coulex yield, integrated B_{TF}, state lifetime τ, γ-ray detection efficiency and angular distribution, and detector positions. Intermediate-energy Coulomb excitation cross sections are usually of order tens of millibarns (depending on the B(E2) value, target Z, beam energy, and maximum scattering angle θ_{max}), and thick targets of order hundreds of mg/cm^2 can be used. The γ rays are emitted with a probability that decays exponentially in time after excitation, meaning that a certain fraction will be emitted prior to reaching the ferromagnet (or prior to the projectile velocity being near Zv_0 where B_{TF} has any effect). The usual figure of merit to maximize in conventional TF experiment planning is S^2N, but a different figure of merit should be used for fast beams due to some different conditions. Due to the long stopping time for fast beams, the only γ rays that contribute to the number N are those that are Doppler corrected properly into a peak area that can be accurately obtained. For practical reasons that will be explained in Chapter 4, those γ rays are emitted after the projectiles leave the target and are flying with constant velocities. Therefore, the number N needs to be reduced by a factor that depends on the excited state lifetime, τ, and the transit time through the target, T: $N \rightarrow Ne^{-T/\tau}$. The figure of merit that can be used to determine the required beam intensity is therefore

$$S^2\phi^2 W\sigma e^{-T/\tau}, \tag{2.35}$$

with $\phi = \Delta\theta/g$ representing the g-factor dependent term (a larger g factor requires less time to measure), S is the slope and W is the angular distribution at a particular detector angle, and σ is the excitation cross section.

Chapter 3

Application at NSCL

The radioactive ^{38,40}S isotopes under study were produced using in-flight fragmentation at the NSCL's Coupled Cyclotron Facility. The high kinetic energy of the resulting fragments created challenges to the $g(2^+)$ measurement that needed to be overcome as described in Chapter 2. The experimental technique and equipment used to accomplish the $g(2^+)$ measurement for ^{38,40}S at the NSCL are described in this Chapter.

3.1 Isotope Production

Two different stable isotopes were accelerated as primary beams to produce the desired radioactive sulfur isotopes. To produce ^{38}S, enriched ^{40}Ar gas was introduced into a superconducting Electron Cyclotron Resonance (ECR) ion source, leading to $^{40}Ar^{7+}$ ions that were guided into the K500 superconducting cyclotron and accelerated to 12 MeV/nucleon. The accelerated $^{40}Ar^{7+}$ ions were sent through the coupling line and radially injected near the center of the K1200 cyclotron, where a thin carbon foil stripped them of their remaining electrons. The K1200 was then used to accelerate the $^{40}Ar^{18+}$ ions to 140 MeV/nucleon, at which energy they were extracted and directed onto a thin target of beryllium located close to the exit of the K1200 cyclotron.

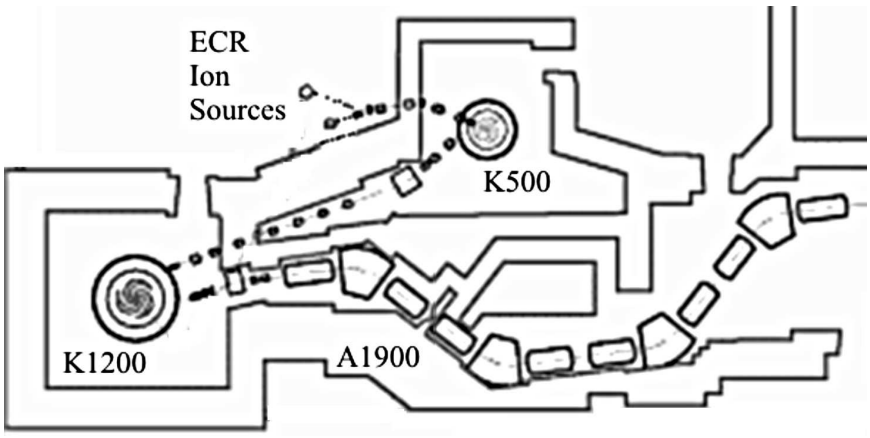

Figure 3.1: Schematic of the coupled cyclotrons and A1900 fragment separator.

Fragmentation reactions occurred inside the target, creating a wide range of nuclides lighter than ^{40}Ar, by removing several nucleons and leaving the products flying forward with a similar velocity to that of the incoming primary beam. For instance, ^{38}S was created through the removal of two protons from the ^{40}Ar projectiles.

The fragment separator, called the A1900 [98], was necessary to separate the desired fragment from among the variety of products. The A1900 consists of a symmetric arrangement of four superconducting dipole magnets, and several superconducting quadrupole triplet magnets, and has a large acceptance and high resolving power. The target box after the K1200 cyclotron is located at the object position of the A1900, which works by separating the reaction products according to their momentum to charge ratios. A diagram of the A1900 is shown in Fig. 3.1, taken from Ref. [98]. At the second intermediate image, there is a large dispersion of the fragments in the horizontal direction. At this position a wedge-shaped degrader and a slit system can be used to selectively enhance the transmission of the species of interest. The second half of the A1900 then focuses the fragments back for transmission to the experimental areas.

The ^{40}S ions could not be created by removing nucleons from ^{40}Ar, so in a separate run, a primary beam of ^{48}Ca was created by heating a sample of enriched ^{48}Ca oxide material to $\sim$875° C in an oven connected to the ECR ion source. The ^{48}Ca vapor

Table 3.1: Production and properties of the radioactive beams.

Primary beam		^{9}Be Target	A1900 Settings		Secondary beam			
Ion	Intensity (pnA)	Thickness (mg/cm^2)	$B\rho_{1,2}$ (Tm)	$B\rho_{3,4}$ (Tm)	Ion	E (MeV)	Intensity (pps)	Purity (%)
^{40}Ar	25	987	3.5303	2.2050	^{38}S	1547.5	$2 \cdot 10^5$	> 99
^{48}Ca	15	1034	3.6580	2.2872	^{40}S	1582.5	$2 \cdot 10^4$	> 95

was ionized, and the ions in the 8+ charge state were accelerated through the coupled K500-K1200 system to 140 MeV/nucleon, and the resulting fully-stripped ^{48}Ca ions impinged on a Be target. The production of ^{40}S occurred through the removal of four protons and four neutrons from ^{48}Ca.

The primary target thicknesses and A1900 magnetic rigidities are summarized in Table 3.1. An acrylic plexiglass wedge degrader, 971 mg/cm^2 thick, as well as a 0.5% momentum slit, were employed in the second intermediate image position. The resulting kinetic energies of the ^{38,40}S fragments were approximately 40 MeV/nucleon, which was found to be the minimum energy to which the secondary beams could be slowed before the transmission through the beamlines would suffer due to energy straggling in the slowing down process. The HVTF target was therefore specifically designed for ^{38,40}S ions of energy $\sim$40 MeV/nucleon.

3.2 Multilayer Target

Using stopping powers of Ziegler and the fragment separator simulator LISE [93, 94], a multilayer target was designed to perform the HVTF measurement on the ^{38,40}S isotopes. The target materials and thicknesses needed to be chosen carefully to ensure a successful measurement, as described in § 2.3.3. The program LISE was used to estimate the secondary beam energy for ^{38}S fragments produced by the fragmentation of 140 MeV/nuclear ^{40}Ar on a ^{9}Be target. A pure beam was desirable for the first HVTF measurement to minimize unwanted background, but in general it is not a

stringent requirement. In the case of the ^{9}Be(^{40}Ar,^{38}S)X fragmentation reaction it was possible to set the A1900 fragment separator settings to obtain a $> 99\%$ pure ^{38}S secondary beam with an energy of $\sim$40 MeV/nucleon. Using this beam energy as a starting point, it remained to design an HVTF target, assemble the target by rolling the target layers to the desired thicknesses, and then to confirm the expected energy loss by testing it in-beam prior to the g-factor measurement. The goal was to choose a target that would slow the projectiles down to as low of a velocity as possible without stopping, or around 100-200 MeV.

The Coulomb excitation target layer was chosen to be gold due to its high atomic number, $Z = 79$. Since Au is monoisotopic in stable form, there will be less target γ rays from different levels in the target nuclei Coulomb excited by the beam. The malleable nature of Au is also beneficial, and allows it to be easily rolled to the proper thickness. For the transient field layer, iron was chosen as the ferromagnet since it does not require cooling with liquid nitrogen or other means, and as was shown in Chapter 2, it has a high stopping power, which is important to ensure that the projectiles slow as quickly as possible. Natural iron has 4 isotopes, ^{54,56,57,58}Fe, and the most abundant isotope, ^{56}Fe, has a γ-ray transition at 846 keV, which is near the 903 keV first-excited state energy in ^{40}S.

3.2.1 Stopping Powers and In–Beam Test

The Au and Fe thicknesses were chosen based on calculations with the program TRIM, which uses the stopping powers of Ziegler and coworkers [99]. The Au thickness was chosen to be 355 mg/cm^2, which was calculated to slow the sulfur ions to kinetic energies of $\sim$780 MeV. For a comparison, calculations using the ATIMA [100] stopping powers implemented in the program LISE predicted a kinetic energy of $\sim$810 MeV when Lindhard-Sorensen (LS) corrections [101] were included, and $\sim$780 MeV without LS corrections. The optimum Fe thickness was determined to be in the range 100-110 mg/cm^2 as a result, for which predictions of final energies of 130, 216, and

131 MeV were obtained using stopping powers of Ziegler, ATIMA+LS, and ATIMA, respectively, for 110 mg/cm^2 Fe.

The two foils were purchased from Goodfellow Cambridge Limited, a 25 mm x 25 mm Au foil with a nominal thickness of 0.250 mm and purity 99.995%, and a 50 mm x 50 mm Fe foil of nominal thickness 0.125 mm and purity 99.999%. The Au foil was rolled to 355 mg/cm^2 using the metal roller in the NSCL detector lab, by sandwiching the Au foil between clean strips of stainless steel (by folding one strip in half). The sandwich of steel and Au was passed through the roller several times, reversing the orientation of the sandwich each time in order to reduce any systematic thickness variation across the Au. The Fe foil was cut into 4 squares of $\sim$25 mm^2, and three of the pieces were rolled to thicknesses of 90, 100, and 110 mg/cm^2.

It was essential to test the two-layer target in-beam to choose the optimum Au/Fe target combination, for two reasons. The stopping powers are not known to high accuracy for the slowing down of ^{38}S from $\sim$1500 MeV to $\sim$150 MeV, as shown above. In addition, the exact initial beam energy would be unknown prior to the actual beam extraction from the cyclotrons. For the target test, a primary beam of ^{40}Ar was accelerated to 140 MeV/nucleon and impinged upon a 945 mg/cm^2 Be production target. An acrylic wedge degrader of thickness 971 mg/cm^2 was used at the dispersive image of the A1900 to separate the desired ions from other species produced in the fragmentation reaction. The secondary beam of ^{38}S was transmitted through the second half of the A1900, with the magnets set to a magnetic rigidity of $B\rho_2 = 2.2053$ Tm, corresponding to a kinetic energy of 1548 MeV. The Au target was held on a rotating target ladder in order to change the effective thickness according to $t' = t/\cos\theta$, where the normal target thickness is t and the thickness along the beam axis is t'.

Two particle detectors were used, a silicon PIN diode of 980 μm thickness (for measuring the after-target energy of the ^{38}S ions) and a plastic scintillator phoswich detector (for identification of possible fragmentation products in the thick target),

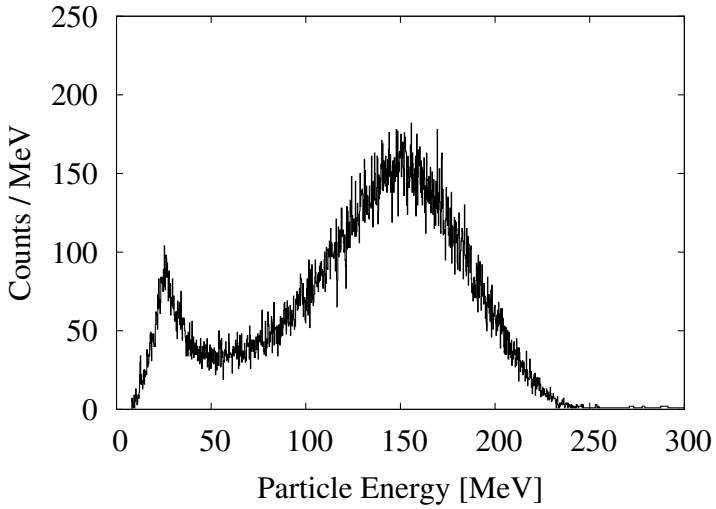

Figure 3.2: Representative PIN spectrum taken during the in-beam target test run, using a 355 mg/cm^2 Au target layered with a 110 mg/cm^2 Fe target, positioned normal to the beam axis. The PIN energy is calibrated (see text), and the ^{38}S centroid energy is 140 MeV.

consisting of a 0.75 mm layer of fast BC-400 plastic scintillator and a 2" layer of slow BC-444 plastic scintillator. The phoswich was viewed by a single photomultiplier tube (PMT), which was coupled to the scintillators by an acrylic light guide. The light guide and PMT had a thin layer of optical grease to couple them. The slow scintillator was attached to the light guide with optical epoxy, and the fast plastic was simply placed in contact with the slow scintillator and held in place by a thin wrapping of aluminized mylar for light tightness. The scintillators were disks with 4" diameters, and the PMT was a Hamamatsu PMT/base assembly with a 2" diameter. More details about the operation of phoswich detectors and the description of the actual phoswich detector built for the HVTF g-factor measurements will be given in § 3.4.

The PIN detector was calibrated using a ^{228}Th α source as well as ΔE signals from attenuated primary beam having a known $B\rho$, which were sent through the PIN without the AuFe target in the beamline, from which the calibration $E = (0.2253/\text{channel} \cdot \text{X} + 3.683)$ MeV was deduced to convert from channel number X to

energy. The PIN detector measurements showed that the ^{38}S energy was ∼800 MeV after the Au layer, and that the ions exited the Au and 110 mg/cm^2 Fe foil combination in a distribution between 80 and 200 MeV, with a peak value at ∼140 MeV, seen in Fig. 3.2. The phoswich detector showed that the majority of the projectiles emerged from the target without undergoing nuclear reactions. The test established that the Au and 110 mg/cm^2 HVTF target was appropriate for slowing the beam into the peak of the transient field strength.

3.3 Coulomb Excitation of ^{38,40}S Isotopes

3.3.1 Segmented Germanium Array

The Segmented Germanium Array (SeGA) is an array of n-type high-purity germanium solid-state γ-ray detectors [102]. Each germanium crystal is cylindrical, with a length of 8 cm and a diameter of 7 cm. Each crystal has a closed-end coaxial geometry with a lithium-diffused central contact to detect the full energy signal from the crystal. The outer surface of the crystal is an ion-implanted p-type contact, which is etched into four azimuthal segments and eight longitudinal segments, giving a total of 32 segments per crystal. Fig. 3.3 shows the segmentation geometry, and Fig. 3.4 shows a view of a complete SeGA detector, which has the crystal cryostat mounted at a 45° angle to the liquid nitrogen dewar in order to allow detector positioning with the fine segmentation axis facing the beam axis for Doppler correction purposes,

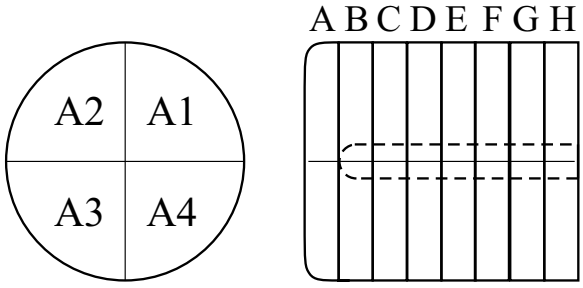

Figure 3.3: SeGA detector crystal segmentation naming convention.

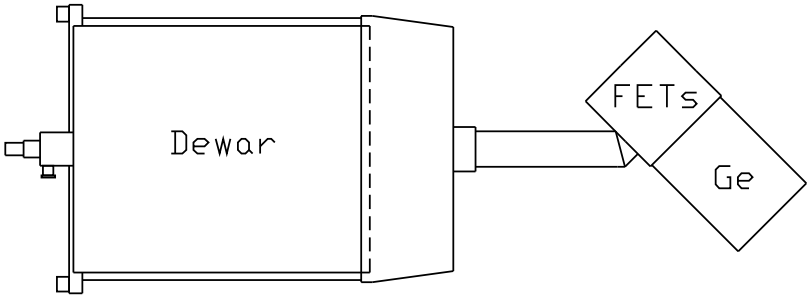

Figure 3.4: The SeGA detector consists of a liquid nitrogen dewar and a thin-walled (< 1 mm) aluminum cryostat containing the single Ge crystal. The Field Effect Transistor (FET) compartment is situated near the crystal compartment but outside of the cryostat so that the FETs are at room temperature. The preamplifiers are located in the angled section on the dewar.

which are discussed in §4.2.2. The signals from the segments can give information on the γ-ray interaction points within the crystal volume, and a measure of the energy deposited by the γ ray in each segment that was hit. The segment energy signals were calibrated relative to the central contact energy using a procedure outlined in Ref. [103]. Conventional electronics were used and the γ-ray interaction points were assigned to the centers of any hit segments.

Angular Distribution Configuration

A stand was constructed at the NSCL for the purposes of SeGA γ-ray angular distribution measurements using intermediate-energy beams [104]. The stand was designed so that SeGA would be sensitive to the angular distribution as a function of the polar angle θ. Since the scattered projectiles are detected symmetrically about the beam axis, the γ-ray angular distribution is insensitive to the azimuthal angle ϕ. However, the precession induced by the transient field occurs about the applied magnetic field axis, which is oriented along the vertical axis. Therefore, the sensitivity of the Ge detectors to the precession is maximized in the plane perpendicular to the magnetic field, and decreases to zero sensitivity at $\phi = 0^\circ$ or 180° (Ge detectors located directly above or below the beam axis). The Cartesian coordinate axes are shown in Fig. 3.5.

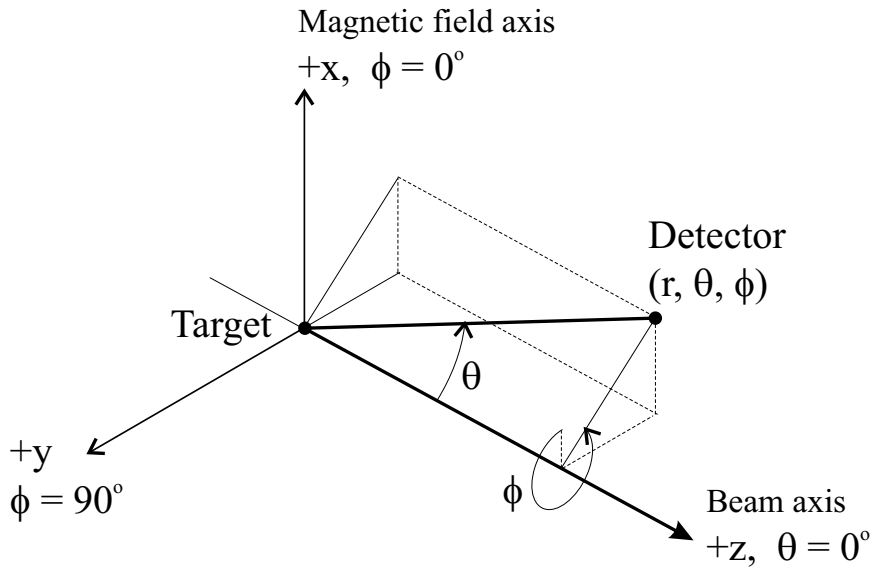

Figure 3.5: Relation between beam axis, magnetic field axis, and the Cartesian and spherical polar coordinate systems used in this dissertation.

For the TF g-factor measurements, sensitivity also increases with the slope of the γ-ray angular distribution. Intermediate-energy Coulomb excitation populates excited states predominantly in the $m = \pm I$ magnetic substates, and in the specific case of a 2^+ excited state transitioning to a 0^+ ground state, the transition is necessarily dominated by $\Delta m = \pm 2$ (since the 0^+ state has only the substate $m = 0$). A $\Delta m = \pm 2$, $2^+ \rightarrow 0^+$ angular distribution has its greatest slope near $\theta_{nuc} = 25°$ and $\theta_{nuc} = 155°$, where θ_{nuc} is the angle in the projectile frame measured from the downstream beam axis. The shape of the angular distribution for Coulomb-excited intermediate-energy beams always has a zero point in the slope at $\theta = 90°$ in the projectile frame, so it is advantageous to avoid 90° and cluster the detectors at angles near the beam axis.

The SeGA stand design for intermediate-energy beam γ-ray angular distributions takes into account the large degree of Lorentz boosting that focuses the γ rays forward, so that even an isotropic γ ray in the projectile frame will have fewer counts in the backward hemisphere and more counts at forward angles in the lab frame. In the standard SeGA angular distribution configuration, the detectors in the horizontal plane were placed as seen on the left side of Fig. 3.6. The back-angle detectors were

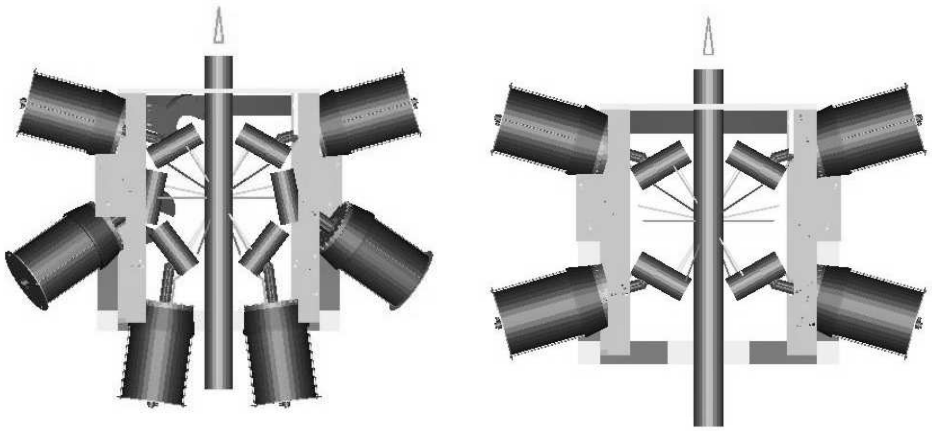

Figure 3.6: The detectors in the horizontal plane for the intermediate-energy γ-ray angular distribution measurements (left) and the TF g-factor measurements (right). The beam axis, indicated by the arrow, determines $\theta = 0^\circ$.

located at $\theta = 127^\circ$ and there are also detectors at 78°. The TF g-factor measurements are done with slower beams, and the Lorentz effect is not as pronounced as it is for the angular distribution measurements with full-energy beams. Therefore, an alternate configuration was designed in which the same stand can have the 127° detectors "flipped" so that the crystals are located at $\theta = 151^\circ$, close to the optimum slope. Part of the TF configuration is seen on the right-hand side of Fig. 3.6, which shows the detectors located in the horizontal plane. Because of the geometry of the SeGA liquid nitrogen dewars, it was not possible to include the 78° detectors in this configuration. Since the 78° detectors are close to 90°, they would offer very little sensitivity to the spin precession and their removal would not impact a g-factor measurement.

The full SeGA configuration for the TF g-factor measurement is shown in Fig. 3.7. There are two detectors for each position in θ, located at azimuthal angles ϕ and $\phi + 180^\circ$. For the actual experiment, one of the detectors at $\theta = 90^\circ$ was not installed because it would be mostly blocked by the magnet return yoke (discussed in § 3.5). On the side without the magnet yoke, the 90° detector was installed. Another SeGA detector normally included in this configuration, the $\phi = 180^\circ$ detector, could not be installed due to space constraints caused by the magnet support frame. As was

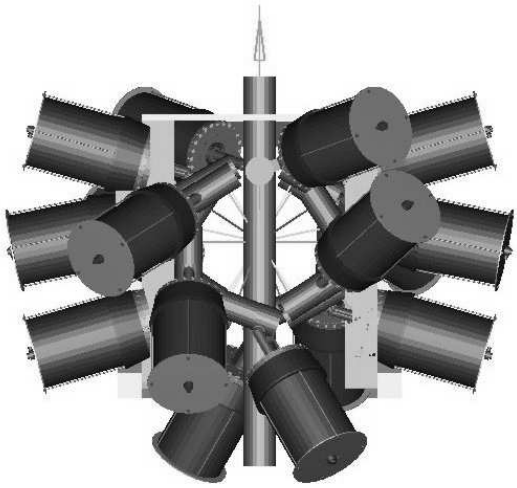

Figure 3.7: Drawing of the full SeGA configuration designed for the TF g-factor measurements.

previously discussed, the $\phi = 180^\circ$ detector would have zero precession sensitivity, and was left out. In total, 14 detectors were used for the g-factor measurements: six pairs at $\theta = 29^\circ, 40^\circ, 60^\circ, 139^\circ, 147^\circ, 151^\circ$, and single detectors at $\theta = 24^\circ$ and $\theta = 90^\circ$.

Prior to the experiment, the detector positions were measured with a theodolite system to provide accurate position information for Doppler correction. The measurements determined the relative coordinates between the center of the stand (target position) and several reference points on the outside of the SeGA crystal cryostats. Detector positions were measured — instead of simply using coordinates from a CAD drawing — to account accurately for the flexing of the SeGA stand when the detectors were mounted. The locations of each germanium crystal segment relative to the outside of the crystal cryostats were previously catalogued for each SeGA detector by Miller [105], and this information was combined with the theodolite detector position measurements to find the segment positions relative to the SeGA stand target position. For more information on the theodolite measurement procedure and the SeGA stand construction, see Ref. [104].

3.3.2 Maximum Scattering Angle and Alignment

A maximum scattering angle was chosen for the Coulex process, based on the relation between the impact parameter and center-of-mass scattering angle given in Eqn. 2.25, and transformed into the lab frame using Eqns. 2.28-2.30. The resulting lab angle was $\theta_{max} = 5.5°$, corresponding to an impact parameter of touching spheres plus $\sim$1 fm at the entrance of the gold layer. The plan was to enhance the Coulomb excitation yield above that of a smaller angle with a greater separation between projectile and target (of course, soon after entering the gold layer, the projectiles lose energy and the projectile-target separation distance increases for a fixed scattering angle). A similar approach has been used in other transient field measurements utilizing Coulomb excitation, although at much lower energies (see, *e.g.*, Ref. [106]). With the theory of Coulomb excitation, implemented in the program GKINT [107], the statistical tensors were calculated for ^{38,40}S scattering on gold to the maximum angle of 5.5°, taking into account the slowing-down process in the gold layer which changes the adiabacity parameter and therefore the statistical tensors. Cross-section weighted statistical tensors for decays occurring after the transient field layer were obtained for the two isotopes, with ^{38}S having $\rho_{20} = 0.3016$ and $\rho_{40} = 0.0326$, and ^{40}S having $\rho_{20} = 0.3647$ and $\rho_{40} = 0.0435$, indicating an effective alignment of 56% for ^{38}S and 68% for ^{40}S, for the decays occurring in vacuum beyond the target. More details of the GKINT calculations as well as the measured angular distributions will be presented along with the data analysis in § 4.2.3.

3.3.3 Slope of Angular Distribution and Sensitivity

The sensitivity of the SeGA detectors to the spin precession of the γ-ray angular distribution depends on the logarithmic slope $S(\theta) = \frac{1}{W}\frac{dW}{d\theta}$ of the angular distribution at the SeGA angles, and the number of γ rays counted at those angles. Differentiation of the angular distribution with respect to θ yields, for the detectors located in the

plane perpendicular to the magnetic field,

$$S(\theta) = -\big(a_2 P_{21}(\cos\theta) + a_4 P_{41}(\cos\theta)\big)/W(\theta), \tag{3.1}$$

where P_{21} and P_{41} are the associated Legendre polynomials. Since the precession occurs about the magnetic field axis, the spherical polar coordinate unit vector does not correspond to the direction of rotation for detectors located out of the plane perpendicular to the magnetic field. Instead of $\partial/\partial\theta$, the directional derivative of the angular distribution $W(\theta)$ should be taken about the magnetic field axis, in the direction of the angular coordinate in a cylindrical coordinate system (where the cylinder axis coincides with the magnetic field axis). The logarithmic slope for a detector located at coordinates (θ, ϕ) is $S(\theta, \phi) = S(\theta)\sin\phi$, with $S(\theta)$ given by Eqn. 3.1. In the design of the SeGA stand, care was taken to place detectors as close as physically possible to the beam axis (corresponding to the smallest possible θ), while keeping the crystal axes tangent to spheres centered on the target (to take advantage of the angular sensitivity of the segmentation). The detectors placed at $\theta = 29^\circ$ and $\theta = 151^\circ$ (the two pairs shown in Fig. 3.6) represent the best physically-achievable detector placement consistent with a 4" beampipe. The four detectors at $\theta = \pm 29^\circ$ and $\pm 151^\circ$ dominate the total sensitivity of the array, since they are located near the angles of maximum $S(\theta)$, and $\sin\phi = 1$ in the plane perpendicular to the magnetic field.

3.4 Phoswich Detector

A beam particle detector was designed for use in detecting the ^{38,40}S ions exiting the HVTF target. The selected phoswich detector served as the trigger to look for particle-γ coincidences between scattered particles near the beam axis and γ rays de-exciting the nuclear level under investigation.

3.4.1 Design and Construction

There were several parameters used to decide on the design of the phoswich detector. Of prime importance was the ability of the detector to handle high event rates. Since the detector is situated over an angular range from 0° to some angle θ_{max}, it has to detect a very high fraction of the incident beam, on the order of 10^5 particles per second in the case of ^{38}S. Such a high rate prohibits the use of solid-state detectors which would succumb to radiation damage. Plastic scintillators have very fast fluorescent times of order nanoseconds, and can survive particle rates of 10^5/s. Another important characteristic for the particle detector is the ability to identify particles. The most common technique for particle identification is the ΔE-E method, where two detectors are used to measure an energy loss (ΔE) and a residual energy (E). According to the Bethe-Bloch formula, charged particles generally deposit an amount of energy that is proportional to their atomic number Z^2. The residual energy left after passing through the energy loss detector is collected by a second detector, which is thick enough to stop the particles. The total energy is proportional to the particle mass. To employ a ΔE-E method with plastic scintillators, it is convenient to use a "phoswich" design. The term phoswich comes from the phrase "phosphor sandwich," meaning multiple layers of scintillating materials. Using two different scintillators that have very different light emission characteristics, the light emitted as charged particles pass through one layer and stop in the next layer can be detected with a single photomultiplier tube and separated using pulse-shape analysis.

The basic phoswich design chosen was a fast/slow plastic scintillator design similar to that previously employed for intermediate-energy Coulomb excitation at the NSCL [10, 108]. A 0.75 mm layer of fast BC-400 plastic scintillator and a 2" thick layer of slow BC-444 plastic scintillator were supplied by Bicron Corporation. The organic scintillators are polyvinyltoluene-based materials with densities of 1.032 g/cm^3, primarily consisting of hydrogen and carbon. The two scintillators have very different time characteristics. BC-400 has a fast decay time of 2.4 ns and BC-444 has a decay

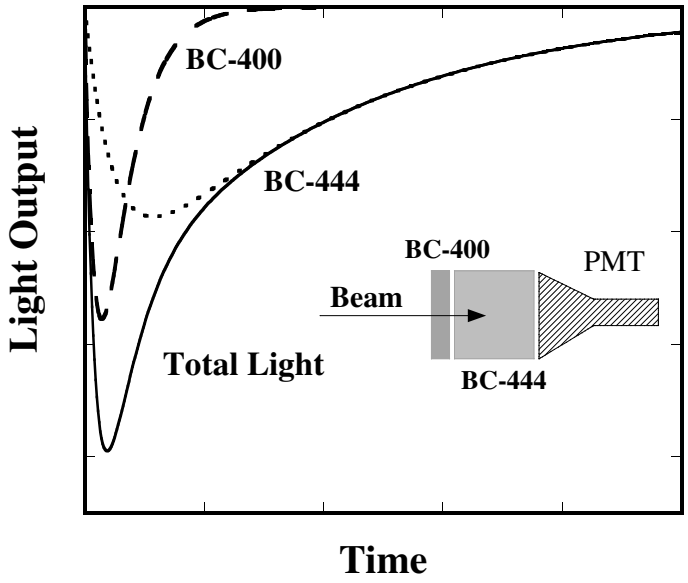

Figure 3.8: Components of phoswich light from the different types of plastic scintillator. The light from the fast BC-400 is shown as the dashed line, the slower light from the BC-444 layer is shown as the dotted line, and the solid line is their total. Pulse-shape analysis can be used to discriminate between particles that penetrate the fast plastic layer or stop in it.

time of 180 ns [109]. When a charged particle traverses both layers of the phoswich, light is emitted by both layers with two characteristic time profiles, shown in Fig. 3.8. Analyzing different time regions of the pulse reveals the amounts of "fast" and "slow" light, providing a measurement of ΔE-E. Since the particles being detected by the phoswich are heavy ions of $Z \sim 16$ and kinetic energy $E \sim 150$ MeV, they are weakly-penetrating particles. The consequence is that the ion range in plastic is only around 40 μm. In order to perform a ΔE-E measurement, a fast plastic layer of thickness $< 40\mu$m would be required. It was decided instead to use a "thick" fast plastic layer of 0.75 mm, which is a macroscopic thickness that is rugged enough to be handled and that will stop all the heavy ions before they reach the slow plastic. If nuclear reactions occur inside the target and result in lower-Z ions accompanied by protons or alpha particles, then the slow scintillator will emit light due to the penetration of such lower-Z particles through the fast plastic layer. The beam purity for the ^{38,40}S was projected to be high, and a test run proved that, for ^{38}S, the purity was $> 99\%$.

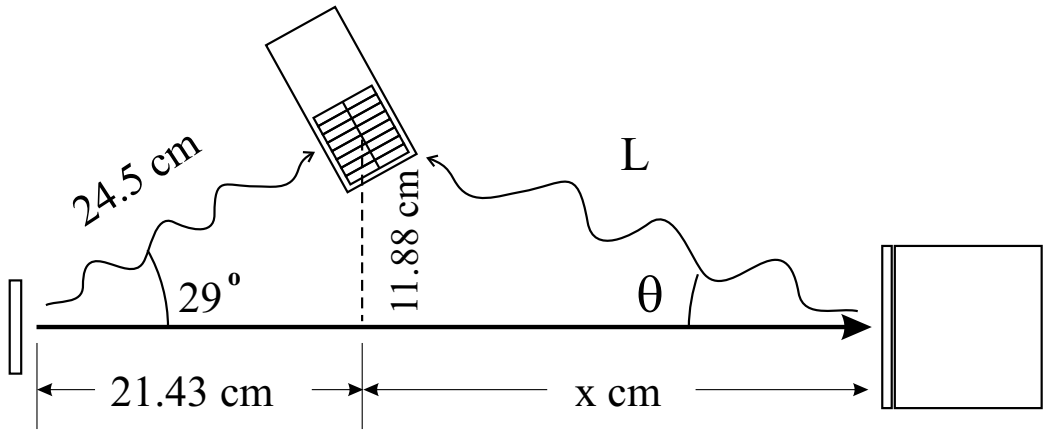

Figure 3.9: Geometry affecting difference in arrival times for γ rays emitted from the target and γ rays emitted from the phoswich. The phoswich position affects the particle flight time from the target as well as the the γ ray flight time from the phoswich to the Ge detector.

This eased the requirement for the phoswich particle identification from unambiguous (Z, A) identification to a discrimination between heavy and light ions.

An appropriate diameter for the plastic scintillators, which were disk-shaped, needed to be determined. The role of the detector was to limit the maximum particle scattering angle to θ_{max}, accomplished by placing the detector at a distance ℓ from the target position such that

$$\tan\theta_{max} = \frac{r_{phos}}{\ell}, \tag{3.2}$$

where r_{phos} is the phoswich radius. The dimension ℓ was selected to place the detector at a sufficient distance from the target to allow the possibility to distinguish between γ rays originating from Coulomb excitation in the target and γ rays originating from the beam hitting the phoswich detector. The time response of the SeGA detectors is about 25 ns [110], and the distance ℓ needed to satisfy the condition that the arrival times of γ rays coming from the target and the phoswich had a separation of 25 ns, as presented in Fig. 3.9. The SeGA detector at 29° was selected for the purpose of the calculation since it is one of the detectors located closest to the phoswich. Beam

particles were assumed to leave the target with 230 MeV kinetic energy, corresponding to a velocity of 3.404 cm/ns for a nucleus of mass number 38. The velocity is essentially an upper limit for particles exiting the HVTF target. The propagation time of a γ ray between the target and the 29° detector was calculated. The time for the particle to travel from the target position to the phoswich, and then for a γ ray to travel from the phoswich to the 29° detector was also calculated and the relationship was determined for the difference in γ ray arrival times:

$$\Delta t_\gamma = \frac{(\mathrm{x} + 21.43)\ \mathrm{cm}}{3.404\ \mathrm{cm/ns}} + \frac{\sqrt{(11.88\ \mathrm{cm})^2 + (\mathrm{x\ cm})^2}}{30\ \mathrm{cm/ns}} - \frac{24.5\ \mathrm{cm}}{30\ \mathrm{cm/ns}}. \qquad (3.3)$$

The distance $\ell = (x + 21.43)$ cm was calculated from this relationship to be ~80 cm for $\Delta t_\gamma > 25$ ns. Using Eqn. 3.2 with $\ell = 80$ cm and $\theta_{max} = 5.5°$, a radius of 7.7 cm results. This corresponds to a detector diameter of 6.07", and for ease of manufacturing a 6" diameter was chosen. The 80 cm distance between the particle detector and the germanium array lowers the γ-ray flux that the germanium detectors see from the stopped radioactive beam in the phoswich, compared to conventional transient field arrangements that often employ small silicon particle detectors located a few cm from the target.

After choosing the scintillator radial dimensions, the next step was to design the light collection system and choose a photomultiplier tube (PMT). A fast PMT with high rate capability and good energy and time resolution is required for the application of high-rate heavy ion particle detection, and the Electron Tubes, Ltd. 9821B phototube was selected. This PMT has 12 linear-focused BeCu dynodes and a 3" (67 mm active) diameter. The linear-focused design generally has very good timing characteristics and pulse linearity. From an efficiency standpoint, the larger the PMT diameter the better, because from the conservation of photon flux per unit solid area, the maximum fraction of light that can be collected is the ratio of the PMT active area to the area of the scintillator cross section. The light collection efficiency,

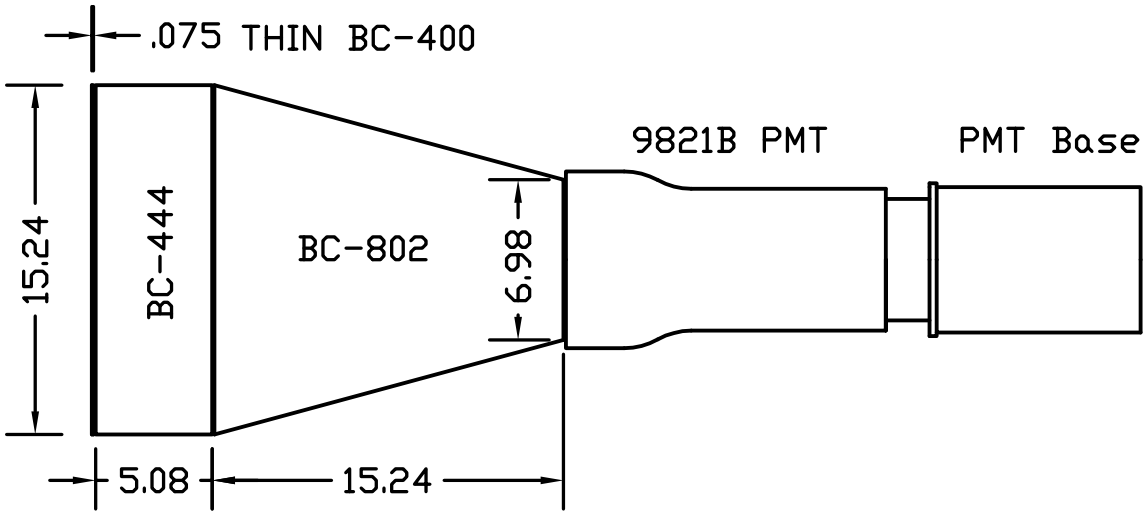

Figure 3.10: Side view of the phoswich detector, including the scintillators, light guide, photomultiplier tube, and voltage-divider base. Dimensions are in centimeters.

therefore, has a theoretical upper limit of the ratio of the squares of the radii of the two components, or $(r_{PMT}/r_{phos})^2$, which is $\sim$0.19.

Light collection uniformity, i.e., the dependence of the light collection on particle position, was a higher priority for the light collection system than total efficiency. A non-uniform light collection could mean that particles of the same energy but a different implantation position will appear to have different energies. The large diameter of the scintillators means that light emitted near the edge of the detector is probably less efficiently collected than light emitted directly on the axis of the cylindrical scintillator. In order to maximize the light collection uniformity, a light guide was designed that tapered from the 6" scintillator diameter to the PMT diameter over a distance on the order of the scintillator diameter. The shallow angle of the light guide enhances the collection of light emitted near the edge of the scintillator. Placing the PMT 6" back from the scintillator also ensures that the PMT views the entire scintillator volume in a more uniform way than it would if a short light guide was used. The phoswich assembly is depicted in Fig. 3.10. The light guide was made of polished acrylic and joined by the manufacturer to the BC-444 slow plastic scintillator with BC-600 optical epoxy. The PMT was attached to the light guide with Tra-Bond F113

optical epoxy. The thin fast plastic layer was secured in place by aluminized mylar foil. No optical coupling was used in between the fast and slow plastic layers (such as optical grease) because any material would introduce a dead layer of inherently non-uniform thickness.

The type of reflective wrapping to use for the phoswich was considered carefully, since wrapping was needed to hold the fast and slow pieces of scintillator together. It is important to have a very thin and uniform layer of material on the front face of the fast scintillator, to avoid attenuating the weakly-penetrating heavy ions. Aluminized mylar was chosen since it is highly reflective and serves to reflect light from the scintillators back towards the PMT. Three options were considered for the sides of the scintillators and light guide: no wrapping, a specular reflecting material, or a diffuse reflecting material. To use no wrapping is to rely on internal reflection alone for the light collection. Internal reflection reaches 100% when the condition of *total internal reflection* (TIR) is met. TIR occurs when light is incident on a boundary between regions of different indices of refraction, and the angle of incidence is less than a critical angle defined by

$$\theta_{crit} = \sin^{-1} \frac{n_1}{n_0}, \tag{3.4}$$

where n_0 is the refractive index of the light guide and n_1 is the refractive index of the surrounding medium, in this case vacuum. Light will "leak" out of the light guide as the angle of incidence increases beyond θ_{crit}, in accordance with the Fresnel equations [111]. There will be position-dependent light collection because of the correlation between the angle of incidence and the amount of reflected light that reaches the PMT. A better solution is to wrap the phoswich with a reflective material to try to catch light that leaks out of the light guide. A specular reflective material is one that obeys the Reflection Law (where the angle of reflection equals the angle of incidence), and is usually shiny in appearance. There is also a large degree of corre-

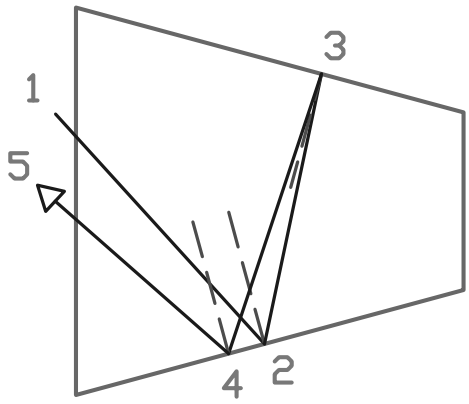

Figure 3.11: A light ray undergoing specular reflection in the light guide. Points along the ray trajectory are labeled numerically in order of occurrence. This trajectory results in the light ultimately being reflected away from the PMT because of the angled light guide.

lation between the light that reaches the PMT and its initial emission position when specular reflectors are employed. In fact, since the light guide gets narrower from the scintillator to the PMT, some light can be reflected away from the PMT, as can be seen in Fig. 3.11. To minimize the correlation between initial position and the fraction of collected light, a diffuse reflector (white Teflon tape) was selected. Diffuse reflectors obey Lambert's Law, where the distribution of reflected light has the form

$$W(\phi) \propto \cos\phi, \tag{3.5}$$

with ϕ denoting the reflection angle. Eqn. 3.5 demonstrates that the reflected light is independent of the angle of incidence, and is peaked around 0° (normal to the surface). In this case, a large amount of mixing occurs for the light as it is reflected in the light guide and there is less correlation between the initial light position and the amount that ultimately reaches the PMT.

3.4.2 Characterization of Phoswich Detector

The light output of the phoswich is the sum of two components, a fast and slow light pulse. The relative magnitude of the fast and slow light is determined by how much

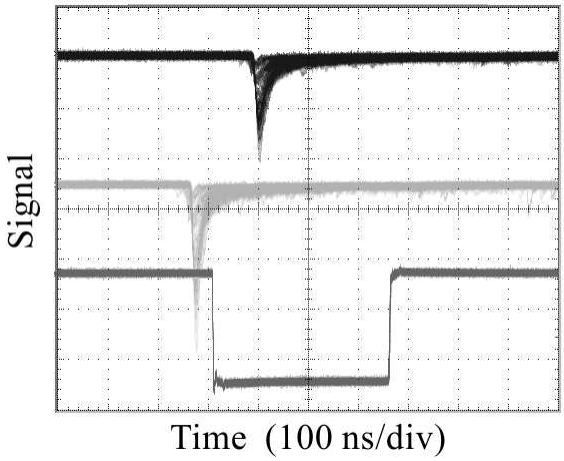

Figure 3.12: Oscilloscope trace showing the two phoswich signals with a relative delay between them, and the common QDC gate. The gate intersects the signals in different regions and the comparison of the two regions accomplishes the pulse-shape analysis.

ionization is caused by the charged particle, electron, γ ray, or neutron as it travels through the scintillator. In order to analyze the relative magnitudes of the fast and slow light, pulse-shape discrimination was accomplished by charge-integrating different parts of the phoswich pulse using a Charge-to-Digital Converter (QDC). The QDC used was a CAEN Model V792 Charge-to Digital Converter, which has 32 channels that integrate the incoming charge falling within a selected time window. Pulse-shape discrimination is possible using the V792 module by splitting the phoswich signal into two and delaying one relative to the other. The full pulse shape is integrated in one channel of the QDC and only the tail of the same pulse is integrated in another channel. An oscilloscope trace of the two signals is shown in Fig. 3.12. The actual scintillation light pattern is preserved during the amplification process in the photomultiplier tube, but the electronics beyond the PMT anode has a particular RC time constant as it responds to the current produced by the PMT, stretching the signal in time.

The phoswich detector PMT was biased to -1700V using a Canberra High Voltage Power Supply. The PMT base, which was designed and built at the NSCL, had two outputs. One output is positive and originates from the first dynode of the PMT and

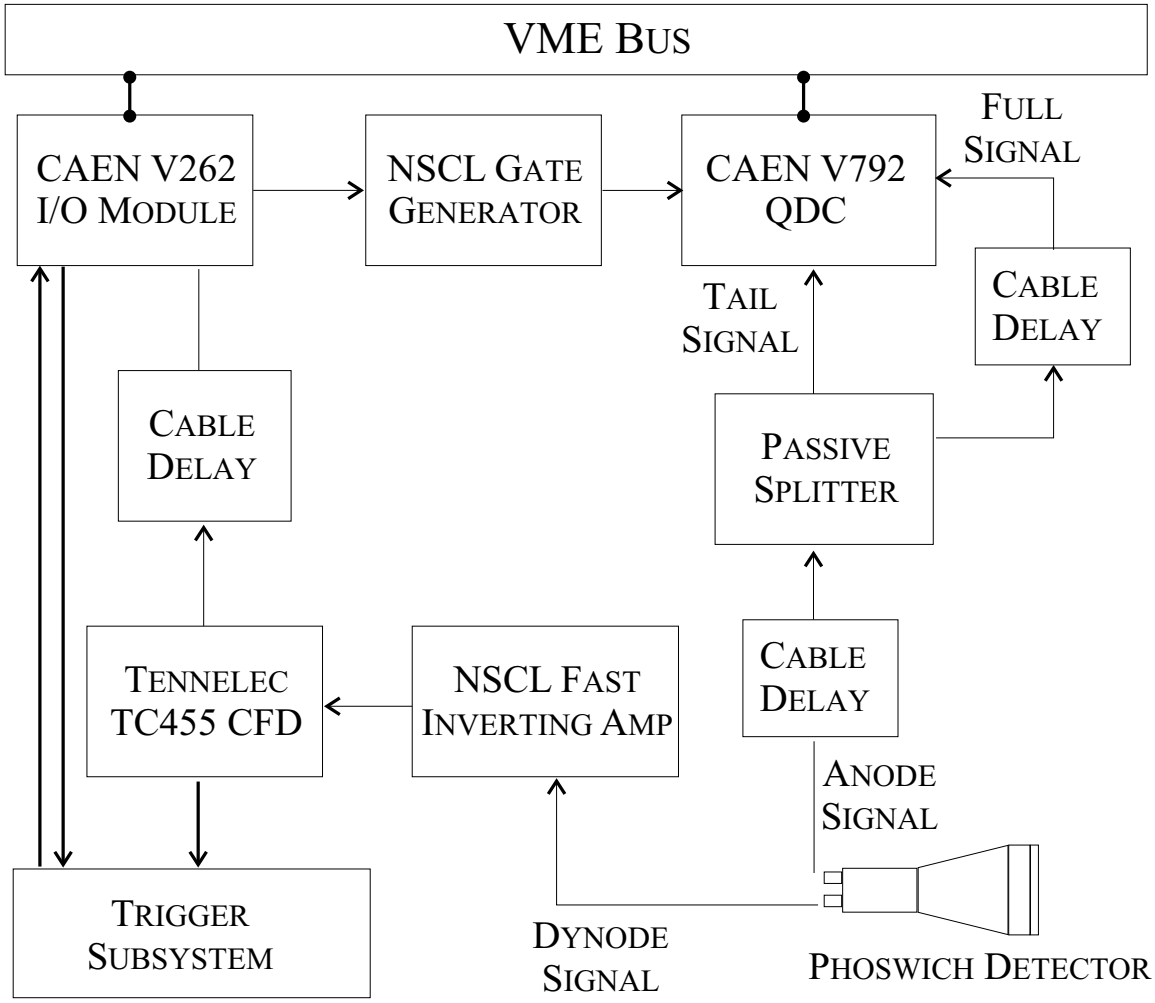

Figure 3.13: Electronics used in the phoswich subsystem. Two signals originating from the PMT base were used for timing and energy analysis. The positive signal from the first dynode of the PMT was inverted and discriminated with the TC-455 CFD for timing and triggering purposes. The signal after all 12 dynode stages was passively split into two and sent to the charge-integrating ADC (QDC) with a relative delay between them. Both energy signals were integrated with a common gate started by the CAEN V262 I/O Module.

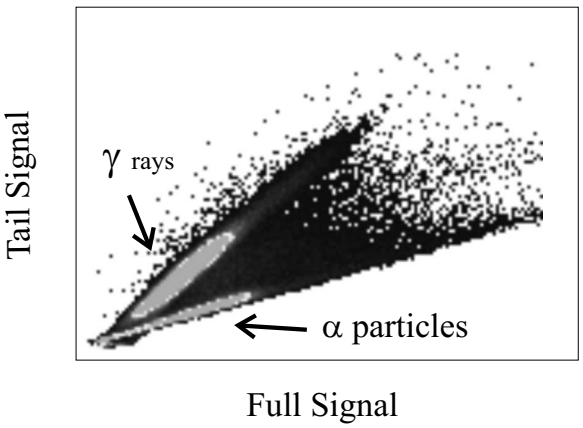

Figure 3.14: Spectrum taken using a ^{241}Am α source and a ^{60}Co γ-ray source. The γ rays are primarily along the slow (tail signal) axis and the α particles are along the fast (full signal) axis.

was used for timing. The other output is the negative anode signal which comes after amplification by all 12 dynode stages. The positive dynode signal was sent through an NSCL fast inverting shaping amplifier and was used as input for a Tennelec TC-455 Constant Fraction Discriminator, which produced the timing signal. A rotary attenuator and the fast amplifier gain could be adjusted to control the amplitude of the input to the CFD. The negative anode signal was passively split into two components, and a cable delay of 100 ns was used for one of the signals to allow pulse-shape discrimination. A master live gate signal that was created by the logical AND of the CFD signal and a computer NOT-BUSY signal opened a QDC integration gate for 300 ns. The management of the master live gate was done using the NSCLDAQ [112] readout software that communicated via the LEMO outputs of the VME V262 I/O module.

Radioactive sources that emit different types of radiation were used to characterize the phoswich detector. The goal was to ensure that the different types of radiation could be distinguished by pulse-shape discrimination, and it was found that there was a discernible difference between the radiation types. The α particles emitted by typical α sources such as ^{228}Th or ^{241}Am generally have $\sim$5 MeV of energy, with a maximum of $\sim$8 MeV for one α emitted by ^{228}Th. Such particles can not penetrate

the 0.75 mm fast plastic and therefore only give rise to fast scintillation. The ^{228}Th chain, however, also includes β-decaying daughters as well as de-excitation γ rays from the resulting nuclei, and those radiations have greater penetrating power, leading to slow scintillation (in the case of γ rays, almost exclusively slow scintillation). The sources used were ^{137}Cs, which emits a single γ ray of energy 662 keV; ^{60}Co, which emits two γ rays of energies 1172 keV and 1333 keV; ^{90}Sr, which emits β particles with an endpoint of 546 keV, and subsequently the ^{90}Y daughter emits β particles with an endpoint energy of 2.3 MeV; ^{241}Am, which emits a 5 MeV α accompanied by a 60 keV γ ray; and ^{228}Th, which has a complicated decay chain including α, β, and γ radiation. A representative spectrum from the ^{60}Co and ^{241}Am sources is shown in Fig. 3.14.

Signals consisting of purely fast pulses should in principle only contribute to the "full signal" and not to the "tail" signal, whereas signals consisting of only slow pulses should be identical in both the "full" and "tail" integrated regions. In practice, there is always some of each type present in each integrated region, which causes a departure from a 45° angle between the "full" and "tail" signals when they are plotted against each other.

3.4.3 High Count Rate Behavior

A test was undertaken to determine the effect of count rate on the phoswich performance. The test was performed at two PMT bias voltages, -1700V and -2000V. A ^{241}Am alpha source with an activity of 100 μCi was used for the test. The α particles from the decay of ^{241}Am have energies of $\approx$5.6 MeV and either directly populate the ground state of ^{237}Np or an excited state which emits a 60 keV γ ray. Neither α particle can penetrate the 0.75 mm BC-400 layer and therefore only cause fast scintillation. The resolution of the plastic scintillator is not sufficient to separate the two α particles that are separated by 60 keV.

The test was conducted in vacuum to eliminate attenuation of the α particles on

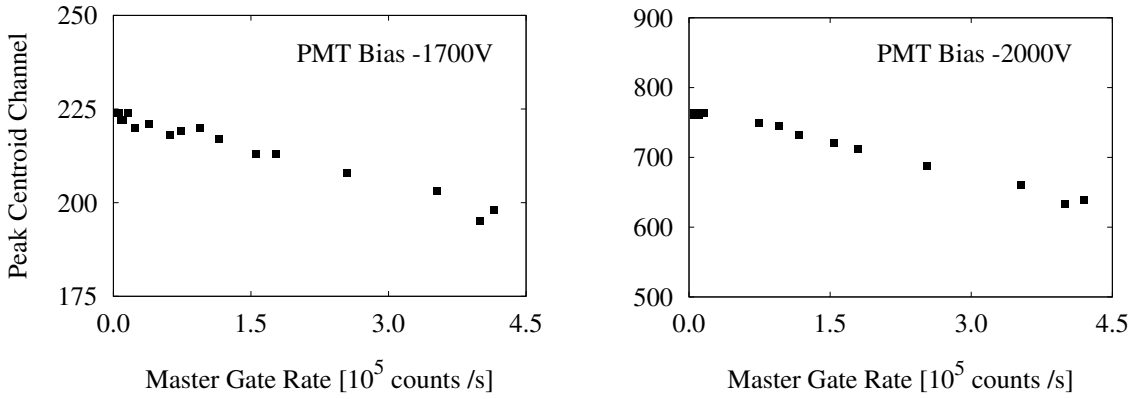

Figure 3.15: Centroid of ^{241}Am α particles as a function of α particle rate resulting from changing the source-detector distance, for a PMT bias of -1700 V (left) and -2000 V (right). Note the change in vertical scales.

the path from the source to the detector. The 100 μCi ^{241}Am source was fixed to the blanked-off end of a 10" beampipe and the phoswich detector was moved in 17 steps from 2 to 74 cm from the source, resulting in count rates from 420,000 to 5,000 master gates per second.

At each source distance and PMT bias voltage setting, charge-integrated spectra were recorded and a two-dimensional figure was plotted showing the full pulse spectrum versus the tail spectrum. The characteristics of the full pulse spectrum, which is most sensitive to the fast plastic scintillator, was the main observable of the test. The peak centroids were determined and the behavior with -1700V PMT bias is shown in Fig. 3.15. The peak centroids shift as a function of count rate, with a 5% shift observed at 150,000 counts per second and a 10% shift observed at 400,000 counts per second. The PMT behavior at -2000V was similar to that at -1700V, with a 5% gain shift at 150,000 counts per second and a 10% shift at 400,000 counts per second.

An appreciable deviation of gain was observed with rates in excess of 10^5 α particles per second, and since the sulfur projectiles in the g-factor measurement stop in the fast plastic layer, the same qualitative rate-dependent behavior would be expected when sulfur ions are implanted into the phoswich. At the highest rate of 420,000 par-

ticles per second, the α peak quality was visibly diminished as the peak shifted down towards the lower level threshold. To guarantee undiminished performance of the phoswich detector at the 10^5/s rate expected for the ^{38}S fragments, a Pb mask was designed to block the angular range 0°-2.5°, where the Rutherford scattering cross section is very high but the Coulomb excitation probability is low due to the large impact parameter. No mask was used in the ^{40}S runs since the particle rate was an order of magnitude lower and pileup and gain shift effects were not appreciable.

3.5 Compact Electromagnet

An external magnetic field that polarizes the ferromagnetic target layer was required to utilize the transient field. It is reasonable to expect that the transient field effect scales with the magnetization of the ferromagnetic host material (the magnetization dependence is explicitly written in the Rutgers parametrization, Eqn. 2.10). Since ferromagnetic materials exhibit a saturation magnetization for a particular applied magnetic field strength B_{sat}, nothing is gained by applying a stronger magnetic field than B_{sat}. For polycrystalline iron, the magnetic field strength required to fully align all magnetic domains is on the order of 10^{-1} T, or ∼1000 G [113], and can be lower depending on the iron sample and foil geometry. A magnetic field strength of ∼1000 G is readily available with permanent magnets, but because the execution of a TF g-factor measurement relies on reversing the magnetic field direction periodically in order to increase the measured effect and cancel most systematic errors, an electromagnet is usually used. This section will describe the parameters of the electromagnet solution designed for TF g-factor measurements at the NSCL.

3.5.1 Design and Construction

Several physical constraints were included in the electromagnet design. The magnet and target chamber needed to fit inside the SeGA stand, which holds the SeGA

detectors with their crystal centers 24.5 cm away from the target position. Taking into account the crystal cryostat diameters, the magnet and target chamber were constrained into a cylindrical space with a diameter of ∼40 cm. The target foils had dimensions 26 x 26 mm^2, chosen to accommodate the projected beamspot size realized for experiments run in the N3 vault. The width of the magnet poles was designed to be no smaller than the target width to ensure full target foil saturation. The target foils were held in a target frame designed to secure them with a minimal amount of material on all sides. The magnet pole tips were machined with grooves to accommodate the target frame, and therefore the magnet "pole gap" was fixed at 32 mm.

Besides the physical dimensions imposed by the target frame and the SeGA stand, it was important to design the magnet such that it produced a magnetic field sufficient to magnetize the target foil with a minimum stray fringing field. A strongly-varying magnetic field can damage Ge detectors, which can experience a *Penning discharge*, or a spark at the surface of the germanium crystal which is held at several kV during normal operation. It is unlikely that a Penning discharge will occur in a magnetic field of only 1000 G. A strong magnetic field may also have an effect on the beam itself as it passes through the magnet fringe field. The steering of the beam, called *beam bending*, is usually a concern for low-energy beams and not for intermediate-energy beams. For the purpose of the magnet design, the fringing field was minimized by keeping the pole dimension short along the beam axis direction, and by choosing a "C"-magnet design that uses a return yoke to channel the magnetic flux in a well-defined region. The pole tips were also tapered from 1" thick along the beam axis to 0.25" thick where they held the target frame, to increase the magnetic flux density near the target foil. The saturation magnetic field could then be attained without introducing a large region of magnetic field along the beam direction for the beam to pass through, which would be the case if the pole tips were symmetric in dimension along the beam axis and perpendicular to it.

Table 3.2: Results of iron foil magnetization measurements [114].

Applied Field [Gauss]	Magnetization [%]
367	91
487	97
621	99

To establish the magnetic field required to saturate the iron foil, the magnetization of a piece of the same iron used for the HVTF target was measured using an AC magnetometer at Rutgers [115], with the results shown in Table 3.2. Those measurements determined the magnetization of the foil as a function of applied field, and it was concluded that the iron foil would be fully magnetized with an applied field of greater than 700 G.

Simulations were run using the code POISSON [116] to model the magnet design and to estimate the number of ampere-turns needed to produce a minimum magnetic field of 700 G at the center of the gap. The calculation included the small gaps where the magnet yoke inside and outside the vacuum was separated by the thinly-machined regions of the aluminum target chamber flanges (see § 3.7). A plot of the magnetic flux is shown in Fig. 3.16. The target value was determined to be 1200 ampere-turns. The coils were to be operated by an in-house power supply, which could deliver 20 Amps at 20 Volts. The choice was made to use a large-diameter copper wire, AWG #14 which has a resistance of 2.524 Ω per 1000 ft, and run 4.3 A through 280 turns of the 14 gauge wire to get the 1200 ampere-turns. The power dissipated per coil was calculated to be ∼20 watts. The cross sectional area of 280 turns of this wire was calculated to be a little over 1" square, which would fit in the available space on the top and bottom flanges of the target chamber.

The iron pole tips and return yoke pieces were fabricated by the NSCL machine shop from high-quality low-carbon steel. The return yoke was designed to fit on the outside of the 4" cross target chamber, and was kept close to the side of the chamber

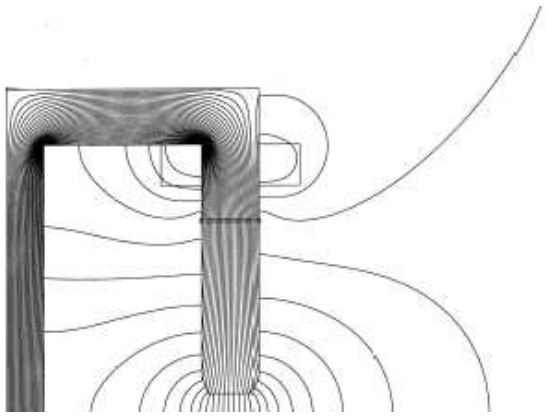

Figure 3.16: Graphical results of a POISSON calculation showing the behavior of a C-magnet including a small air gap near the coil.

in order not to protrude into the space near the SeGA detectors. The return yoke and pole tips were made in seven pieces. Two small vertical pieces attached to the top and bottom flanges with screws, and they extended 1.5" in the vertical direction to accommodate the magnet coils and coil support plates. Two horizontal sections of the return yoke connected the coil sections to the vertical return yoke section, which were all 1 in^2. The target frame was held by the upper pole tip with a set screw and rested in a groove in the lower pole piece. The target was installed by attaching it to the upper pole piece before assembling the magnet onto the target chamber. Since the return yoke was detachable, the target could be accessed by removing the top flange of the target chamber after disconnecting the yoke at the outer vertical piece.

The magnet coils were made out of AWG #14 enameled copper conductor using a coil winding station available at the NSCL. To keep the turns secure and to prevent electrical shorts, epoxy (miller-stephenson Versamid 140 and EPON® Resin 815C) was applied to the coils after each layer accumulated. In order for the coil to be removable from the form after being epoxied, all surfaces of the form were covered by 3M Teflon tape, to which epoxy does not easily adhere. Four coils were wound, with 290, 280, 260, and 259 turns.

The coils were tested using a bench top Power Designs, Inc. Model TW347D 0-16 V, 5 A power supply. Current was driven through the coils to test their heat

dissipation and to measure their current-voltage relationships. For the 290-turn coil, a voltage of 3.6 V was required to sustain a 5.55 A current after the power supply and coil were run for one hour to allow the operational temperature to be reached, for which the coil resistance would plateau. The temperature of the coil was determined to be 165°F using a RayTek MiniTemp MT gun-type infrared thermometer. To ensure safe operation, temperature switches were attached to the coils with thermally-conductive epoxy. The devices were model STO-150 switches that trip at 145-155°F, and they were wired into the control system to switch off the current should the temperature exceed that range, which was established by safety regulations. The vault pressurized air supply was used to blow air across the coils, using a regulator to obtain a pressure of 20 PSI through 1/4" diameter nylon tubing. During normal operation, the coil temperatures were ∼110°F with a current of 4.5 A (1.1 kG).

3.5.2 Hall Probe Measurements

An F.W. Bell Model 5080 Gaussmeter (a Hall probe) was used to measure the magnetic field strength as a function of magnet current. The Au and Fe target foils were secured to the target frame and the magnet chamber was fully assembled. The Hall probe was held with the sensitive area inserted in a notch near the pole tip, ensuring that it was held in a reproducible location. The magnet current was cycled at discrete values $\pm I$ and the magnetic field was recorded. A plot of the measured field strength is shown in Fig. 3.17. A magnet current of 4.5 A, corresponding to a 1.1 kG field at the pole tips, was chosen to ensure full target polarization during the run.

The magnetic field was also measured along the beam axis to characterize the fringing field. For the measurement, a current of 5.5 A was run through the coils and no target foil was in place. The Hall probe was insensitive to the magnetic field at a distance of 30 cm from the target along the beam axis. The results of the measurements are shown in Fig. 3.18. In contrast to the pole-gap field measurement shown in Fig. 3.17, the measurement shown in Fig. 3.18 has a large systematic uncertainty

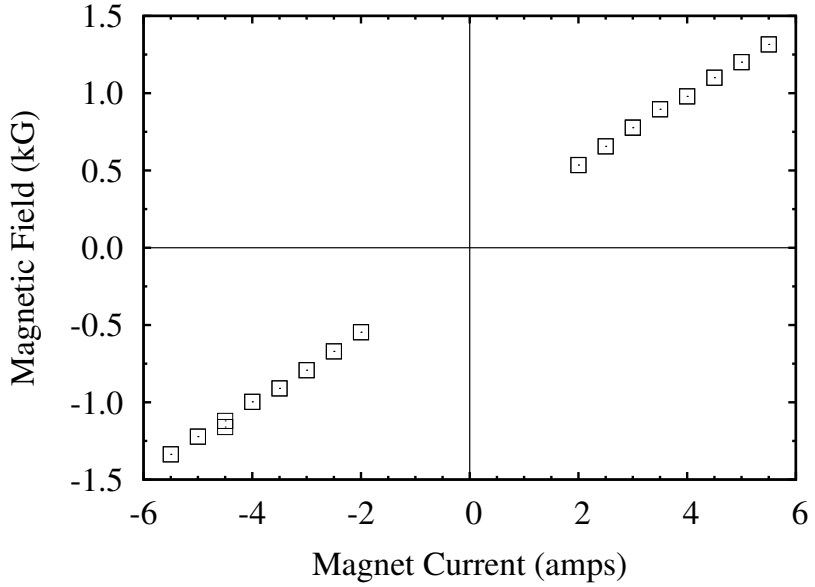

Figure 3.17: Plot of magnetic field (in kiloGauss) measured with a Hall probe for various values of the current (in amps) running through the coils.

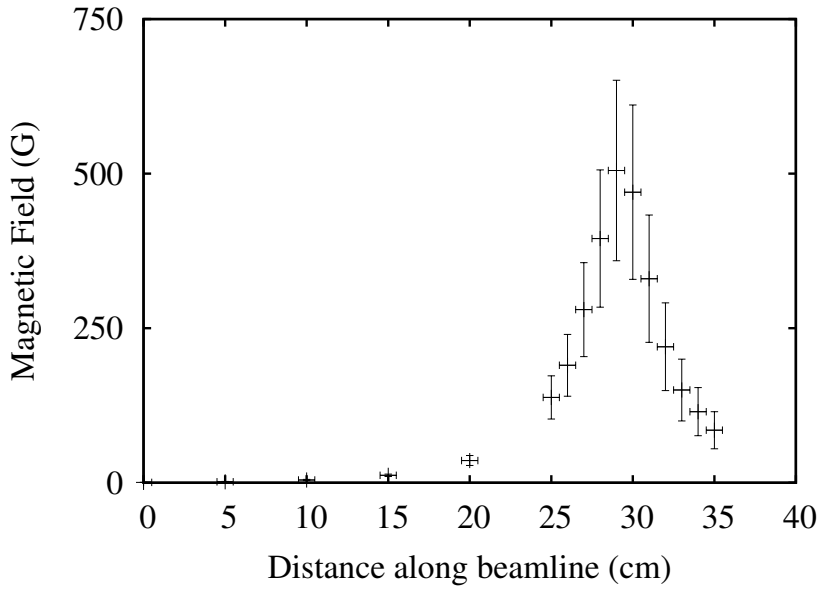

Figure 3.18: Plot of magnetic field as a function of distance along the beamline, measured from the target chamber entrance flange, without the target in place.

because the position and angle of the Hall probe could not be held rigidly in place, in a reproducible manner. This measurement gives at most a qualitative understanding of the magnetic field along the beam axis, since the presence of the iron target would be expected to narrow this magnetic field distribution near the target position. However, the Hall probe test firmly established that the magnetic field is negligible at the Ge detectors, at a ∼25 cm radius from the target.

3.5.3 Power Supply Control

The external magnetic field direction needed to be reversed at preset intervals (on the order of minutes) during the transient field g-factor measurements, in order to reduce systematic errors. Since the power supply used to provide current to the magnet coils was an NSCL-built four-quadrant power supply, it could output a current that is proportional to the control system input voltage, including the polarity. It was possible to convey information from the NSCL EPICS control system into the datastream by interfacing the magnet control system with the data acquisition (DAQ) system, and in that way the data could be sorted by field direction, which was reversed periodically.

The power supply used was the NSCL 20/20 power supply (maximum output 20 Volts and 20 amps). The power supply is designed to provide a constant current that corresponds to the "set value" that is proportional to the voltage applied from the control system; the power supply will automatically adjust the voltage necessary to run the desired current through the attached load. Large-diameter current leads were used to connect to the magnet coil leads in order to avoid transmission losses since the power supply was located ∼5 m from the electromagnet. A VME module containing an on-board computer running VxWorks was used to run a control script written for the purpose of controlling the electromagnet power supply as well as supplying the status signals to be included in the datastream. The script also had several user-selectable options to control its functionality. The user interface to the control script was provided through a PanelMate application that could run on a PC

computer. The magnet could be run in a "swapping" or a "non-swapping" mode, whereby either the magnet current would swap after a predefined number of seconds from $I \rightarrow -I$ (where the current I is set by the user), or the magnet current could simply be held constant at the value I.

3.6 Data Acquisition System

The DAQ system consisted of separate subsystems for the germanium array and the phoswich detector, which were developed and tested separately and then integrated together. The model for a DAQ system at the NSCL is to run nuclear electronics modules, standardized according to the NIM, CAMAC, or VME standards, and access the data by mapping the CAMAC addresses into the VME address space managed by a DAQ computer connected to the VME crate. In this instance, the SeGA electronics were CAMAC modules and the phoswich and PIN electronics were VME modules. Trigger logic was performed using NIM modules, and the CAEN VME I/O module shown as part of the phoswich subsystem in Fig. 3.13 was the master trigger manager for the DAQ system that interfaced between the VME bus and the DAQ computer that hosted the DAQ software. An overview of the DAQ electronics will be given here.

3.6.1 Germanium Detector Electronics

The SeGA subsystem consisted of electronics channels to process signals from the central contacts as well as the detector segments, meaning that each detector has 33 channels of energy information. Each SeGA detector has a dual output of the central contact energy, one of which is used for timing. The timing signals from each Ge detector were processed by TC-455 NIM Constant Fraction Discriminator modules, the outputs of which are combined using a logical OR gate in a NIM multiplicity logic unit. The GE-OR signal was used for the trigger logic which will be described in the next section. The Ge CFD signals were also fanned out to the SeGA Phillips 7186

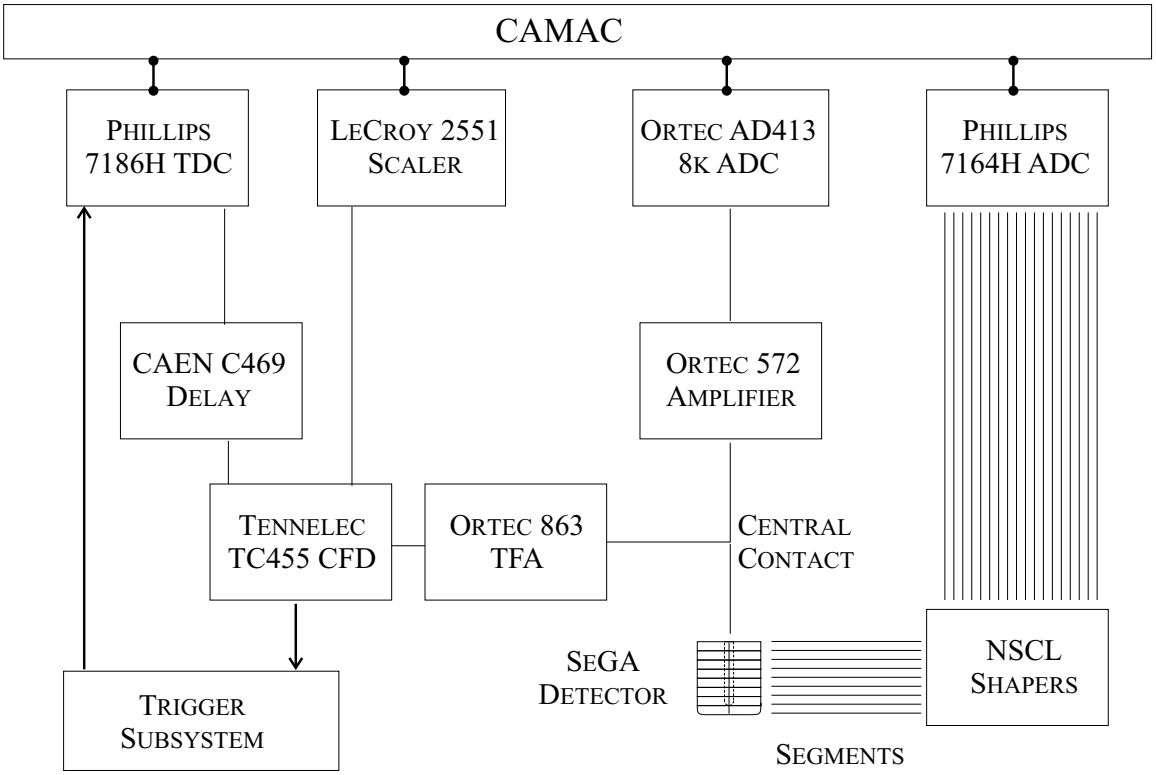

Figure 3.19: Electronics used in the SeGA subsystem. One SeGA crystal produces a full-energy central contact signal as well as 32 segment energy signals. The central contact signal is split internally, and used for timing and energy analysis. The segment signals are shaped and digitized independently of the central contact signal. The trigger subsystem starts the TDC upon registering a valid trigger condition, and individual SeGA detectors can then stop the TDC. The DAQ system determines which SeGA detectors have above-threshold events by first reading out the TDC module, and then reading out the central contact and segment ADC modules for the SeGA detectors that have sent stop signals to the TDC.

Time-to-Digital Converter (TDC) module that was started by the master trigger. The TDC spectra were 800 ns wide and were used to discriminate the germanium spectra in time, to correct for random coincidences. The central contact energy signals for each SeGA detector that registered a γ-ray hit were digitized using Ortec 413 CAMAC 8k Analog-to-Digital Converters (ADCs). The segment energy signals were shaped using NSCL-built shaping amplifiers and digitized with Philips 7164 CAMAC ADCs.

3.6.2 Phoswich and PIN Detector Electronics

The phoswich detector electronics were presented in § 3.4.2, and the same electronics arrangement shown in Fig. 3.13 was used during the TF g-factor measurements. The trigger condition was a coincidence between the phoswich detector and the Ge array, in order for the SeGA electronics only to be read out when both a γ ray and an associated beam particle were present. The phoswich subsystem provided the particle trigger signal that was one half of the coincidence logic shown in Fig. 3.20. The dynode signal of the phoswich was inverted by a fast amp and then discriminated using a TC-455 CFD. The CFD output signal opened a 300 ns gate called PARTICLE with which an OR of the SeGA CFD signals called GE–OR could satisfy a logical AND condition. The result of the AND gate, GE–OR-*and*-PARTICLE, was a 340 ns wide gate that could overlap in time with a 40 ns-wide DELAYED–PARTICLE gate that occurred at the end of the 300 ns PARTICLE gate. The logical AND of the DELAYED–PARTICLE gate and the GE–OR-*and*-PARTICLE was the master trigger for the DAQ system. The timing of the trigger was with respect to the particle, regardless of the timing behavior of the germanium detectors, which was still preserved in the TDC spectrum for each SeGA detector.

During the beam tuning, a 488 μm silicon PIN detector was used to diagnose the secondary fragments using a ΔE–TOF method. The PIN was located in the N3 vault near the target position, as will be described in § 3.7, and was retracted from the beam line during the TF measurements. During the beam tuning time, the DAQ trigger was changed to PIN singles OR downscaled phoswich singles, and the PIN signal was shaped and amplified by an NSCL Quad Shaper and digitized using a CAEN V785 VME Peak-Sensing ADC.

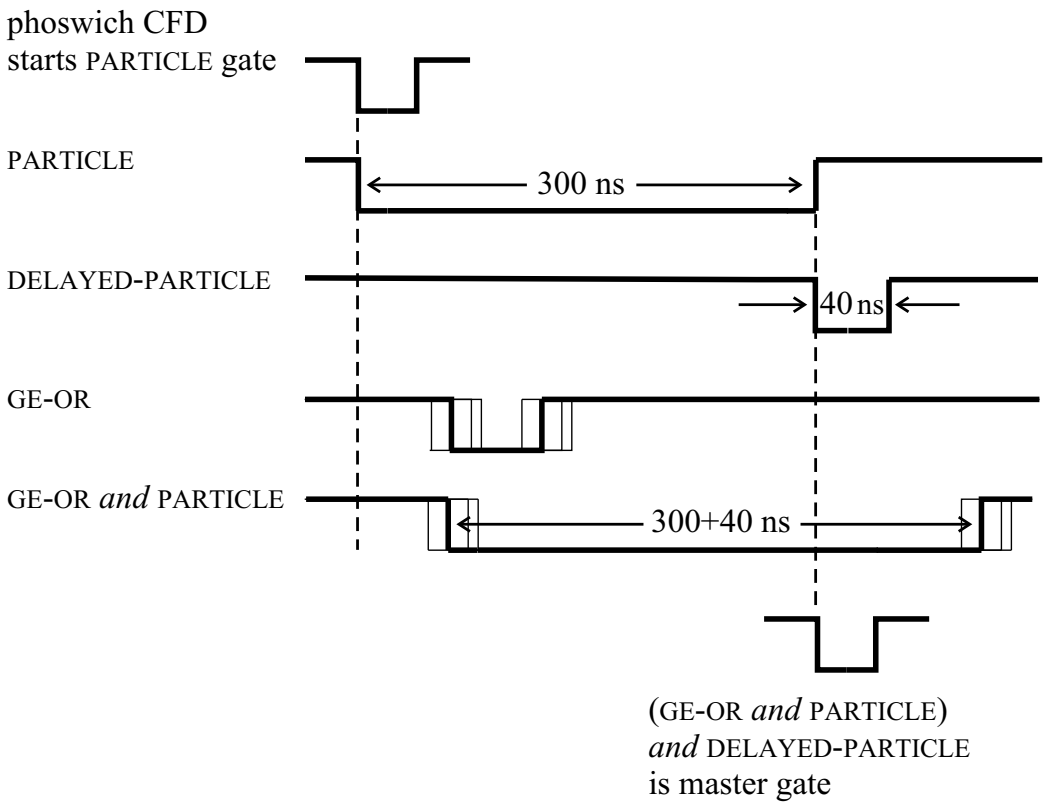

Figure 3.20: Trigger logic used in the experiment. The phoswich CFD signal started a 300 ns gate (PARTICLE) and a 40 ns gate that started at the end of the particle gate called DELAYED–PARTICLE. The logical OR of the SeGA CFD signals (GE–OR) started a 340 ns gate (GE–OR-*and*-PARTICLE) if it overlapped with the PARTICLE gate, and the logical AND of this gate with the DELAYED–PARTICLE gate created a master trigger that was correlated with the phoswich timing, avoiding any jitter in the germanium timing.

3.6.3 Magnet Interface to Datastream

In order to embed the status of the magnetic field direction in the datastream for analysis, the magnet control script running in the control system VME crate controlled coils in the Modicon/PLC to send high or low logic signals (0 V and 24 V) to the data acquisition system. A system of three signals were used, two for the electromagnet polarity and one for the swapping status. Prior to the polarity swapping, the "swap" signal was set to true, and it remained true for a small delay after swapping to ensure the magnetic field of the electromagnet had completely reversed before the swap was considered finished. The three signals needed to be interfaced into the DAQ system to be recorded as bits in the datastream (1=true, 0=false), and a hardware interface was built to electrically isolate the three signals to avoid noise from the control system and to adapt the 24 V control signals to the CAEN V262 VME I/O Module used in the DAQ system. The interface module consisted of mechanical relays that would open or close current sources with the proper impedances to produce NIM logic signals.

3.6.4 Data Acquisition Software

The software used for data acquisition was the NSCLDAQ Production Readout software, which provides a framework for the integration of distinct data acquisition subsystems into one coherent DAQ system. The SeGA electronics and data acquisition code had been developed for previous experiments with SeGA coupled to the S800 spectrograph, in the framework of Classic Readout, an older version of the DAQ software. The readout system for the phoswich detector was written as an event segment within Production Readout, and the older SeGA Readout software was decoupled from the S800 and formed into another event segment for Production Readout, using a functionality that encapsulates older software to make it compatible with Production Readout. The two separate subsystems (phoswich and SeGA) were then combined, along with the magnet status flags, into one datastream structure.

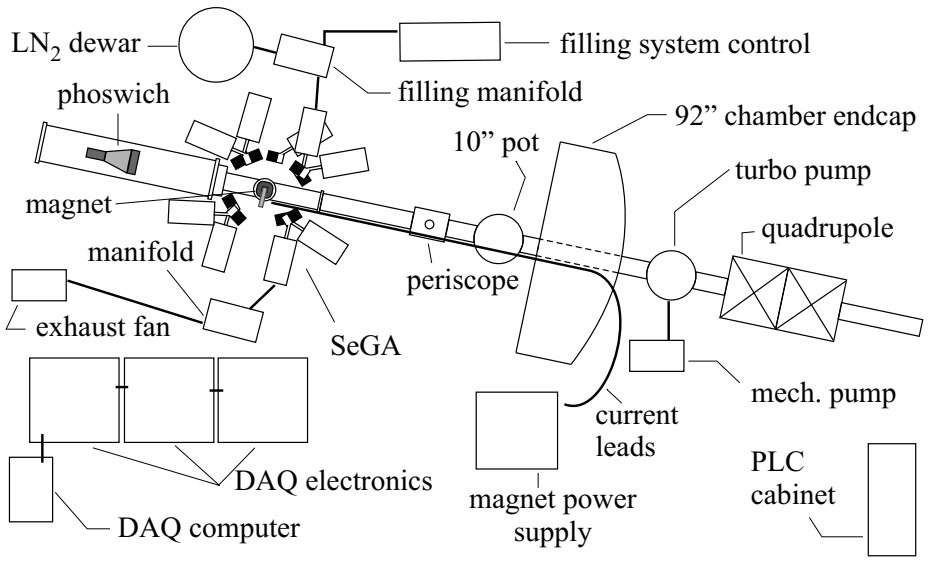

Figure 3.21: Arrangement of equipment in the N3 vault. The existing control system interface via the PLC cabinet was used to control the magnet power supply and interface with the DAQ electronics. The building liquid nitrogen supply was used to fill the Ge detectors after first accumulating in a large dewar. Data acquisition was run using electronics inside the vault, and data were recorded onto disks via an ethernet connection.

3.7 Layout in N3 Vault

The layout in N3 is shown in Fig. 3.21, which shows the components used in the experiment. The beamline was aligned using an optical reticule mounted on the entrance flange inside the 92" chamber, as well as a target permanently fixed to the wall inside the N3 vault beamdump to define the beam axis. An in-place 92" chamber mechanical roughing pump was used to back a 900 liter/s Alcatel 5900 turbomolecular pump that was installed on the bottom of the 92" chamber entrance pot to provide pumping for the entire experimental beamline beyond a gate valve located after the quadrupole doublet inside the N3 vault. The system could provide vacuum better than 10^{-5} torr, necessary to ensure the slowed projectiles did not scatter on their 80 cm flight path between the target and phoswich.

A 10" pot was installed upstream of the target position. The pot contained a 5"-thick copper beamstop on which a phosphorescent paint was applied. The beam-

stop could be remotely raised to stop the beam, and a CCD camera could view the beamspot for tuning. The Si PIN diode was installed in the pot and raised into the beam for tuning, and to measure the transmission from the A1900 to the N3 vault. In addition, the PIN could be used to estimate the transmission through the HVTF target, by comparing counts in the PIN to counts in the phoswich with the PIN lowered out of the beam. At the entrance to the pot, a collimator was installed in order to prevent a beam halo from hitting the target frame or electromagnet pole tips. The collimator consisted of a thick plate of tungsten with a 1" diameter hole drilled in the center.

Downstream of the 10" pot, a section of beampipe containing a periscopic mirror was used to view the target position. A phosphor-coated aluminum plate on a circular target frame was inserted in the horizontal section of the target chamber upstream of the target position, to serve as a target viewer during beam tuning. Since the vacuum needed to be broken to insert the viewer and also to remove the viewer after tuning, it consumed some time during the experiment, and was only used once for the ^{38}S run and once for the ^{40}S run.

The SeGA stand was clamped to a translation stage that was bolted to the vault floor just downstream of the 92" chamber rails. Two optical targets were held in place on the SeGA stand using aluminum alignment bars that were built for that purpose. The same alignment bars were used when the stand was first completed to hold the targets for measurements that located the SeGA detectors with respect to the targets by means of a theodolite system (this formed the database of detector coordinates used for the Doppler correction, which is discussed in §4.2.2). The translation stage could move the entire stand (with respect to the beam axis) up, down, left, right, forward, and backward, but it could not rotate about the vertical axis, the beam axis, or the axis perpendicular to the two. In order to rotate the stand about the vertical, the clamps holding it to the translation stage were loosened and the stand was manually rotated. Rotations about other axes could be accomplished by inserting

shims beneath the stand in order to level it, but by measuring with a mechanical level this was seen to be unnecessary because the stand was level.

A 4" beampipe cross design was chosen for the target chamber. The 4" cross was purchased and the necessary modifications were made by the NSCL machine shop. The target chamber is shown in Fig. 3.22. The target chamber downstream pipe was stepped to a 6" diameter as soon as possible after exiting the array, in order to provide an opening angle of $\sim 9.5^\circ$ for scattered beam particles. Below this angle, essentially all of the Rutherford cross section is contained, ensuring that a negligible fraction ($\sim 10^{-5}$) of the beam particles would stop near the array. The 6" diameter section is welded to an adapter flange for connecting to an 8" beampipe that holds the phoswich detector downstream of the array. The vertical section of the 4" cross was used to hold the electromagnet. The chamber was designed to allow the electromagnet coils and return yoke to be located outside of the vacuum. In order for the magnet pole tips to enter the vacuum of the target chamber, a "magnetic feedthrough" rather than a "physical feedthrough" was used. The top and bottom target chamber flanges

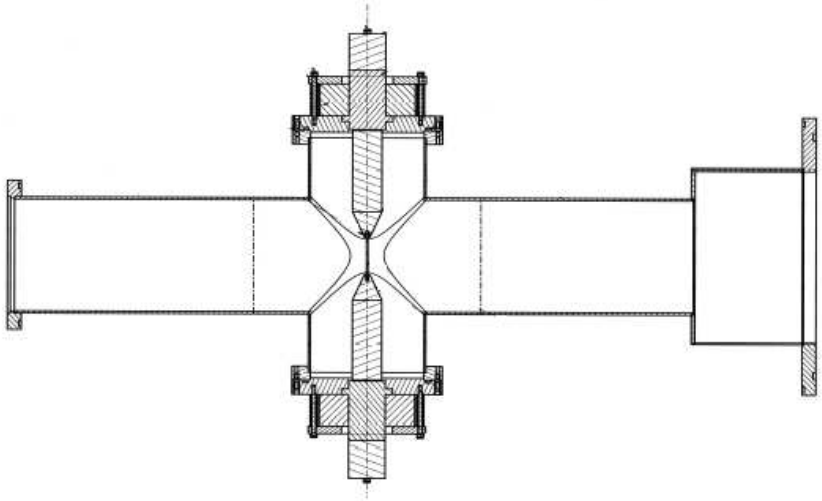

Figure 3.22: Cross section of the HVTF target chamber, with the beam entering from the left. The target is held in a target frame between the pole tips. The magnet yoke is separated into a piece that attaches inside the vacuum chamber and a piece that attaches to the outside of the chamber. The magnet coils are located outside of the vacuum.

were machined very thin (on both the outside and the vacuum side) in a 1 in^2 region to match the yoke area. On the outside of the flange, the vertical magnet yoke piece was attached with screws, and the magnet coil fit snugly around it, held in place by the horizontal yoke piece. On the vacuum side of the chamber flanges, the magnet pole tips were attached with screws. In this manner, the magnetic field carried by the iron yoke could "jump" across the thinly machined section of the flange without the need for an actual vacuum feedthrough. The cross section of the target chamber, in Fig. 3.22, shows the internal arrangement of the target chamber.

An 8" beampipe, attached to the exit of the target chamber, was the final section of beampipe and housed the phoswich detector. The phoswich signals were brought out of the vacuum using a feedthrough plate that was insulated from the beamline.

Chapter 4

Results and Conclusions

A separate run was performed for each sulfur isotope. For each secondary beam, phoswich-γ coincidences as well as downscaled phoswich events were recorded, during which the electromagnet ran at 4.5 amps (1.1 kG near the pole tips), switching polarity every 600 s. Data were collected for 81 hours for the ^{38}S fragments and 68 hours for the ^{40}S fragments. This Chapter presents the data analysis and results of the two measurements.

4.1 Particle Identification

Secondary beam particle identification was performed using the A1900 focal plane detectors for energy loss and time-of-flight information, verifying that the dominant component of the beam was the desired sulfur isotope. When the ions were sent to the experimental endstation, γ rays from the radioactive decay of the projectiles (which stop in the phoswich detector) were used to confirm the particle ID. Known γ rays in ^{38}Cl and ^{38}Ar were observed during the ^{38}S run and γ rays in ^{40}Cl and ^{40}Ar were observed during the ^{40}S run. After implanting beam into the phoswich, the beamstop was inserted and the phoswich CFD threshold was raised in order to cut out triggers coming from radioactive decay of the beam particles. Those signals were much lower

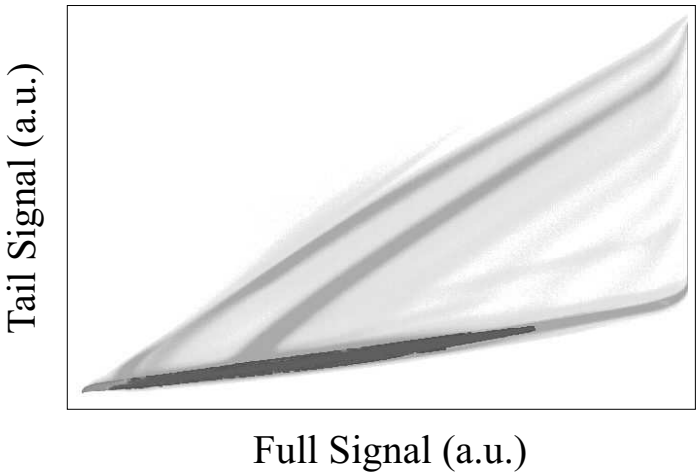

Figure 4.1: Phoswich tail signal vs. the full energy signal, with counts in a log scale indicated by grayscale shade. A lower-level threshold is used in this plot for better contrast. Most counts are for particles that only cause fast scintillation (the darker band with low values of tail light). Particles that punch through the fast plastic layer will show up away from the dark band with larger values of tail light.

in energy than the beam particles, but it was desirable to remove them as a source of random particle-γ coincidences.

4.2 γ-ray Sorting

Particle-γ coincidences were recorded, and both lab-frame and Doppler-corrected spectra were obtained. Particle energy, time of flight, and SeGA TDC gates were used to produce true coincidence spectra that were corrected for random particle-γ coincidences, and Doppler correction was optimized for the γ rays emitted after the projectiles traversed the entire ferromagnet layer. The angular distribution of γ rays was analyzed and compared to the calculated angular distribution using the theory of Coulomb excitation, and the count rate changes upon magnetic field reversal were obtained for each of the six pairs of detectors at symmetric angles $\pm\theta$ with respect to the beam direction. Calculations were performed to determine the transient field strength B_{TF}, and $g(2^+)$ values were obtained for ^{38,40}S. The details of each step will be presented in this section.

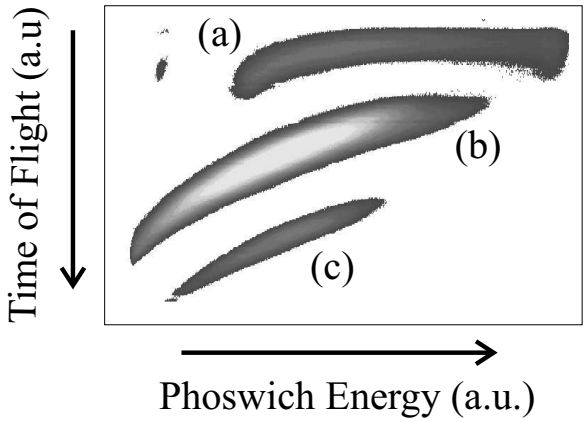

Figure 4.2: Time of flight between the cyclotron RF and the phoswich, versus phoswich energy, with counts shown in a log scale indicated by grayscale shade. A lower-level threshold is used in this plot for better contrast. The three main features are: (a) events triggering the slow plastic (light particles), (b) events having particle-γ coincidences primarily in the fast plastic only, and (c) downscaled particle singles (no particle-γ coincidence).

4.2.1 Phoswich, Time of Flight, and γ Time Cuts

A fast/slow 2D spectrum, shown in Fig. 4.1, was obtained by plotting the tail-integrated QDC channel versus the total-pulse integrated QDC channel. The dark band located along the "full signal" axis, corresponding to small "tail signal" values, are the sulfur projectiles. Any deviation from the heavy-ion band is caused by an increased proportion of slow scintillation light, indicating punch-through events that are caused by low-Z particles. In addition to the 2D fast/slow spectrum, the phoswich energy signal (the full pulse shape integration) was plotted versus the time-of-flight between the cyclotron RF and the phoswich pulse, to form a 2D E–TOF spectrum for the particles. Three distinct features are evident in the spectrum (a representative spectrum is shown in Fig. 4.2). By gating on different regions of the phoswich 2D fast/slow spectrum, it was established that the upper feature (labeled "a" in Fig. 4.2) corresponds to those events causing a large amount of slow scintillation in the phoswich, meaning that they are not heavy ions (those would stop in the thin fast plastic layer) but are light particles coming from nuclear reactions in the target or other material such as the Image 2 wedge. The middle region (labeled "b") cor-

responds to phoswich events triggered by sulfur projectiles that are in coincidence with γ rays, and the lower region (labeled "c") is made up of downscaled phoswich events (the downscaler module introduces an additional delay that shifts this group of events away from the phoswich-γ coincidences).

The germanium spectra were produced by gating on the sulfur region of the phoswich 2D fast/slow spectrum and the particle-γ coincidence region of the phoswich-TOF 2D spectrum. The γ-ray spectra were corrected for random coincidences, beginning by projecting out the TDC spectra corresponding to particles in the 2D fast/slow and TOF spectra that came in coincidence with γ rays in the energy range 1000-1500 keV for ^{38}S runs and 700-1200 keV for ^{40}S runs. The ^{38}S TDC spectra are shown in Fig. 4.3, which includes the raw (ungated) TDC spectra superimposed with the phoswich- and energy-gated TDC spectra. For each SeGA detector, gates were placed around the prompt γ-ray peak in the TDC spectrum (shown as the filled channels in Fig. 4.3), and gates were placed to each side of the prompt peak, in order to produce germanium spectra with good coincidences and with random coincidences. Normalized random coincidence spectra were then subtracted from the coincidence spectra for the prompt region, yielding SeGA spectra that were analyzed to extract the count differences at each angle for magnetic field up and magnetic field down. Random-subtracted spectra were created for both the lab-frame and the Doppler-corrected spectra. Separate spectra were created for magnetic field up and magnetic field down data; these spectra could be added together to obtain an unperturbed angular distribution since the precession angle is small.

4.2.2 Principles of Doppler Correction

One of the principal challenges posed by in-beam γ-ray studies is the Doppler shift of the γ rays. For intermediate-energy beams, the Doppler shift is very pronounced. For a projectile with velocity $\beta = v/c$, a γ ray emitted at an angle θ with respect to

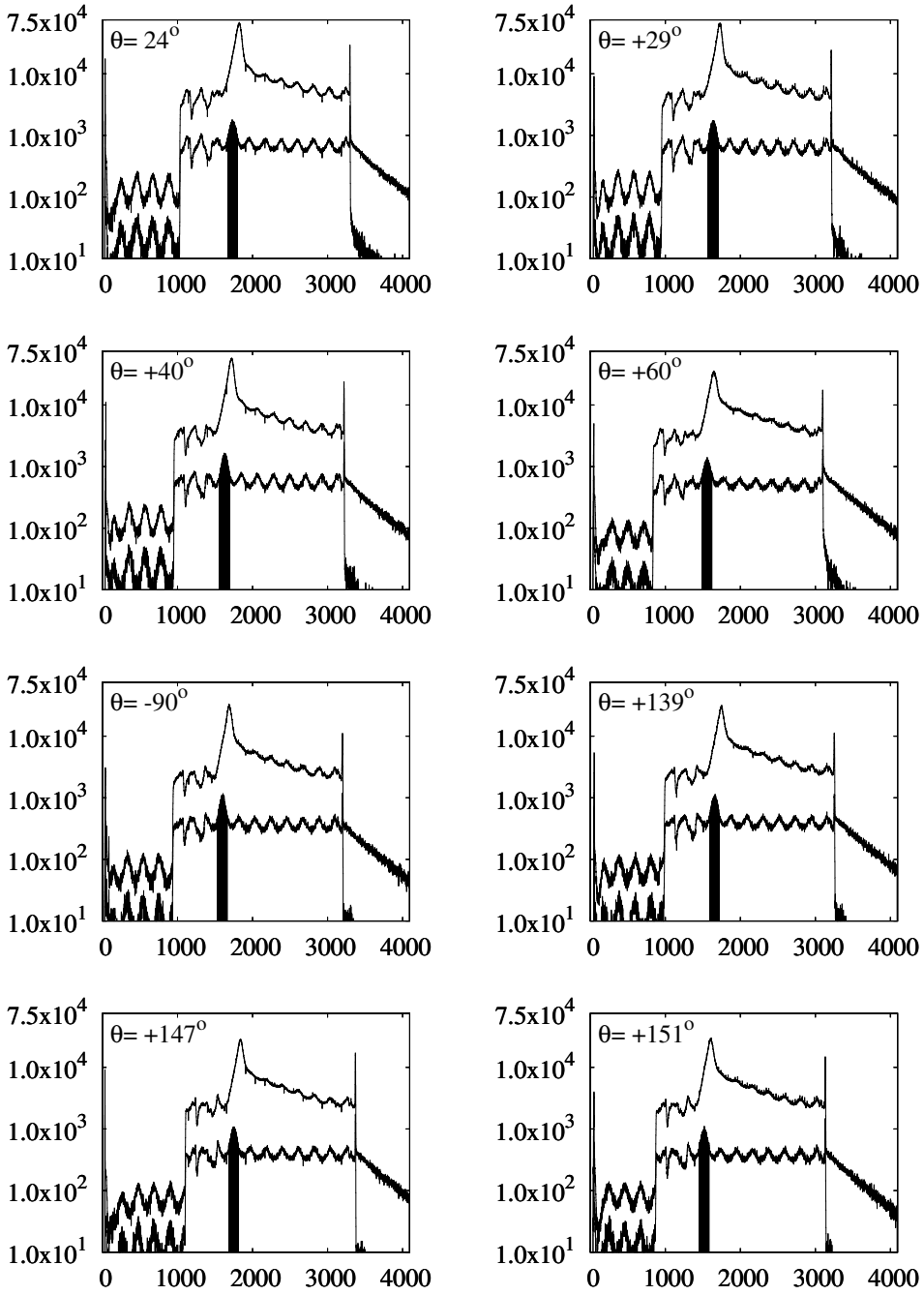

Figure 4.3: SeGA time spectra for ^{38}S showing the raw spectra (upper curves) and the resulting spectra when gated on the 2D phoswich heavy ion region, the phoswich-TOF good particle-γ coincidence region, and SeGA γ-ray energies between 1000 and 1600 keV (lower curves). The shaded region shows the channels used to make the prompt γ-ray TDC gate.

the projectile direction will have an energy

$$E_\gamma^{lab} = \frac{E_\gamma^{nuc}\sqrt{1-\beta^2}}{1-\beta\cos\theta}, \tag{4.1}$$

where E_γ^{nuc} is the energy of the γ ray in the rest frame of the projectile. Doppler correction is performed event-by-event on the detected γ-ray energy E_γ^{lab} in order to recover the "true" γ-ray energy. From Eqn. 4.1 it can be seen that the beam velocity β and the γ-ray emission angle θ are required. Since the projectiles only undergo small-angle scattering in intermediate-energy Coulomb excitation, the γ-ray emission angle can safely be measured with respect to the beam axis. In other words, the angle θ used in Eqn. 4.1 is the γ-ray *detection* angle measured with SeGA.

SeGA detectors give sub-crystal position resolution for the γ-ray interaction point in order to improve the Doppler correction over that of a conventional germanium detector. For γ rays with an energy of $\sim$ 1 MeV, the primary type of interaction in germanium is Compton scattering with a mean free path of 3 cm as calculated from the germanium mass attenuation coefficient [117]. Since the crystal size is larger than the mean free path, it is possible that more than one interaction will occur within the crystal, and hits might be recorded in more than one segment. A method to assign the "first hit" segment and therefore choose the corresponding angle to use in the Doppler correction formula must be implemented. The method used to choose the first-hit segment for the SeGA detectors was the following empirically-justified procedure: the segment with the highest energy signal is selected to be the first-hit if the total γ-ray energy is above 500 keV, and for γ rays below 500 keV total energy, the lowest-energy segment is chosen.

In Compton scattering, a photon imparts some of its energy to an electron and then continues traveling through the material (perhaps leaving the material if the interaction occurs near a boundary edge). The electron and lower-energy photon leave the scattering site with an angle between them that governs how much energy

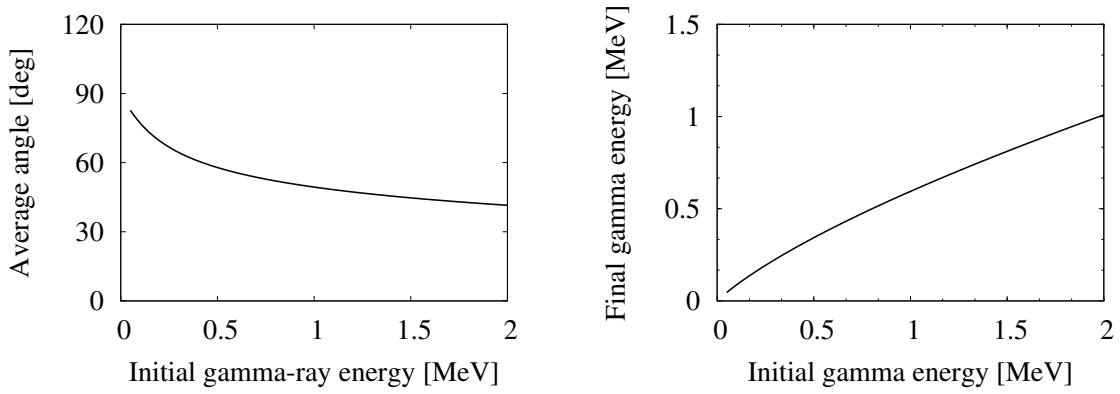

Figure 4.4: Klein-Nishina differential cross section for the Compton scattering of 1 MeV γ rays (left), and the final γ-ray energy as a function of incoming γ-ray energy for Compton scattering at the energy-dependent average scattering angle (right).

is transferred from the photon to the electron. The relationship between the Compton scattering angle θ_C and the outgoing photon energy can be written as

$$E_f = \frac{E_i}{1 + (E_i/m_e c^2)(1 - \cos\theta_C)}, \tag{4.2}$$

where $E_{i,f}$ are the initial and final photon energies and m_e is the electron mass. The angle- and energy-dependent cross section for Compton scattering is called the Klein-Nishina equation [118]:

$$\frac{d\sigma}{d\Omega} = \frac{r_0^2}{2}\frac{E_f^2}{E_i^2}\left(\frac{E_i}{E_f} + \frac{E_f}{E_i} - \sin^2\theta_C\right), \tag{4.3}$$

where $r_0 = e^2/m_e c^2$ is the classical radius of the electron, and θ_C is the usual angle between the initial and final photon directions. Inserting 4.2 into 4.3, one obtains the scattering cross section as a function of θ, shown on the left side of Fig. 4.4, for 1 MeV γ rays. For Compton scattering at the average θ_C for a given incoming photon energy E_i, which can be calculated using Eqn. 4.3, the final photon energy is plotted in Fig. 4.4. On average, an incoming γ ray will deposit most of its energy in the first interaction, at least for γ rays of more than $\gtrsim$500 keV. Another interaction becomes

likely for a photon with an energy less than 500 keV as it travels through germanium, and that is absorption through the *photoelectric effect.* Since a photoelectric absorption is the most likely event for the lower-energy γ rays, resulting in the disappearance of the γ ray and all of its energy deposited in the segment containing the interaction, it is not as likely that the highest-energy segment results from Compton scattering.

Following the assignment of the first-hit segment, the angle θ in Eqn. 4.1 can be calculated based on the known coordinates of the segment with respect to the target position. The detection angle as well as the beam velocity β are used in Eqn. 4.1 to perform the Doppler correction. The angular width of a segment, which is 1 cm wide and located 21 cm from the target, is $\sim 2.7^{\circ}$. The effect of this angular uncertainty $\Delta\theta$ and any uncertainty in the beam velocity $\Delta\beta$ on the width of the Doppler-corrected γ-ray peak can be seen by partial differentiation of Eqn. 4.1 with respect to θ and β, yielding

$$\begin{aligned}\left(\frac{\Delta E_\gamma}{E_\gamma}\right)^2 = \quad & \left(\frac{\beta \sin\theta}{1-\beta\cos\theta}\right)^2 (\Delta\theta)^2 \\ & + \left(\frac{\cos\theta-\beta}{(1-\beta^2)(1-\beta\cos\theta)}\right)^2 (\Delta\beta)^2 \\ & + \left(\frac{\Delta E_{Ge}}{E_\gamma}\right)^2,\end{aligned} \tag{4.4}$$

where a term accounting for the intrinsic energy resolution of the germanium has been added. As was pointed out by Glasmacher [119], the relative width of the Doppler-corrected peak scales directly with the uncertainties $\Delta\theta$ and $\Delta\beta$ and not with the γ-ray energy. For the case of the ^{38,40}S measurements presented here, the particle velocity ranges from $\beta \sim 0.28$ at the front of the target to $\beta \sim 0.08$ at the back of the target. The $\Delta\beta$ of 0.2 means that the $\Delta\beta$ term in Eqn. 4.4 will be the dominating term if a constant β value is used for the Doppler correction. In the usual intermediate-energy Coulomb excitation studies, there is not a large change in velocity through the target and the use of a constant β such as the mid-target velocity is acceptable. In the

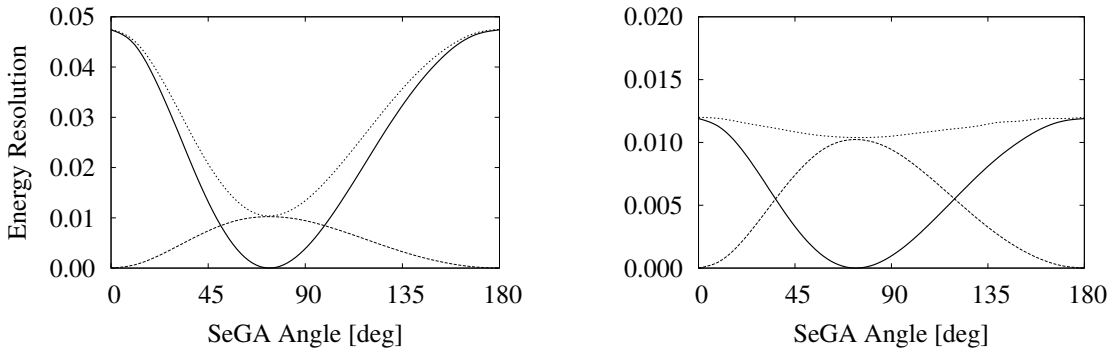

Figure 4.5: Square of the fractional energy resolution using Eqn. 4.4 with $\Delta\theta = 10°$ for two different $\Delta\beta$ values: $\Delta\beta = 0.2$ (left) and $\Delta\beta = 0.1$ (right), where the solid line represents the term in Eqn. 4.4 involving $\Delta\beta$, and the other two curves are the $\Delta\theta$ term and the total.

HVTF case, the impact on $(\Delta E/E)^2$ due to two values of $\Delta\beta$ is displayed in Fig. 4.5. The panel on the left represents the actual case if a single beta is used, and the panel on the right represents a factor of two decrease in $\Delta\beta$ to get $\Delta\beta = 0.1$, where it is apparent that the $\Delta\theta$ and $\Delta\beta$ terms are on equal footing. In the present context, the long Doppler tail that results from the emission of γ rays during the slowing-down process is not the feature of interest, as will be discussed further. Instead, the portion of the spectrum resulting from γ-ray emission after the projectiles have left the target is more important, and the Doppler correction was performed using a β determined event-by-event, in order to optimize the reconstruction of the in-vacuum flight peak.

Event-by-event Doppler correction was performed by using the SeGA first-hit segment positions and the after-target particle velocities determined from a transformation of the phoswich energy signals into velocities. The event-by-event β values resulted in an improved Doppler correction that was optimized for the γ rays emitted after the projectile experienced the full transient field. The average after-target velocities were extracted using the lab-frame centroids of the Doppler-shifted projectile 2^+ γ-ray peaks. The Doppler shift formula for γ rays emitted in flight,

$$E_0 = \gamma E_{lab}\,(1 - \beta\,\cos\theta), \tag{4.5}$$

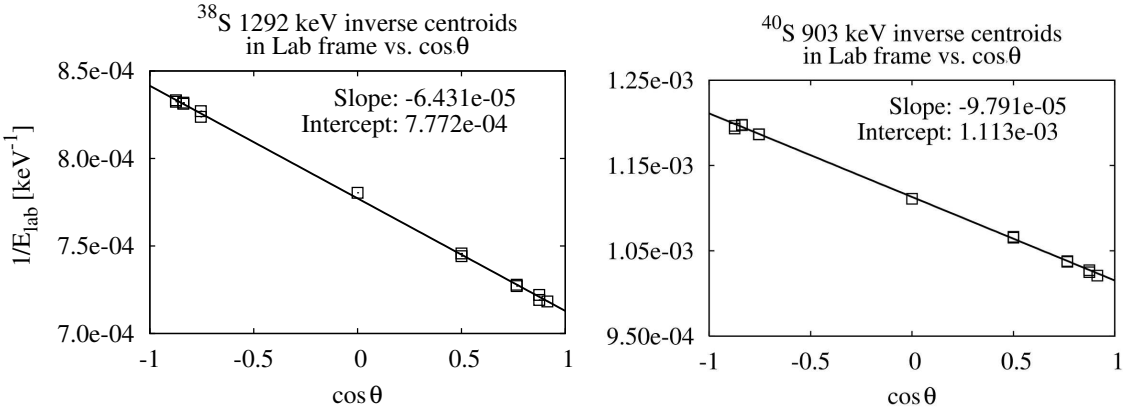

Figure 4.6: Inverse peak centroids versus $\cos\theta$ for ^{38}S (left) and ^{40}S (right) γ rays in the lab frame, with the slopes and intercepts obtained by a linear fit to the data shown in the plots. The average after-target velocities are the ratios of the slopes and intercepts (see text).

was used to determine the average β of the moving source, since the γ-ray energy was measured at different angles. Solving Eqn. 4.5 for E_{lab} and inverting both sides of the equation gives

$$\frac{1}{E_{lab}} = \frac{\gamma - \gamma\beta\cos\theta}{E_0} = \frac{\gamma}{E_0} - \frac{\gamma\beta\cos\theta}{E_0}. \tag{4.6}$$

It can be seen that a plot of $1/E_{lab}$ versus $\cos\theta$ will be a line of slope $-\beta\gamma/E_0$ with an intercept at γ/E_0; the quotient of those two quantities is the beam velocity β. Fig. 4.6 shows the results of a least-squares fit to the inverse centroids in the lab frame versus $\cos\theta$ for ^{38}S and ^{40}S.

The values of β extracted from the fits are $\beta^{38} = 0.083(1)$ and $\beta^{40} = 0.088(1)$, where the quoted errors are 30% larger than those given by the errors of the fit parameters. The β^{38} and β^{40} values were used to fix the average velocity after the transformation from phoswich energy channel to β value. The velocity distribution was assumed to have a $\sqrt{E}$ functional form, and it remained to choose scaling factors that would result in a realistic velocity distribution (*i.e.*, ensure that low phoswich channels did not give $\beta \to 0$). From the phoswich energy-TOF plot, the kinematical

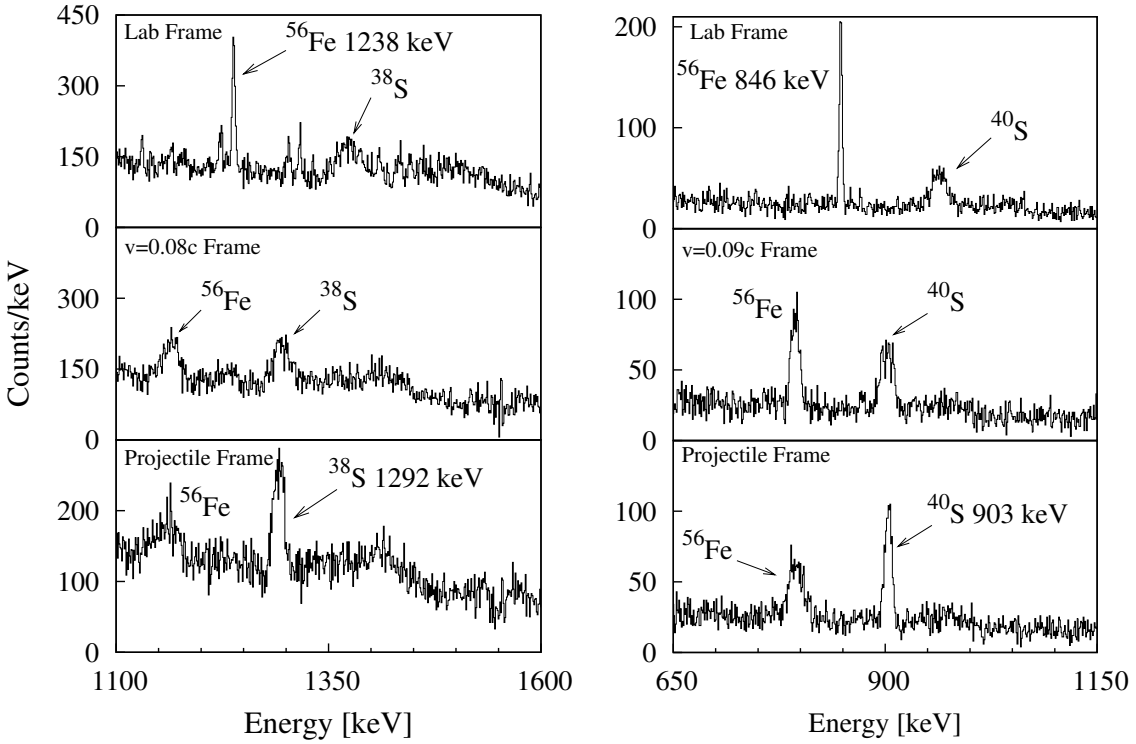

Figure 4.7: Laboratory frame (top), single-β Doppler corrected (middle), and event-by-event Doppler corrected spectra (bottom) for ^{38}S (left) and ^{40}S (right) at $\theta = 40°$. The bottom spectrum is optimized for decays occurring in vacuum by detecting the kinetic energy of the particle in the phoswich detector and using that velocity as the value of β in Eqn. 4.5.

curve of the particle distribution was analyzed to extract the scaling factors for use in the following transformation,

$$\beta_{phos} = A\sqrt{\frac{E_{phos} + B}{C}}, \tag{4.7}$$

where E_{phos} is the channel number of the phoswich full-energy signal and A, B, and C are constants chosen to produce resulting velocity distributions that had the proper average velocities and minima and maxima of β $\sim$0.05 and 0.12. In order to check that the velocity distribution used for the Doppler correction was correct, additional data were taken at the end of the experiment with the phoswich position shifted by $\pm$15 cm. The change in time of flight was measured, confirming that the adopted projectile velocity distribution was correct. Examples of Doppler-corrected γ-ray spectra are shown in Fig. 4.7, and the difference between using a single value of β and using a β determined event-by-event is clearly seen.

4.2.3 Angular Distribution of γ Rays

Gamma-ray peak areas were obtained at each angle by integrating the counts in the Ge spectra between limits set close to the high and low side of the 2^+ peaks, and subtracting counts summed in background regions on the low and high energy sides of the peak, normalized to the widths of the summing regions. For integrating the counts in the magnet up/down spectra, the summation limits were set using the summed up+down spectra in order to ensure that no bias was introduced for the up and down counting results, since the precession was deduced by comparing the counts in the up versus the down spectra.

The angular distributions of the 1292 keV ^{38}S γ rays and the 903 keV ^{40}S γ rays are shown in Fig. 4.8. The angular distribution has been transformed into the projectile frame by correcting the number of counts for the Lorentz boost of the solid angle and for the angle transformation between the laboratory and projectile frames. The

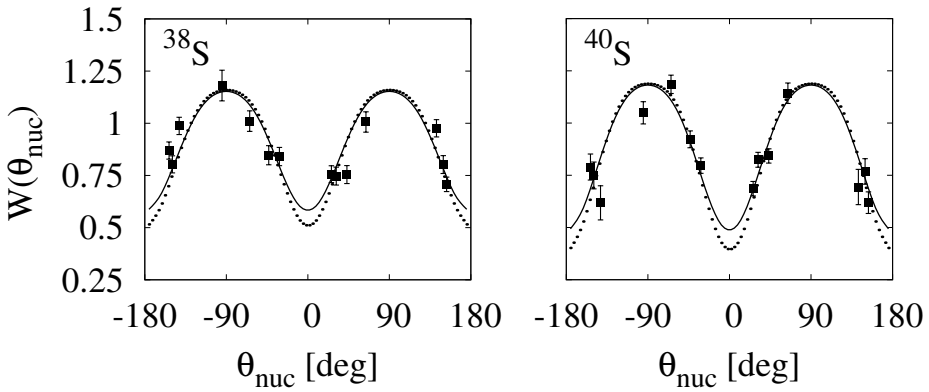

Figure 4.8: Angular correlation of ^{38}S (left) and ^{40}S (right) γ rays. The solid (dotted) line shows the calculated angular correlation in the frame of the projectile nucleus including (not including) the effect of vacuum deorientation. The SeGA angles have been transformed into the projectile frame.

former effect is more important, and can be expressed as [56]

$$d\Omega_{lab} = \frac{1-\beta^2}{(1+\beta\cos\theta_{nuc})^2}\, d\Omega_{nuc}, \tag{4.8}$$

with the resulting angular distribution transformed as

$$W_{nuc}(\theta_{nuc}) = W_{lab}(\theta_{lab})\frac{d\Omega_{lab}}{d\Omega_{nuc}}. \tag{4.9}$$

The transformation needed to obtain the SeGA angles in the projectile frame is [120]

$$\cos\theta_{nuc} = \frac{\beta - \cos\theta_{lab}}{\beta\cos\theta_{lab} - 1}. \tag{4.10}$$

The solid lines in Fig. 4.8 are calculations of the angular distributions using the program GKINT [107]. GKINT divides the target layers into thin slices and uses the stopping powers of Ziegler and coworkers [99] to compute the kinetic energy as a function of depth using a Runge-Kutta routine. Using the theory of Coulomb excitation [121], excitation cross sections in each slice are obtained by integrating over the phoswich scattering angle acceptance, and the kinetic energy of the particles emerging

from the target is calculated as a function of excitation depth. The flight time from excitation to target exit is used to determine the number of γ rays emitted during target transit and in vacuum, using the 2^+ lifetimes. The in-vacuum emission rates are used to create weighted-average values for the angular distribution coefficients ($a2$ and $a4$) that are detected in the vacuum-flight peaks, including the effects of vacuum deorientation, which will be described in the next section. For ^{38}S, the values $a_2 = -0.3596$ and $a_4 = -0.0597$ were obtained, and for ^{40}S, the values $a_2 = -0.3850$ and $a_4 = -0.0653$ were obtained. Good agreement can be seen between the calculated angular distribution and the measured values, and it is important to note that the solid line is not a fit to the data except for the overall scaling.

4.2.4 Vacuum Deorientation

The ^{38}S and ^{40}S γ-ray peaks at 1292 keV and 903 keV in the Doppler-corrected spectra appear sharp because those γ rays were emitted by nuclei in flight through vacuum after leaving the target, rather than during the slowing down process. Once an ion exits the target, its velocity does not change until it is detected in the phoswich. Therefore, the velocity detected in the phoswich detector will correspond to the ion velocity at which the γ ray was emitted, and those γ rays will be Doppler corrected to the true transition energy. It is advantageous from the point of view of HVTF g-factor measurements to have a long-lived excited state (i.e., several picoseconds) for which a large fraction of decays occur after the ion leaves the target. However, from LISE calculations as well as explicit charge-state measurements undertaken at ANU [122], it was established that the sulfur ions were carrying 1-3 electrons upon emerging from iron at velocities near Zv_0. Therefore, recoil-in-vacuum (RIV) effects needed to be examined to determine the extent of their impact on the g-factor measurement.

Recoil-in-vacuum effects are interactions between the nucleus of an ion and the atomic electrons. The dominant interaction between orbital electrons and the atomic nucleus is the magnetic dipole interaction between the nuclear magnetic moment and

the magnetic field created at the site of the nucleus by the ns electrons, with the $1s$ electron field (from Eqn. 2.31) being most significant since the fields for higher orbitals fall off with $1/n^3$. Additionally, it is important to note that only *unpaired* electrons have a magnetic field contribution at the site of the nucleus, because the fields from paired electrons cancel each other. Therefore, RIV effects are most important for hydrogen- and lithium-like ions, which is most likely the situation for projectiles in the HVTF regime or in any other scenario where projectiles are slowed to $v \approx Zv_0$. The nuclear angular momentum I and the electronic angular momentum J will couple to a total angular momentum $F = I + J$, which is the conserved quantity for the free ions recoiling through vacuum. The nuclear and electronic spins will precess about F, and this serves to deorient the nuclear spins from their initial orientation in Coulomb excitation. While traversing a solid material, the ion-electron collision times are so fast that electrons are constantly hopping on and off the nucleus. This means that no spin precession can occur about the vector F because each new electron also has a randomly-oriented spin direction. Upon emerging from material into vacuum, however, an ion left with a few electrons attached quickly reaches its electronic ground state. The static electronic configuration has a unique orientation for J, and hence RIV effects can happen.

The deorientation is experimentally observed through an *attenuation* of the angular distribution, which is manifested by a reduction of the angular distribution parameters a_2 and a_4 in a specific way. The reduction parameters, called attenuation coefficients, are denoted G_2 and G_4. Goldring [59] discussed these attenuation coefficients for a variety of scenarios, depending on the state of ionization of the ions, by calculating the interaction between the nuclear g factor and the magnetic fields created by the atomic electrons, which can be a complicated configuration. The 'cold ionization' scenario, where the ions are carrying only a few electrons, applies to

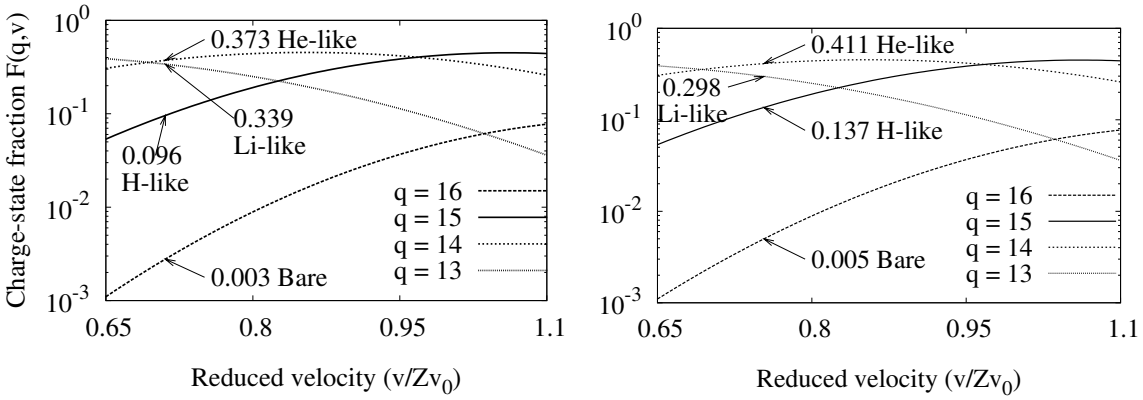

Figure 4.9: Charge-state fractions for sulfur projectiles exiting iron foils near the sulfur K-shell electron velocity, measured at the ANU 14UD Pelletron [122]. The velocity 0.083 c is marked on the left, corresponding to the ^{38}S ions, and the velocity 0.088 c is marked on the right panel, corresponding to the ^{40}S ions.

high-velocity ions recoiling into vacuum. The attenuation coefficients in this case are

$$G_k(\omega\tau) = 1 - \frac{k(k+1)}{(2I_i+1)^2}\frac{(\omega\tau)^2}{1+(\omega\tau)^2}, \tag{4.11}$$

and they depend on the lifetime of the excited state (τ), and the Larmor frequency (ω) for the free-ion hyperfine field. Since the hydrogen- and lithium-like hyperfine fields are so large, $\omega\tau$ approaches infinity and the attenuation reaches a "hard core" value of

$$G_k(\omega\tau \to \infty) = 1 - \frac{k(k+1)}{(2I_i+1)^2} \equiv 1 - b_k. \tag{4.12}$$

The actual attenuation for the angular distribution will depend on the fraction of ions in the hydrogen- and lithium-like states, which depends on the velocity with which the ions leave the target material, the ion atomic number Z, and the target material itself. A measurement of the charge state distribution of sulfur ions emerging out of iron foils at velocities near the sulfur K-shell electron velocity was undertaken at the ANU 14UD Pelletron [122]. Fits to the resulting charge state distributions are plotted in Fig. 4.9. The attenuation coefficients for an ensemble of nuclei in different

few-electron charge states can be written as

$$G_k = 1 - (Q_H + Q_{Li})b_k, \tag{4.13}$$

with the $I = 2$ values of $b_2 = 0.24$ and $b_4 = 0.8$. The measured charge-state fractions of $Q_H + Q_{Li} = 0.435$ yield attenuation coefficients $G_2 = 0.90$ and $G_4 = 0.65$. From the angular distribution plots in Fig. 4.8, it can be seen that the overall effect of these coefficients on the angular distributions are small; in fact, at the SeGA angles used in the TF measurements, there is no sensitivity to the RIV effects except for the slope changes they cause. The RIV effects calculated with the program GKINT were included in the a_2 and a_4 coefficients used to calculate the slope factors $S(\theta)$, and uncertainties of 10% were assigned to the S factors.

4.3 Transient Field Effect

The transient field effect is observed through the Larmor precession of the angular distribution. The total precession angle can be small due to the short interaction time with the transient field. Therefore, an established analysis method using ratios of counts in the germanium detectors is employed [51], rather than fits to the perturbed angular distribution. In the following subsections the details of the transient field effect are given, including the extracted $g(2^+)$ values of ^{38,40}S.

4.3.1 Experimental Spin Precession

The precession angle $\Delta\theta$ was extracted from the measured change in the angular distribution for the two magnetic field directions, using the procedure described in § 2.1.3. The logarithmic slopes of the γ ray angular distribution $W(\theta)$ were evaluated at the SeGA angles θ *in the frame of the projectile* due to Lorentz effects. The Lorentz boost of the γ ray angular distribution does not affect the experimental precession

effect ϵ, since the factors $d\Omega_{lab}/d\Omega_{nuc}$ that affect $N(\theta)$ will cancel in the double ratio ρ. However, the spin precession occurs in the projectile frame, and it should be noted that the SeGA observation angles in the laboratory frame are not located at the same angles in the projectile frame. Therefore, the slope factors were evaluated at the projectile-frame SeGA angles, obtained by transforming the SeGA angles according to Eqn. 4.10, when calculating ϵ/S. The S factors are shown in Table 4.1, along with the extracted spin precessions for each angle pair.

4.3.2 Evaluation of Transient Field

The transient field strength was evaluated with the program GKINT using the ANU HVTF parametrization described in Chapter 2, and the experimental incoming beam energies. The kinematical calculations, performed to obtain γ-ray angular distributions weighted by excitation depth in the target and exponential decay in time, also resulted in the knowledge of particle velocity profiles through the target. The particle velocity profiles were integrated through the target (from the velocity at excitation, to the velocity upon exiting the target) and the transient field interaction was calculated using the TF parametrization. The particles statistically emit de-excitation γ rays, which carry the information of the transient field interaction up until the time of γ-ray emission. Therefore, the Doppler shifts of the γ rays, which are essentially measures of the particle depths within the target at the times of emission, reveal a lineshape-dependent spin precession, in principle. The lineshape dependence is due to the different respective transient-field interaction times for particles that emit γ rays at different depths in the target. The particles that emit γ rays after leaving the target have the longest transient-field interaction time and therefore the largest spin precession, $\Delta\theta$, which is deduced by analyzing the γ rays in the vacuum flight peak. Therefore, the spin precession per unit g factor, $\Delta\theta/g$, was evaluated in GKINT for decays occurring in vacuum.

Results of the GKINT calculations are shown in Table 4.2. Spin precessions per

Table 4.1: Precession results obtained for each angle pair from the double ratios ρ and ϵ, and the slope factors S.

detectors		^{38}S			^{40}S		
θ°	ϕ°	ϵ	S	$\Delta\theta$ [mrad]	ϵ	S	$\Delta\theta$ [mrad]
$\pm$29	90	-50(20)	+0.79(8)	-64(27)	-17(35)	+0.86(9)	-20(41)
$\pm$151	90	+26(23)	-0.80(8)	-33(29)	-4(35)	-0.88(9)	+5(40)
$\pm$139	46	-10(23)	-0.54(5)	+19(43)	+7(28)	-0.58(6)	-12(48)
$\pm$147	143	-7(27)	-0.48(5)	+15(57)	-24(31)	-0.52(5)	+46(60)
$\pm$40	131	-41(19)	+0.50(5)	-83(39)	+26(32)	+0.53(5)	+49(60)
$\pm$60	61	-18(15)	+0.26(3)	-69(58)	+1(28)	+0.27(3)	+4(103)
average:				$-43(15)$			+5(21)

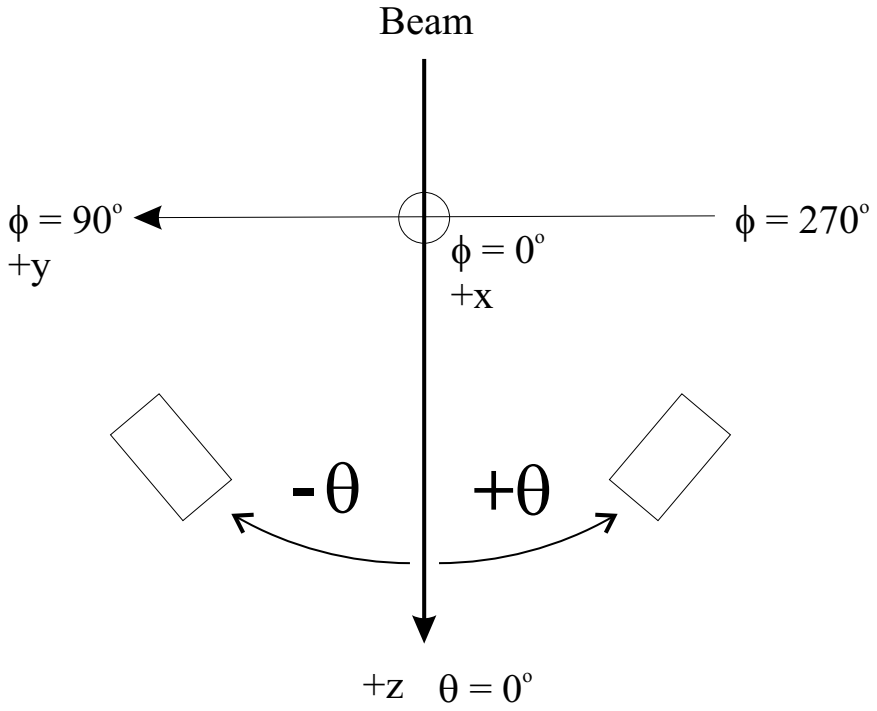

Figure 4.10: Sign convention used for pair of SeGA detectors at symmetric polar angles from the beam axis. When seen from above, positive θ is defined as increasing in a counterclockwise fashion from the downstream beam axis.

Table 4.2: Nuclear parameters and reaction kinematics. $\langle E_{i,e} \rangle$ and $\langle v_{i,e} \rangle$ are the ion kinetic energies and velocities at the entrance and exit of the iron layer. The effective transient-field interaction time t_{eff} and the spin precession per unit g factor, $\Delta\theta/g$, are evaluated for ions that decay after leaving the target. The ion entrance and exit velocities, t_{eff}, and $\Delta\theta/g$ were calculated with the program GKINT [107].

Isotope	$\tau(2_1^+)$ [ps]	$\langle E_i \rangle$ [MeV]	$\langle E_e \rangle$ [MeV]	$\langle v_i/Zv_0 \rangle$	$\langle v_e/Zv_0 \rangle$	t_{eff} [ps]	$\Delta\theta/g$ [mrad]
^{38}S	4.9	762	123	1.75	0.71	2.98	−330
^{40}S	21	782	145	1.73	0.75	2.99	−339

unit g factor, $\phi = \Delta\theta/g$, of -330 mrad for ^{38}S and -339 mrad for ^{40}S were obtained from the GKINT analysis for ions that decay after leaving the target. The effects of the parametrization and the γ-ray lineshape on the magnitude of $\Delta\theta/g$ are investigated in the following section.

Effects of B_{TF} Uncertainty and Doppler Tail Effects

The uncertainty due to the parametrization was investigated by applying a quenching factor to the $v > Zv_0$ region of the $B_{TF}(v)$ function, since it is the high-velocity side that does not have as much experimental verification as the low-velocity side, which was fit to a large number of experimental measurements over the $6 \leq Z \leq 16$ range. Quenching the transient field strength on the high-velocity side did not appreciably change the ϕ value, because the field strength is small as v moves away from Zv_0, and the projectiles spend the least time at the higher velocities (as the ions slow, more time is spent at the lower velocities where the transient field strength is higher). It was seen that the parametrization does not have a significant impact on the spin precession because the majority of the precession comes from the $v \sim Zv_0$ region where the field strength is well-characterized. There have been several measurements using sulfur ions in the $\frac{1}{2}Zv_0 \leq v \leq Zv_0$ velocity range, with a measurement at $v \approx \frac{1}{2}Zv_0$ in Fe and two measurements at $v = Zv_0$ and $v = \frac{1}{2}Zv_0$ in Gd, which make up part of the data set that was fit to obtain the ANU B_{TF} parametrization.

Rather than attempting to deduce $B_{TF}(Z = 16; \text{Fe})$ directly from only the sulfur transient field measurements, it is more accurate to find a global B_{TF} behavior, since the transient field is a general phenomenon for light ions at high velocities as found in Ref. [91]. Treating B_{TF} as a global function is justifiable at high velocities (near Zv_0) because the projectile energy is well above the region where atomic shell effects and possible molecular orbital effects come into play due to energy matching. Therefore the uncertainty due to the global parametrization does not play a significant role in the present measurements.

Since the γ-ray lineshape contains information on the velocity profile of the particles at the time of γ-ray emission, and the transient field is strongly velocity-dependent, a study was undertaken to determine the effects of the Doppler tails on the $\Delta\theta/g$ value and the S values, particularly as a function of detector angle. Using the GKINT routines, a Monte Carlo code was developed to analyze the effect of the lineshape on the precession effect [123]. The code generated incoming particle energies from a distribution that resulted in an outgoing particle energy spread resembling the measured particle energy distribution shown in Fig. 3.2. Coulomb excitation cross sections were calculated for randomly-picked interaction depths (hence energies) and scattering angles within the phoswich acceptance, and were accepted or rejected in a Monte Carlo fashion based on the Coulomb excitation cross section at that energy and scattering angle. After excitation, the particle was traced through the target, and a simulated γ ray could be emitted along its path at any time after excitation, according to the lifetime of the state. Using the particle energy after leaving the target, Doppler correction was performed in the same manner as the experimental analysis, for each SeGA detector, and a Doppler-corrected γ-ray lineshape was generated. The $a2$ and $a4$ parameters were also calculated as a function of lineshape to see the difference between the angular distribution of the Doppler tails and the vacuum peaks. It was concluded that the spin precession per unit g factor is dominated by the vacuum flight peak (accounting for 92% of the precession of the total lineshape) and that the

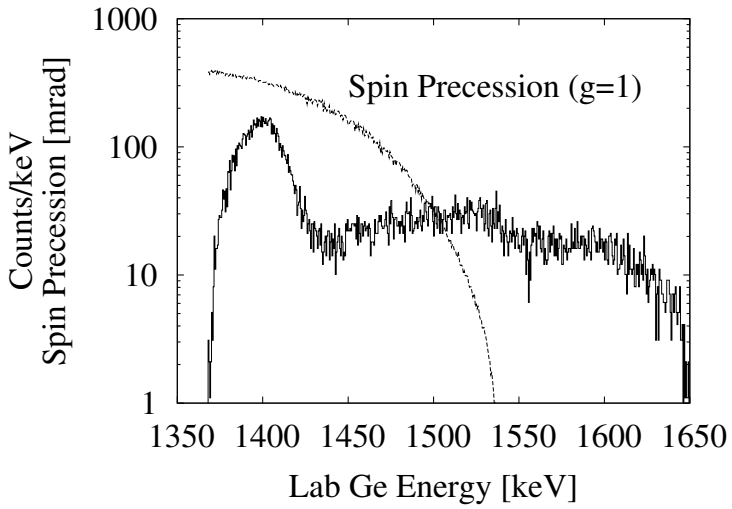

Figure 4.11: Doppler-shifted γ-ray spectrum modeled using Monte Carlo techniques [123], overlayed with the lineshape-dependent spin precession per unit g factor. The detected spin precession is dominated by contributions from the in-vacuum flight peak (see text).

Doppler tails do not impact the g factor measurement. The Monte Carlo modeling of the γ-ray lineshapes yielded $\Delta\theta/g$ values in agreement with the GKINT values shown in Table 4.2.

4.3.3 2^+ g factors of ^{38,40}S

The g factors for the 2_1^+ levels of ^{38}S and ^{40}S are deduced to be $+0.13(5)$ and $-0.01(6)$, respectively, using the spin precessions from a weighted average of the six SeGA angle pairs, shown in Table 4.1, and the calculated transient field strength in the spin precession per unit g factor shown in Table 4.2, which has been shown to be independent of the TF parametrization. The uncertainty in B_{TF}, obtained from the change upon quenching the high velocity TF strength discussed in the previous section, did not change the final uncertainty when added in quadrature with the statistical errors. All the available $g(2^+)$ values for sulfur isotopes are shown in Fig. 4.12. The errors in the g factors are dominated by the γ ray counting statistics. Interpretations of the g-factor results for ^{38,40}S are given in the following section, within the framework of

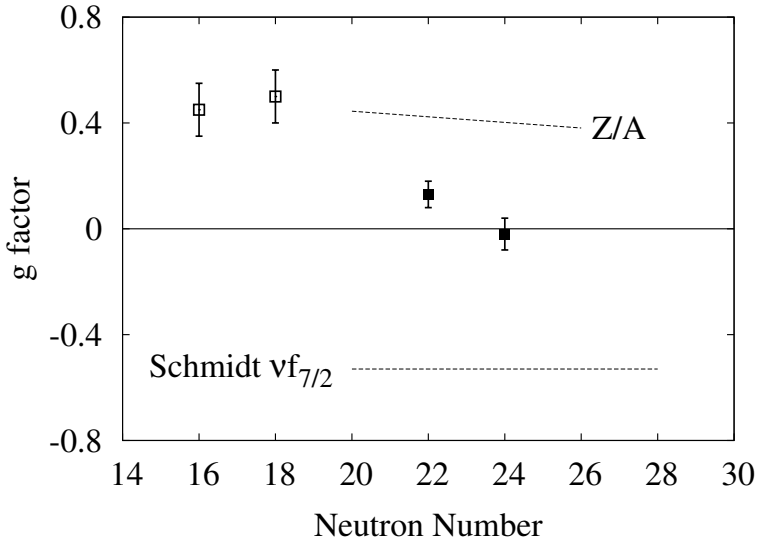

Figure 4.12: Comparison of previously-measured g factors of stable sulfur isotopes (open points) and the present radioactive isotope results (filled points). Also shown is the Schmidt value for $f_{7/2}$ neutrons, the orbital that begins to fill for $N \geq 20$, and the usual collective Z/A value, representing the two naive predictions for the single particle and the collective effects, respectively.

the shell model.

4.4 Interpretation of Measured $g(2^+)$ values

Shell model calculations were undertaken in order to interpret the excited-state g factors. The shell model calculations were performed with the program OXBASH [124], using an *sd-pf* model space where valence protons were restricted to the *sd* shell and valence neutrons were restricted to the *pf* shell. Calculations were performed for ${}^{36}_{16}S_{20}$, ${}^{38}_{16}S_{22}$, and ${}^{40}_{16}S_{24}$, and their isotones ${}^{38}_{18}Ar_{20}$, ${}^{40}_{18}Ar_{22}$ and ${}^{42}_{18}Ar_{24}$. The Nowacki interaction, which was developed in Refs. [20, 23] for application to neutron-rich nuclides near $N = 28$, was used for the shell-model calculations. The effective interaction consists of USD matrix elements [125] for the proton-proton interactions, the KB$'$ matrix elements [126] for the neutron-neutron interactions, and the Kahana, Lee, and Scott G matrix [127] for the proton-neutron interactions.

Table 4.3: Shell model and experimental values of excitation energies and $B(E2; 0_1^+ \rightarrow 2_1^+)$ values for ^{36,38,40}S and ^{38,40,42}Ar nuclides, as well as predicted quadrupole moments, and deformation parameters extracted from the predicted quadrupole moments, predicted B(E2) values, and measured B(E2) values.

Nuclide	$E_{2^+}^{\rm th}$ (MeV)	$E_{2^+}^{\rm exp}$ (MeV)	$Q(2_1^+)$ e fm^2	$B(E2)^{\rm th}$ e^2 fm^4	$B(E2)^{\rm exp}$	$\beta_Q^{\rm th}$	$\lvert\beta_{E2}^{\rm th}\rvert$	$\lvert\beta^{\rm exp}\rvert$
^{36}S	3.426	3.291	−11.6	141	104(28)	+0.21	0.20	0.17(2)
^{38}S	1.531	1.292	−9.7	268	235(30)	+0.17	0.26	0.25(2)
^{40}S	0.980	0.904	−19.3	473	334(36)	+0.33	0.34	0.28(2)
^{38}Ar	2.018	2.167	+4.3	178	130(10)	−0.07	0.19	0.16(1)
^{40}Ar	1.371	1.461	+8.5	263	330(40)	−0.13	0.22	0.25(2)
^{42}Ar	1.243	1.208	+5.2	360	430(10)	−0.08	0.25	0.28(3)

The calculations gave first-excited 2^+ state energies, reduced transition probabilities to the first 2^+ states, and quadrupole moments of the 2^+ states of ^{36,38,40}S and ^{38,40,42}Ar. Standard effective charges of $e_p \sim 1.5$ and $e_n \sim 0.5$ were used. The $E(2^+)$ and B(E2) values are in good agreement with experimental values, and are compared in Table 4.3. In general, the excited-state energies are reproduced within about 200 keV, and the trends in the B(E2) values are correctly reproduced.

The $g(2^+)$ values were obtained from the calculated shell-model wavefunctions, using bare nucleon g factors. The calculated g factors are compared to the experimental values in Fig. 4.13. The ^{38,40}Ar values were recently measured using the conventional transient field method [128, 129]. The ^{36}S $g(2^+)$ value has not been measured due to its high excitation energy and short lifetime, although ^{36}S is stable. The ^{42}Ar $g(2^+)$ value has not been measured, since ^{42}Ar is radioactive. The calculations reproduce the g-factor behavior of the sulfur and argon isotopes fairly well, and therefore some insight can be gained by examining the shell model results in more detail.

The individual contributions of the neutrons and protons are separated in Table 4.4, and one can see that a near cancelation of the neutron and proton g factors

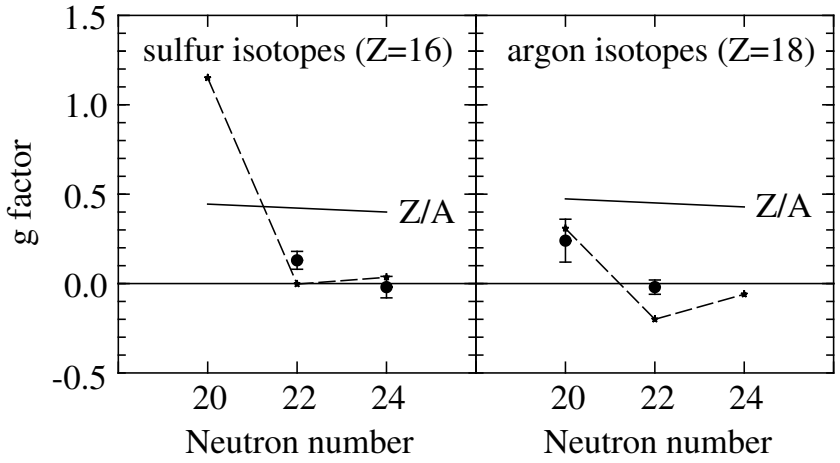

Figure 4.13: Comparison of measured g factors and shell model predictions (see text). The nearest stable nuclides to the sulfur isotopes for which g-factor results are available, the argon isotopes (Refs. [128] and [129]), are shown on the right hand side, and the results of the current work are shown on the left.

is causing the small values for the $N = 22$ and $N = 24$ isotones. At $N = 20$, the 2^+ wavefunction of ^{36}S consists exclusively of proton excitations within this model space, leading to a large positive g factor that comes primarily from coupling an $s_{1/2}$ proton and a $d_{3/2}$ proton to spin $I = 2$. As neutrons begin to occupy the $f_{7/2}$ single-particle orbital, there are still positive contributions of proton excitations in the 2^+_1 states of ^{38}S and ^{40}S. The proton excitations effectively cancel the neutron contributions that would naively dominate the excited-state wavefunctions due to the close proximity of the $N = 20$ shell closure.

To investigate the neutron shell structure further, the shell model calculations were repeated with the valence neutrons restricted to the $f_{7/2}$ orbital (i.e., not allowed to be excited to the other orbitals in the fp shell that lie above the $N = 28$ gap). The results of the two shell model calculations are displayed in Table 4.5. There were two substantial differences in the $g(2^+)$ value for ^{38}S. The neutron g factor resembles more closely the $f_{7/2}$ Schmidt value, as would be expected when the neutrons are restricted to the $f_{7/2}$ orbital. However, an additional effect is that the proton g factor becomes *less positive*, due to fewer proton excitations contributing to the 2^+ wavefunction.

Table 4.4: Theoretical g factors compared with experiment. The measured ^{38}Ar and ^{40}Ar g factors are from Refs. [128] and [129], respectively.

Nuclide	$g^{\text{th}}_{\text{proton}}$	$g^{\text{th}}_{\text{neutron}}$	g^{th}	g^{exp}
$^{36}_{16}S_{20}$	+1.15	0	+1.15	
$^{38}_{16}S_{22}$	+0.298	−0.301	−0.0026	+0.13(5)
$^{40}_{16}S_{24}$	+0.276	−0.241	+0.035	−0.01(6)
$^{38}_{18}Ar_{20}$	+0.308	0	+0.308	+0.24(12)
$^{40}_{18}Ar_{22}$	+0.164	−0.364	−0.200	−0.02(4)
$^{42}_{18}Ar_{24}$	+0.220	−0.280	−0.060	

Table 4.5: Detailed decomposition of theoretical g factors compared with experiment. The g factors that result from restricting valence neutrons to the $f_{7/2}$ orbital are in the rows labeled with the "SDF" model space, and the g factors from the full fp shell calculation are in the rows labeled with the "SDPF" model space.

Nuclide	Model	$g^{\text{th}}_{\text{proton}}$			$g^{\text{th}}_{\text{neutron}}$	g^{th}	g^{exp}
		orbital	spin	total			
$^{36}_{16}S_{20}$	SDPF	0.9667	0.1868	+1.15	0	+1.15	
$^{38}_{16}S_{22}$	SDPF	0.2248	0.0733	+0.298	−0.301	−0.003	+0.13(5)
	SDF	0.087	0.049	+0.136	−0.494	−0.358	
$^{40}_{16}S_{24}$	SDPF	0.2249	0.0513	+0.276	−0.241	+0.035	−0.01(6)
	SDF	0.2489	0.0695	+0.3184	−0.4037	−0.0853	
$^{38}_{18}Ar_{20}$	SDPF	1.1509	−0.8424	+0.308	0	+0.308	+0.24(12)
$^{40}_{18}Ar_{22}$	SDPF	0.3109	−0.1470	+0.164	−0.364	−0.200	−0.02(4)
	SDF	0.2278	−0.0922	0.1356	−0.4310	−0.2954	
$^{42}_{18}Ar_{24}$	SDPF	0.2629	−0.0431	+0.220	−0.280	−0.060	
	SDF	0.2421	−0.0254	0.2167	−0.4167	−0.2000	

The proton excitations seem to be very closely linked to neutron excitations into the higher orbitals in the fp shell, and the resulting theoretical g factor changes from -0.358 (with neutrons restricted to $f_{7/2}$), to -0.003 (when neutrons are allowed to spread into the full fp shell).

Details of the contributing components to the 2^+ wavefunctions of ^{38}S and ^{40}S are shown graphically in Fig. 4.14. The contributions of the main proton partitions are shown for both the restricted and full-fp shell model calculations. There are eight valence protons available to partition among the three sd orbitals ($d_{5/2}$, $s_{1/2}$, and $d_{3/2}$) beyond the $Z = 8$ closed shell at oxygen. The different combinations shown in Fig. 4.14 give rise to different g factors, depending upon how the different particles are coupled together, and for the simple cases, g factors are shown next to the relevant partition. Not shown are off-diagonal components, such as $\nu f_{7/2} - \nu f_{5/2}$ or $\pi d_{5/2} - \pi d_{3/2}$ terms which have $\Delta\ell = 0$ and can therefore contribute to the magnetic moment. The difference between the restricted and full calculation is more pronounced in ^{38}S than in ^{40}S. The $N = 22$ nucleus ^{38}S has one pair of valence neutrons, and the two neutrons were found by the full fp shell calculations to be partitioned as 63.2% $f_{7/2}^2$, 24.4% $f_{7/2}^1 p_{3/2}^1$, and 4.2% $f_{7/2}^0 p_{3/2}^2$, taking into account partitions that contribute 1% or more to the total wavefunction. In the 2_1^+ wavefunction of ^{38}S, it is more favorable for a proton to be excited from $s_{1/2}$ to $d_{3/2}$ when the neutrons are also allowed to be excited. Such a strong influence of the neutron occupancies on the proton configuration indicates that they are strongly coupled together, which is a prerequisite for the onset of deformation. When two additional neutrons are added to make ^{40}S, the shell model calculations show that they are partitioned as 47% $f_{7/2}^4$, 25% $f_{7/2}^3 p_{3/2}^1$, and 8.8% $f_{7/2}^2 p_{3/2}^2$, again only accounting for partitions that contribute 1% or more to the total wavefunction. There is not as large of a change in the ^{40}S proton configuration, which was already composed of several proton excitations to begin with than in the case of ^{38}S. Closer inspection of Table 4.5 shows that the change in the ^{40}S g factor when neutrons are restricted to $f_{7/2}$ is due almost entirely

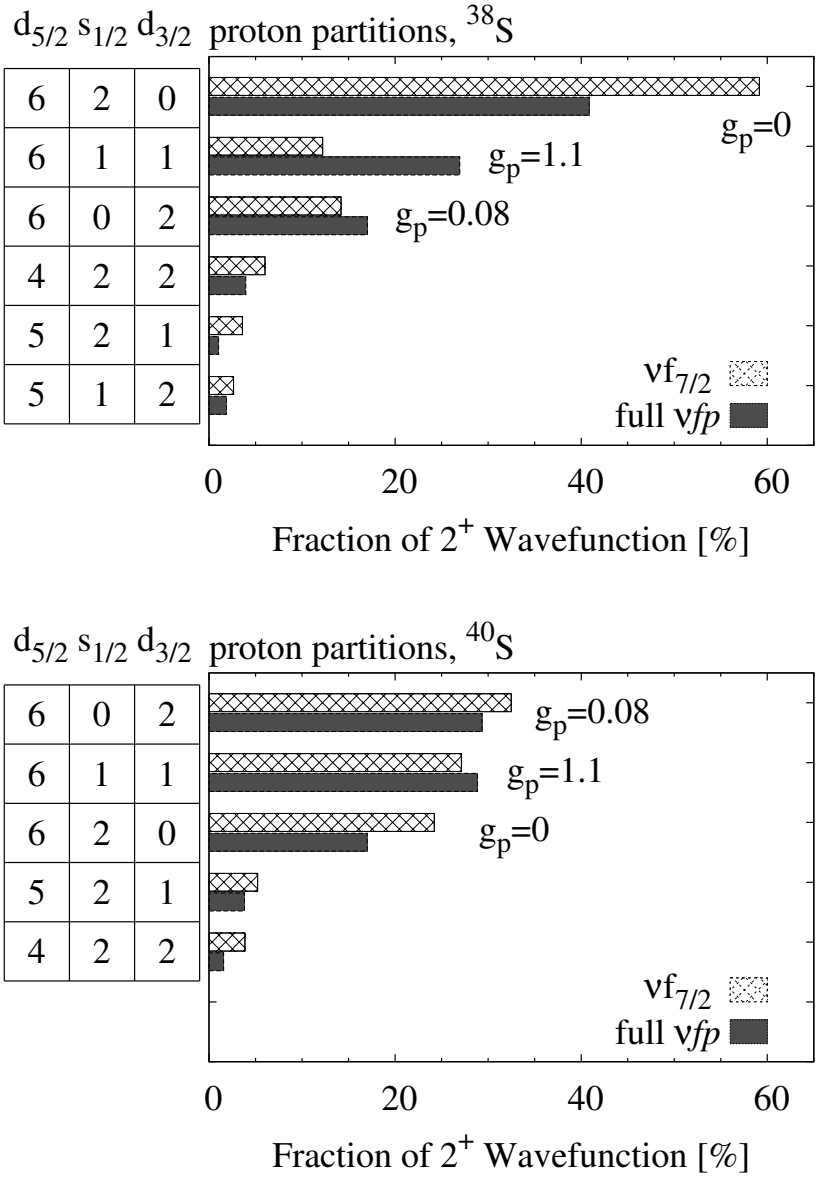

Figure 4.14: Calculated components of the 2^+ wavefunctions of ^{38}S (left) and ^{40}S (right). The main proton partitions are labeled and the horizontal bars represent the fraction of the 2^+ wavefunctions. Two different shell model results are shown. The hatched bars are results of a restricted shell model calculation that forced the valence neutrons to occupy the $f_{7/2}$ orbital, and the solid bars show the results of the full fp shell calculation that allows neutrons to occupy higher-lying orbitals. The Schmidt values for particular proton partitions are shown for selected cases.

to the change in the neutron g factor contribution.

The ^{40}S $g(2^+)$ result is interesting because it is nearly zero, although ^{40}S is assumed to be deformed according to the $E(2^+)$ and B(E2) systematics. The shell model calculations for ^{40}S predict a quadrupole moment that leads to a deformation parameter of $\beta_2 \approx +0.3$, which agrees with the value extracted from the B(E2) measurement [10]. Therefore the onset of deformation is confirmed by the shell model calculations that explain the g-factor results. However, the magnetic behavior of the deformed ^{40}S nucleus is manifested in an unprecedented way, since in general, deformed nuclei have been found to exhibit g factors that are the result of the orbital motion of the protons alone (since the neutrons have $g_\ell = 0$), with intrinsic spin contributions of the neutrons and protons usually assumed to be very small in collective models. Traditionally, it has been assumed that deformed nuclei should always have g factors near Z/A, since without exception the deformed, stable, even-even nuclei with known g factors (whether they are the $A \sim 150$ rare earth elements, or deformed light $N = Z$ nuclei) have $g(2^+) \approx Z/A$. Large neutron spin contributions to the $g(2^+)$ value in a deformed nucleus, as is seen in ^{40}S, have not been reported previously in the literature. The Z/A collective prediction for $g(2^+)$ is not generally regarded to be well-justified theoretically, but it is generally held as an empirical rule. There is now evidence that shell effects, which lead to large neutron spin contributions to the g factor, can overcome the tendency for deformed nuclei to have gyromagnetic ratios of $+Z/A$.

4.5 Summary and Outlook

The successful measurement of the 2_1^+ g factors of ^{38}S and ^{40}S demonstrates that the transient field technique can be applied successfully to fast fragment beams. Shell model results indicate that the transitional neutron-rich sulfur isotopes show shell effects indicative of active neutron shell gaps around the $f_{7/2}$ orbit. The filling of the

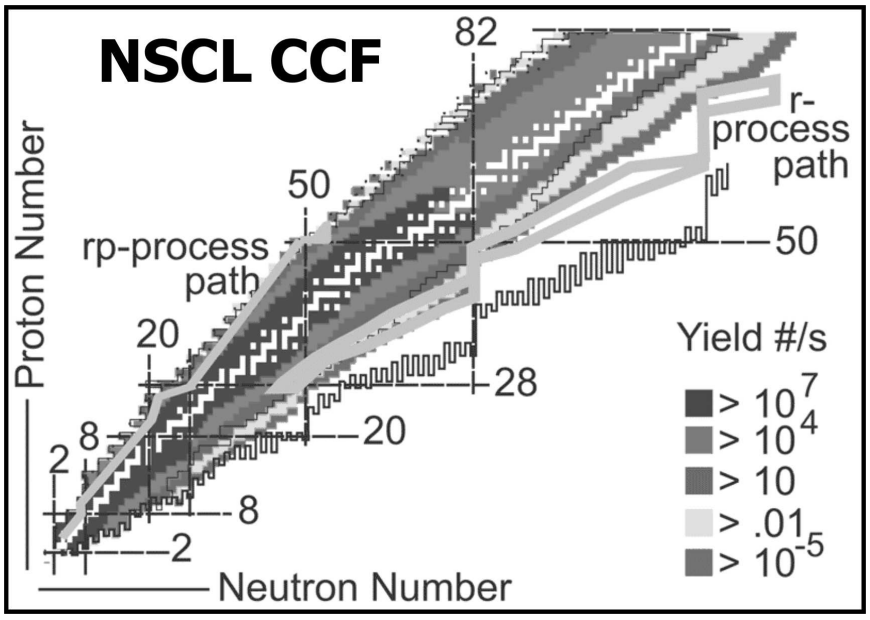

Figure 4.15: Calculated yields of the Coupled Cyclotron Facility. The ^{40}S measurement reported in this dissertation indicates that fast-fragment g factors of short lived states can be measured with rates of 10^4 particles per second.

$f_{7/2}$ neutron orbit, however, affects the protons through an interaction that causes the $s_{1/2}$-$d_{3/2}$ gap to change, as has been the subject of much recent experimental [130] as well as theoretical [27] interest. In addition, it was observed that the neutron occupation of higher-lying states across the $N = 28$ gap has a profound effect on the proton occupancies, indicating that the neutrons and protons are strongly coupled. Since the g factors contain information on orbital components of the wavefunction, they offer a sensitive and unique means to assess how shifts in the single-particle energy spectrum and orbital occupancies occur. The transition from single-particle behavior to collectivity that occurs in the neutron-rich sulfur isotopes has been investigated by measurements of their $g(2^+)$ values, allowing a microscopic study of the dramatic deformation change, since the g factors provide stringent constraints on the nuclear wavefunctions of ^{38}S and ^{40}S.

Earlier measurements on the stable ^{32,34}S isotopes [131] can be compared to the present work, as shown in Fig. 4.12. The similar magnitudes of the error bars, given the disparity in the beam intensities for the stable versus the radioactive sulfur mea-

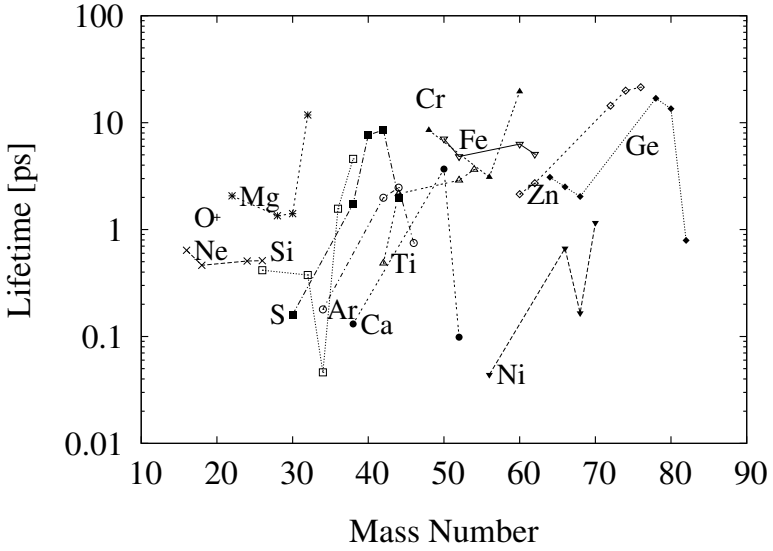

Figure 4.16: Estimates of first 2^+ lifetimes (using the Grodzins relation, for levels with energies less that 3 MeV) in radioactive even-even nuclides. Isotopic chains are labeled and connected by lines.

surements, shows that the HVTF technique can take advantage of the high projectile energies and utilize thick ferromagnet layers, which increases the interaction time with B_{TF}. In fact, most of the interaction time is spent near Zv_0 as the fast beam slows through the peak of the transient field strength, whereas most stable-beam measurements are moving away from Zv_0 as they slow down in the target. For the specific cases of the stable sulfur isotopes shown in Fig. 4.12, the interaction time with the transient field is low due to the short excited state lifetimes of less than 0.5 ps, but the beam currents available were on the order of 10^{11} particles per second. The ^{40}S measurement demonstrates that the HVTF method is applicable to beams with intensities as low as 10^4 particles per second. The yield of secondary fragments at the Coupled Cyclotron Facility is shown in Fig. 4.15, and a large region of the nuclear chart is available through fragmentation, at the 10^4 pps rate.

The transient field measurement of $g(2^+)$ with fast projectiles depends on slowing the projectiles down in a timely manner, governed by the 2^+ lifetime τ. The $\tau(2^+)$ value of a particular isotope provides the severest constraint on the feasibility of an

HVTF measurement. In general, the time to slow ions in the target material will depend on the ion atomic number Z and the incoming projectile velocity. The final velocity should be near Zv_0, which means higher-Z ions need less slowing than lower Z ions, although the behavior of the transient field at high velocities for higher Z ions is not well studied, and the maximum transient field strength may no longer be at the velocity Zv_0. Since stopping powers are increasing functions of the projectile Z, it appears that moving higher in the periodic table is advantageous from a projectile velocity point of view, but much work is still needed to characterize the transient field for $Z > 16$ ions at and above the K-shell electron velocity. This is a difficult task to undertake at a radioactive beam facility, but may be well-suited for stable-beam facilities since in general stable isotopes have known $g(2^+)$ values and are available with high beam intensities. An estimation of 2_1^+ lifetimes (using the Grodzins relation [12]) in radioactive even-even nuclei with $Z \leq 32$ is shown in Fig. 4.16 for states with an excitation energy of 3.3 MeV or less. It can be seen that a large number of states have favorable lifetimes for the HVTF method. One such state, the 2_1^+ state in the deformed $N = 20$ nucleus ^{32}Mg, has a similar energy, B(E2) value, and lifetime to ^{40}S. Shell effects, such as those observed in the neutron-rich sulfur isotopes, are not expected to be strong (since the $N = 20$ shell closure has disappeared at $Z = 12$), and a $g(2^+)$ measurement is highly desirable to investigate the magnetic properties of a well-deformed nucleus located far from stability.

Bibliography

[1] A. de-Shalit and M. Goldhaber, *Phys. Rev.* **92**:1211 (1953).

[2] T. Lee, D. A. Papanastassiou, and G. J. Wasserburg, *Astrophys. J.* **220**:L21 (1978).

[3] O. Sorlin, D. Guillemaud-Mueller, A. C. Mueller, *et al.*, *Phys. Rev. C* **47**:2941 (1993).

[4] N. J. Davis, J. A. Kuehner, A. A. Pilt, A. J. Trudel, M. C. Vetterli, C. Bamber, E. K. Warburton, J. W. Olness, and S. Raman, *Phys. Rev. C* **32**:713 (1985).

[5] J. W. Olness, E. K. Warburton, J. A. Becker, D. J. Decman, E. A. Henry, L. G. Mann, and L. Ussery, *Phys. Rev. C* **34**:2049 (1986).

[6] E. K. Warburton, D. E. Alburger, and G. Wang, *Phys. Rev. C* **36**:429 (1987).

[7] L. K. Fifield *et al.*, *Nucl. Phys. A* **417**:534 (1984).

[8] W. A. Mayer *et al.*, *Z. Phys. A* **319**:287 (1984).

[9] B. Fornal, R. H. Mayer, I. G. Bearden, *et al.*, *Phys. Rev. C* **49**:2413 (1994).

[10] H. Scheit, T. Glasmacher, B. A. Brown, *et al.*, *Phys. Rev. Lett.* **77**:3967 (1996).

[11] T. Glasmacher, B. A. Brown, M. J. Chromik, *et al.*, *Phys. Lett. B* **395**:163 (1997).

[12] S. Raman, C. W. Nestor, and P. Tikkanen, *At. Data Nucl. Data Tables* **78**:1 (2001).

[13] H. Scheit, Ph.D. thesis, Michigan State University (1998).

[14] P. Möller and J. R. Nix, *At. Data Nucl. Data Tables* **26**:165 (1981).

[15] T. R. Werner, J. A. Sheikh, W. Nazarewicz, M. R. Strayer, A. S. Umar, and M. Misu, *Phys. Lett. B* **335**:259 (1994).

[16] T. R. Werner, J. A. Sheikh, M. Misu, W. Nazarewicz, J. Rikovska, K. Heeger, A. S. Umar, and M. R. Strayer, *Nucl. Phys. A* **597**:327 (1996).

[17] J. A. Winger, P. F. Mantica, R. M. Ronningen, and M. A. Caprio, *Phys. Rev. C* **64**:064318 (2001).

[18] J. H. Kelley, T. Suomijärvi, S. E. Hirzebruch, *et al.*, *Phys. Rev. C* **56**:1206 (1997).

[19] D. Sohler, Z. Dombrádi, J. Timár, *et al.*, *Phys. Rev. C* **66**:054302 (2002).

[20] J. Retamosa, E. Caurier, F. Nowacki, and A. Poves, *Phys. Rev. C* **55**:1266 (1997).

[21] D. Hirata, K. Sumiyoshi, B. V. Carlson, H. Toki, and I. Tanihata, *Nucl. Phys. A* **609**:131 (1996).

[22] G. A. Lalazissis *et al.*, *Phys. Rev. C* **60**:014310 (1999).

[23] S. Nummela, P. Baumann, E. Caurier, P. Dessagne, A. Jokinen, *et al.*, *Phys. Rev. C* **63**:044316 (2001).

[24] E. Caurier, F. Nowacki, and A. Poves, *Nucl. Phys. A* **742**:14 (2004).

[25] R. Rodríguez-Guzmán, J. L. Egido, and L. M. Robledo, *Phys. Rev. C* **65**:024304 (2002).

[26] J. Dobaczewski, I. Hammamoto, W. Nazarewicz, and J. A. Sheikh, *Phys. Rev. Lett.* **72**:981 (1994).

[27] T. Otsuka, T. Suzuki, R. Fujimoto, H. Grawe, and Y. Akaishi, *Phys. Rev. Lett.* **95**:232502 (2005).

[28] P. D. Cottle and K. W. Kemper, *Phys. Rev. C* **58**:3761 (1998).

[29] T. Motobayashi, Y. Ikeda, Y. Ando, *et al.*, *Phys. Lett. B* **346**:9 (1995).

[30] S. Grévy, J. C. Angélique, P. Baumann, *et al.*, *Phys. Lett. B* **594**:252 (2004).

[31] J. Fridmann, I. Wiedenhöver, A. Gade, *et al.*, *Nature* **435**:922 (2005).

[32] P. D. Cottle and K. W. Kemper, *Phys. Rev. C* **66**:061301 (2002).

[33] J. D. Jackson, *Classical Electrodynamics* (John Wiley and Sons, New York, 1975).

[34] J. M. Blatt and V. F. Weisskopf, *Theoretical Nuclear Physics* (Wiley, New York, 1952).

[35] S. Eidelman, K. G. Hayes, K. A. Olive, *et al.*, *Phys. Lett. B* **592**:1 (2004), Particle Data Group.

[36] M. G. Mayer, *Phys. Rev.* **75**:1969 (1949).

[37] O. Haxel, J. H. Jensen, and H. E. Suess, *Phys. Rev.* **75**:1766 (1949).

[38] D. M. Brink and G. R. Satchler, *Angular Momentum* (Clarendon Press, Oxford, 1968).

[39] B. Castel and I. S. Towner, *Modern Theories of Nuclear Moments* (Clarendon Press, Oxford, 1990).

[40] B. A. Brown, *Prog. Part. Nucl. Phys.* **47**:517 (2001).

[41] E. Caurier, G. Martínez-Pinedo, F. Nowacki, A. Poves, and A. P. Zuker, *Rev. Mod. Phys.* **77**:427 (2005).

[42] R. J. Blin-Stoyle, *Rev. Mod. Phys.* **28**:75 (1956).

[43] N. J. Stone, *At. Data Nucl. Data Tables* **90**:75 (2005).

[44] N. Bohr, *Nature* **137**:344 (1936).

[45] A. Bohr and B. Mottelson, *Nuclear Structure*, vol. 2 (Benjamin, New York, 1975).

[46] A. E. Stuchbery, *Nucl. Phys. A* **589**:222 (1995).

[47] O. Prior, F. Boehm, and S. G. Nilsson, *Nucl. Phys. A* **110**:257 (1968).

[48] E. L. Brady and M. Deutsch, *Phys. Rev.* **78**:558 (1950).

[49] R. R. Borchers, J. D. Bronson, D. E. Murnick, and L. Grodzins, *Phys. Rev. Lett.* **17**:1099 (1966).

[50] R. R. Borchers, B. Herskind, J. D. Bronson, L. Grodzins, R. Kalish, and D. E. Murnick, *Phys. Rev. Lett.* **20**:424 (1968).

[51] N. Benczer-Koller, M. Hass, and J. Sak, *Annu. Rev. Nucl. Part. Sci.* **30**:53 (1980).

[52] K.-H. Speidel, O. Kenn, and F. Nowacki, *Prog. Part. Nucl. Phys.* **49**:91 (2002).

[53] N. Rud and K. Dybdal, *Phys. Scr.* **34**:561 (1986).

[54] R. D. Gill, *Gamma-Ray Angular Correlations* (Academic Press, New York, 1975).

[55] T. Yamazaki, *Nucl. Data A* **3**:1 (1967).

[56] A. E. Stuchbery, *Nucl. Phys. A* **723**:69 (2003).

[57] H. Morinaga and T. Yamazaki, *In-Beam Gamma-Ray Spectroscopy* (North-Holland, Amsterdam, 1976).

[58] K. S. Krane, in *Low Temperature Nuclear Orientation*, edited by N. J. Stone and H. Postma (Elsevier Science, 1986), p. 31.

[59] G. Goldring, in *Heavy Ion Collisions*, edited by R. Bock (North-Holland, Amsterdam, 1982), vol. 3, p. 484.

[60] R. E. Tuzan, P. Burkhardt, and D. Secrest, *Comp. Phys. Comm.* **112**:112 (1998).

[61] H. Frauenfelder and R. M. Steffen, in *Alpha-, Beta-, and Gamma-Ray Spectroscopy*, edited by K. Siegbahn (North-Holland, Amsterdam, 1965).

[62] M. J. L. Yates, in *Alpha-, Beta-, and Gamma-Ray Spectroscopy*, edited by K. Siegbahn (North-Holland, Amsterdam, 1965).

[63] D. C. Camp and A. L. Van Lehn, *Nucl. Inst. & Meth.* **76**:192 (1969).

[64] A. E. Stuchbery, private communication.

[65] U. Reuter, F. Hagelberg, S. Kremeyer, H.-J. Simonis, K.-H. Speidel, M. Knopp, W. Karle, J. Cub, P. N. Tandon, and J. Gerber, *Phys. Lett. B* **230**:16 (1989).

[66] P. C. Zalm, A. Holthuizen, J. A. G. de Raedt, and G. van Middelkoop, *Phys. Lett. B* **69**:157 (1977).

[67] A. E. Stuchbery, C. G. Ryan, H. Ohnuma, G. B. Beard, and H. H. Bolotin, *Phys. Rev. C* **27**:434 (1983).

[68] M. B. Goldberg, W. Knauer, G. J. Kumbartzki, K. H. Speidel, J. C. Adloff, and J. Gerber, *Hyperfine Interact.* **4**:262 (1978).

[69] J. L. Eberhardt, R. E. Horstmann, P. C. Zalm, H. A. Doubt, and G. van Middelkoop, *Hyperfine Interact.* **3**:195 (1977).

[70] N. K. B. Shu, D. Melnik, J. M. Brennan, W. Semmler, and . Benczer-Koller, *Phys. Rev. C* **21**:1828 (1980).

[71] H. R. Andrews, O. Häusser, D. Ward, P. Taras, R. Nicole, J. Keinonen, P. Skensved, and B. Haas, *Nucl. Phys. A* **383**:509 (1982).

[72] C. Caso *et al.*, *Eur. Phys. Jour.* **C3**:1 (1998).

[73] J. F. Ziegler, *J. Appl. Phys.* **85**:1249 (1999).

[74] S. Schielke, K.-H. Speidel, O. Kenn, J. Leske, N. Gemein, M. Offer, Y. Y. Sharon, L. Zamick, J. Gerber, and P. Maier-Komor, *Phys. Lett. B* **567**:153 (2003).

[75] K.-H. Speidel, J. Leske, S. Schielke, S. C. Bedi, O. Zell, P. Maier-Komor, S. J. Q. Robinson, Y. Y. Sharon, and L. Zamick, *Phys. Lett. B* **633**:219 (2006).

[76] O. Kenn, K.-H. Speidel, R. Ernst, S. Schielke, S. Wagner, J. Gerber, P. Maier-Komor, and F. Nowacki, *Phys. Rev. C* **65**:034308 (2002).

[77] K.-H. Speidel, N. Benczer-Koller, G. Kumbartzki, *et al.*, *Phys. Rev. C* **57**:2181 (1998).

[78] J. Holden, N. Benczer-Koller, G. Jakob, *et al.*, *Phys. Rev. C* **63**:024315 (2001).

[79] G. Kumbartzki, J. R. Cooper, N. Benczer-Koller, *et al.*, *Phys. Lett. B* **591**:213 (2004).

[80] R. E. Laxdal, *Nucl. Inst. Meth. Phys. Res. B* **204**:400 (2003).

[81] O. Kester, T. Sieber, S. Emhofer, *et al.*, *Nucl. Inst. Meth. Phys. Res. B* **204**:20 (2003).

[82] C. J. Gross, *J. Phys. G* **31**:S1639 (2005).

[83] D. H. Feng, A. R. Barnett, and L. J. B. Goldfarb, *Phys. Rev. C* **13**:1151 (1976).

[84] A. N. F. Aleixo and C. A. Bertulani, *Nucl. Phys. A* **505**:448 (1989).

[85] T. Czosnyka, D. Cline, L. Hasselgren, C. Y. Wu, R. M. Diamond, H. Kluge, C. Roulet, E. K. Hulet, R. W. Lougheed, and C. Baktash, *Nucl. Phys. A* **458**:123 (1986).

[86] H. Goldstein, *Classical Mechanics* (Addison-Wesley, 1980).

[87] J. Cub, M. Bussas, K. H. Speidel, *et al.*, *Z. Phys. A* **345**:1 (1993).

[88] U. Grabowy, K. H. Speidel, *et al.*, *Z. Phys. A* **359**:377 (1997).

[89] O. Kenn, K.-H. Speidel, R. Ernst, J. Gerber, P. Maier-Komor, N. Benczer-Koller, G. Kumbartzki, and F. Becker, *Nucl. Inst. Meth. Phys. Res. B* **171**:589 (2000).

[90] H. Ueno, W. Sato, H. Ogawa, *et al.*, *Hyperfine Interact.* **136**:211 (2001).

[91] A. E. Stuchbery, *Phys. Rev. C* **69**:064311 (2004).

[92] H. Kopfermann, *Nuclear Moments* (Academic Press, New York, 1958).

[93] O. Tarasov, D. Bazin, M. Lewitowicz, and O. Sorlin, *Nucl. Phys. A* **701**:661 (2002).

[94] D. Bazin, O. Tarasov, M. Lewitowicz, and O. Sorlin, *Nucl. Inst. Meth. Phys. Res. A* **482**:307 (2002).

[95] A. E. Stuchbery, A. N. Wilson, P. M. Davidson, A. D. Davies, T. J. Mertzimekis, S. N. Liddick, B. E. Tomlin, and P. F. Mantica, *Phys. Lett. B* **611**:81 (2005).

[96] J. F. Ziegler, *SRIM Special — Degrader Blocks* (2000), Documentation of computer program SRIM.

[97] J. F. Ziegler, *Computer program SRIM*, Tech. rep., IBM-Research, New York (2000).

[98] D. J. Morrissey, B. M. Sherrill, M. Steiner, A. Stolz, and I. Wiedenhoever, *Nucl. Inst. Meth. Phys. Res. B* **204**:90 (2003).

[99] J. F. Ziegler, J. P. Biersack, and U. Littmark, in *The stopping and ranges of ions in matter*, edited by J. F. Ziegler (Pergamon, New York, 1985), vol. 1.

[100] H. Geissel and C. Scheidenberger, *Nucl. Inst. Meth. Phys. Res. B* **136**:114 (1998).

[101] J. Lindhard and A. H. Sørensen, *Phys. Rev. A* **53**:2443 (1996).

[102] W. F. Mueller, J. A. Church, T. Glasmacher, D. Gutknecht, G. Hackman, P. G. Hansen, Z. Hu, K. L. Miller, and P. Quirin, *Nucl. Inst. Meth. Phys. Res. A* **466**:492 (2001).

[103] Z. Hu, T. Glasmacher, W. F. Mueller, and I. Wiedenhöver, *Nucl. Inst. Meth. Phys. Res. A* **482**:715 (2002).

[104] H. Zwahlen, Ph.D. thesis, Michigan State University (2005).

[105] K. L. Miller, T. Glasmacher, C. Campbell, L. Morris, W. F. Mueller, and E. Strahler, *Nucl. Inst. Meth. Phys. Res. A* **490**:140 (2002).

[106] G. Jakob, N. Benczer-Koller, G. Kumbartzki, *et al.*, *Phys. Rev. C* **65**:024316 (2002).

[107] A. E. Stuchbery, *Some notes on the program GKINT: Transient-field g-factor kinematics at intermediate energies*, Department of Nuclear Phyiscs, The Australian National University, report no. ANU-P/1678 (2005).

[108] J. A. Church, C. M. Campbell, D.-C. Dinca, *et al.*, *Phys. Rev. C* **72**:054320 (2005).

[109] *BC-400 and BC-444 Plastic Scintillator Data Sheets* (2005), Saint Gobain Ceramics & Plastics, Inc., Newbury, OH.

[110] W. F. Mueller, private communication.

[111] E. Hecht, *Optics* (Addison-Wesley, 1998).

[112] R. Fox, E. Kasten, K. Orji, C. Bolen, C. Maurice, and J. Venema, *IEEE Trans. Nucl. Sci.* **51**:571 (2004).

[113] C. Kittel, *Introduction to Solid State Physics* (Wiley, New York, 1996).

[114] N. Benczer-Koller, private communication.

[115] A. Piqué, J. M. Brennan, R. Darling, R. Tanczyn, D. Ballon, and N. Benczer-Koller, *Nucl. Inst. Meth. Phys. Res. A* **279**:579 (1989).

[116] K. Halbach and R. F. Holsinger, *Particle Accelerators* **7**:213 (1976).

[117] J. H. Hubbell and S. M. Seltzer, *Tables of X-Ray Mass Attenuation Coefficients and Mass Energy-Absorption Coefficients*, Tech. rep., National Institute of Standards and Technology, Gaithersburg, MD (2004).

[118] O. Klein and Y. Nishina, *Z. Physik* **52**:853 (1929).

[119] T. Glasmacher, *Annu. Rev. Nucl. Part. Sci.* **48**:1 (1998).

[120] D. Pelte and D. Schwalm, in *Heavy Ion Collisions*, edited by R. Bock (North-Holland, Amsterdam, 1982), vol. 3, p. 1.

[121] C. A. Bertulani, A. E. Stuchbery, T. J. Mertzimekis, and A. D. Davies, *Phys. Rev. C* **68**:044609 (2003).

[122] A. E. Stuchbery, P. M. Davidson, and A. N. Wilson, *Nucl. Inst. Meth. Phys. Res. B* (2005), in press.

[123] A. E. Stuchbery and A. D. Davies, to be published.

[124] B. A. Brown, A. Etchegoyen, N. S. Godwin, W. D. M. Rae, W. A. Richter, W. E. Ormand, E. K. Warburton, J. S. Winfield, L. Zhao, and C. H. Zimmerman, *Oxbash for Windows PC*, Michigan State University, report no. MSU-NSCL 1289 (2004).

[125] B. H. Wildenthal, *Prog. Part. Nucl. Phys.* **11**:5 (1984).

[126] A. Poves and A. Zuker, *Phys. Rep.* **70**:235 (1981).

[127] S. Kahana, H. C. Lee, and C. K. Scott, *Phys. Rev.* **180**:956 (1969).

[128] K.-H. Speidel, S. Schielke, J. Leske, J. Gerber, P. Maier-Kormor, S. J. Q. Robinson, Y. Y. Sharon, and L. Zamick, *Phys. Lett. B* **632**:207 (2006).

[129] E. Stefanova, N. Benczer-Koller, G. Kumbartzki, *et al.*, *Phys. Rev. C* **72**:014309 (2005).

[130] A. Gade, B. A. Brown, D. Bazin, *et al.*, *Evolution of the E(1/2)-E(3/2) energy spacing in odd-mass K, Cl, and P Isotopes for N=20-28*, NSCL Preprint MSUCL-1309 (2006).

[131] P. C. Zalm, A. Holthuizen, J. A. G. de Raedt, and G. van Middelkoop, *Nucl. Phys. A* **315**:133 (1979).